

RXJ0152.7–1357: STELLAR POPULATIONS IN AN X-RAY LUMINOUS GALAXY CLUSTER AT $z=0.83$

INGER JØRGENSEN

Gemini Observatory, 670 N. A'ohoku Pl., Hilo, HI 96720, USA

MARCEL BERGMANN

NOAO Gemini Science Center, Chile

ROGER DAVIES, JORDI BARR

University of Oxford, United Kingdom

MARIANNE TAKAMIYA

University of Hawaii, Hilo, Hawaii, USA

AND

DAVID CRAMPTON

HIA, Canada

Accepted for publication in Astronomical Journal, November 30, 2004

ABSTRACT

We present a study of the stellar populations of galaxies in the cluster RXJ0152.7–1357 at a redshift of 0.83. The study is based on new high signal-to-noise spectroscopy of 29 cluster members covering the wavelength range 5000–10000Å as well as $r'i'z'$ photometry of the cluster.

We use scaling relations between the central velocity dispersions of the galaxies and their luminosities, Balmer line strengths and various metal line strengths to parameterize the differences between the members of RXJ0152.7–1357 and our low redshift comparison sample. The luminosities of the RXJ0152.7–1357 galaxies and the strengths of the higher order Balmer lines $H\gamma$ and $H\delta$ (for non-emission line galaxies) appear to be in agreement with pure passive evolution of the stellar populations with a formation redshift $z_{\text{form}} \approx 4$. However, the strengths of the D4000 indices and the metal indices do not support this interpretation. Compared to our low redshift comparison sample, the metal indices (C4668, Fe4383, CN3883, G4300 and CN_2) show that at least half of the non-emission line galaxies in RXJ0152.7–1357 have an α -element abundance ratio $[\alpha/\text{Fe}]$ of 0.2 dex higher, and about half of the galaxies have significantly lower metal content.

X-ray data have previously shown that RXJ0152.7–1357 is in the process of merging from two sub-clumps. We find that differences in stellar populations of the galaxies are associated with the location of the galaxies relative to the X-ray emission. The galaxies with weak C4668 and G4300, as well as galaxies for which weak [O II] emission indicates a very recent star formation episode involving about 1 per cent of the mass, are located in areas of low X-ray luminosity, on the outskirts of the two sub-clumps. It is possible that these galaxies are experiencing the effect of the cluster merger as (short) episodes of star formation, while the galaxies in the cores of the sub-clumps are unaffected by the merger.

The spectroscopy of the RXJ0152.7–1357 galaxies shows for the first time galaxies in a rich cluster at intermediate redshift that cannot evolve passively into the present day galaxy population in rich clusters. Additional physical processes may be at work and we speculate that merging with infalling (disk) galaxies in which stars have formed over an extended period might produce the required reduction in $[\alpha/\text{Fe}]$. However, the merging could not be accompanied by star formation involving a substantial mass fraction. We note that our conclusions, in part, rely on stellar population models for which the predictions of the indices in the rest frame blue have not yet been tested extensively.

Subject headings: galaxies: clusters: individual: RXJ0152.7–1357 – galaxies: evolution – galaxies: stellar content.

1. INTRODUCTION

Studies of nearby galaxies ($z < 0.05$) have shown that despite the complex processes involved in the formation and evolution of the galaxies (e.g. mergers, bursts of star formation, morphological changes), the global properties of the

galaxies follow very tight empirical scaling relations. Spiral galaxies follow the Tully-Fisher (TF) relation (Aaronson et al. 1986), which is a relation between total magnitude and rotational velocity. Elliptical (E) and lenticular (S0) galaxies follow the Fundamental Plane (FP) (Dressler et al. 1987; Djorgovski & Davis 1987; Jørgensen et al. 1996), which is a relation between the effective radius, the mean surface brightness within that radius and the central velocity dispersion. The FP may be interpreted as a relation between the masses and the mass-to-light (M/L) ratios of the galaxies. For E and S0

Electronic address: ijorgensen@gemini.edu
Electronic address: mbergmann@ctio.noao.edu
Electronic address: rld@astro.ox.ac.uk, jmb@astro.ox.ac.uk
Electronic address: takamiya@hawaii.edu
Electronic address: david.crampton@nrc.ca

galaxies the absorption line strengths ($H\beta$, Mgb , and (Fe)) as well as the colors are correlated with the central velocity dispersions of the galaxies (Bender et al. 1993; Jørgensen 1997; Colless et al. 1999).

Several authors have used single-stellar population (SSP) models to derive luminosity weighted mean ages and metal contents from the line strengths. Such analysis shows that at a given velocity dispersion metal rich cluster E and S0 galaxies are younger than metal poor galaxies, and that many of the galaxies have experienced star formation within the last ≈ 3 Gyr involving at least 10 per cent of the mass (Jørgensen 1999; Trager et al. 2000).

It is not possible to fully constrain the models for galaxy formation and evolution based on observations of one epoch ($z \approx 0$), only. Therefore, many different groups have studied galaxies at intermediate redshifts, typically up to $z \approx 0.8$ with a few studies reaching redshift one, in order to constrain the models for galaxy evolution.

The TF relation has been studied by, e.g., Vogt et al. (1996), Ziegler et al. (2002, 2003), Milvang-Jensen et al. (2003) and Böhm et al. (2004). The results are not all consistent, but in general very small offsets relative to the low redshift TF relations are found for cluster galaxies, while field galaxies show larger offsets. Ziegler et al. (2002) and Böhm et al. (2004) find for field spiral galaxies that the low mass galaxies show more evolution between $z = 1$ and the present than found for high mass spiral galaxies. They conclude that the evolution of the M/L ratios depends on the galaxy masses. All of the studies interpret the offsets relative to the TF relation as an offset in the luminosity. However, see Kannappan & Barton (2004) for a discussion of kinematic anomalies as the source of some offsets from the TF relation found a high redshifts.

The FP has been used to study the luminosity evolution of E and S0 galaxies as a function of redshift (e.g., Bender et al. 1998; van Dokkum et al. 1998; Jørgensen et al. 1999; Kelson et al. 2000; Ziegler et al. 2001; van Dokkum & Stanford 2003; Wuyts et al. 2004). The study by van Dokkum & Stanford is the first to establish the FP for cluster galaxies at $z > 1$. The luminosity evolution is usually interpreted within a model that assumes pure passive evolution of the galaxies. This means the stellar populations of the galaxies are assumed to evolve quiescently, with no additional star formation in the redshift interval that is studied. In this model, the only differences between the stellar populations at different redshifts are differences in ages equal to the differences in the lookback time for the various redshifts. All the studies of the FP as a function of redshift conclude that the change in the zero point of the FP is consistent with the assumption that E and S0 galaxies evolve passively from a high redshift, called the formation redshift, z_{form} . Most of the authors find that $z_{\text{form}} > 2$.

Some attempts have also been made to use other scaling relations for E and S0 galaxies. Bender et al. (1998) and Ziegler et al. (2001) used both the Mg_2 - σ relation and the FP, and concluded that both relations were in agreement with pure passive evolution. Kelson et al. (2001) studied the strength of the higher order Balmer lines, $H\delta$ and $H\gamma$, as a function of the galaxy velocity dispersion for four galaxy clusters with redshifts between 0.06 and 0.83. Kelson et al. conclude that the Balmer line strengths are in agreement with pure passive evolution and $z_{\text{form}} > 2.5$.

Apart from Kelson et al. (2000), Ziegler et al. (2001), and Wuyts et al. (2004), the rest of the studies have been restricted to quite small galaxy samples in each cluster, typically about 10 galaxies per cluster, covering a narrow range in luminosities.

With a narrow coverage in luminosities, and therefore in masses, these studies cannot address how the evolution may depend on galaxy mass. Further, the samples are usually selected such that the galaxies are on the red sequence of the color-magnitude relation and/or their morphologies are early-type (E or S0). Significant morphological evolution has been found between redshift ≈ 0.5 and the present showing that a substantial number of spiral galaxies must have evolved into E and S0 galaxies (e.g., Dressler et al. 1997). Therefore studying galaxy evolution by comparing E and S0 galaxies at redshifts between 0.2-1.0 to those at low redshift, is likely to give a biased impression of the actual evolution of the galaxies since part of the E and S0 galaxy population at low redshift originates from galaxies not included in the higher redshift samples. This ‘‘progenitor bias’’ is discussed in detail by van Dokkum & Franx (2001). While it is difficult to identify which high redshift galaxies lead to which low redshift descendants, a safer assumption may be that the whole cluster population at high redshift leads to the cluster population at low redshift. This assumption ignores any cluster infall occurring between redshift ≈ 1 and the present that may change the populations of cluster galaxies. However, to some extent the problem of the ‘‘progenitor bias’’ may be addressed by studying representative samples of the full population of cluster galaxies.

Two of the major variables that determine the physical processes a galaxy will undergo during its evolution are mass and environment. Other major variables like the gas content may depend on the mass and the early evolution of the galaxy. Detailed information about how the galaxy evolution depends on the mass can be used to constrain the formation scenarios, i.e. hierarchical versus monolithic collapse (e.g., Kauffmann & Charlot 1998). The scaling relations with low scatter represent very powerful tools to address these questions, since we can measure as a function of galaxy size, mass, luminosity and central velocity dispersion how the galaxies follow or deviate from the mean relations and how the relations may change with epoch reflecting the evolutionary paths of the galaxies. Typical model predictions show changes in the slopes of the scaling relations as a function of redshift of ≈ 10 per cent between $z = 1$ and the present (Ferreras & Silk 2000a). However, empirically larger changes are found, e.g., Ziegler et al. (2002) find a 35 per cent change in the slope of the TF relation between $z = 1$ and the present. For nearby galaxies, Concanon et al. (2000) find that low mass galaxies have a larger age spread than high mass galaxies. Their result as well as a recent study of Abell 851 at $z = 0.41$ (Ferreras & Silk 2000b) indicate that the evolutionary paths depend significantly on the galaxy mass, and that these differences should be detectable in samples that reach luminosities of one to two magnitudes fainter than L^* .

From these considerations follow four requirements for a galaxy sample selected for a detailed study of galaxy evolution as a function of epoch and mass: (1) Large coverage in luminosity, (2) sufficient number of galaxies at each epoch to accurately determine the slopes of the scaling relations, (3) sufficient number of epochs to detect the possible changes in slopes with redshift, and (4) consistent coverage in distance from the cluster center at different epochs such that we can differentiate between effects due to galaxy mass and due to cluster environment.

In Section 2 we describe the science objectives and methods of our project, ‘‘The Gemini/HST Galaxy Cluster Project’’, which is designed following the above listed requirements.

The remainder of the paper is based on photometry and spectroscopy of galaxies in the cluster RXJ0152.7–1357 and addresses a subset of the analysis and questions outlined in Section 2. Section 3 gives background information about the galaxy cluster RXJ0152.7–1357. The observational data for the galaxies in RXJ0152.7–1357 are described in Section 4, with further details given in the Appendix. Our low redshift comparison sample is briefly described in Section 5. In Section 6 we describe the stellar population models and the evolutionary scenarios that we use for interpreting the data. Section 7 discusses the cluster sub-structure in RXJ0152.7–1357. In Section 8 we focus on the properties of the stellar populations in the RXJ0152.7–1357 galaxies. In Section 9 we discuss the stellar populations in the context of the cluster sub-structure and in the context of the evolutionary scenarios. Section 10 summarizes the conclusions. Throughout this paper we adopt a Λ CDM cosmology with $H_0 = 70 \text{ km s}^{-1} \text{ Mpc}^{-1}$, $\Omega_M = 0.3$, and $\Omega_\Lambda = 0.7$.

2. THE GEMINI/HST GALAXY CLUSTER PROJECT

This paper is the first in a series from “The Gemini/HST Galaxy Cluster Project”, aimed at studying galaxy evolution during half the age of the Universe. The science objective of the project is to establish the star formation history for galaxies in rich clusters as a function of galaxy mass. Among the questions that we aim to address are (1) the role and duration of star formation episodes, (2) the links between morphological evolution and the evolution of the stellar populations, (3) the presence of possible variations in the initial-mass-function (IMF), (4) sub-structure of the clusters and the location of galaxies containing young stellar populations.

The sample consists of 15 X-ray selected rich galaxy clusters covering a redshift interval from $z = 0.15$ to $z = 1.0$; we adopt a lower limit on the X-ray luminosity of $L_X(0.1 - 2.4 \text{ keV}) = 2 \cdot 10^{44} \text{ erg s}^{-1}$. A full description of the selection of galaxy clusters and sample selection for the spectroscopic samples in each of the clusters will be presented in Jørgensen et al. (in preparation).

Our observing strategy is as follows. We obtain optical photometry in three or four filters with the Gemini Multi-Object Spectrograph (GMOS) on either Gemini North or Gemini South. See Hook et al. (2004) for a description of GMOS. For each cluster we cover approximately the central $1.7 \text{ Mpc} \times 1.7 \text{ Mpc}$, which for the adopted cosmology is about $1^\circ \times 1^\circ$ at the distance of the Coma cluster, and $3.7 \text{ arcmin} \times 3.7 \text{ arcmin}$ at the distance of RXJ0152.7–1357. The photometry is used to select the spectroscopic sample, which includes all galaxies that are likely to be members of the cluster. The selection is based on color-magnitude diagrams as well as color-color diagrams. Of special importance is that no morphological selection criteria are applied to the spectroscopic sample. For each cluster we obtain high signal-to-noise (S/N) optical spectroscopy of 30 to 50 cluster members using GMOS. The S/N of the spectra is typically higher than 25 per Ångstrom in the rest frame of the galaxies. The spectra are used for determining the redshift, the central velocity dispersion of each galaxy, and line indices for absorption lines (Balmer lines as well as several metal lines). We measure line indices for enough absorption lines to be able to study differences in ages, metallicities, and α -element abundance ratios $[\alpha/\text{Fe}]$. For galaxies with emission lines, we also determine the equivalent width of these. Hubble Space Telescope (HST) imaging obtained with either the Wide Field and Planetary Camera 2 or the Advanced Camera for

TABLE 1
INSTRUMENTATION

Telescope	Gemini North
Instrument	GMOS-N
CCDs	$3 \times \text{EEV } 2048 \times 4608$
r.o.n. ^a	$(3.5, 3.3, 3.0) \text{ e}^-$
gain ^d	$(2.10, 2.337, 2.30) \text{ e}^-/\text{ADU}$
Pixel scale	$0.0727 \text{ arcsec/pixel}$
Field of view	$5'5 \times 5'5$
Imaging filters	$r' i' z'$
Grating	R400_G5305
Spectroscopic filter	OG515_G0306
Slit width	1 arcsec
Slit length	5 – 14 arcsec
Extraction aperture	$1 \text{ arcsec} \times 1.15 \text{ arcsec}$
r_{ap}^b	0.62 arcsec
Spectral resolution ^c , σ	3.065 \AA
Wavelength range ^d	5000–10000 Å

^aValues for the three detectors in the array.

^bRadius of equivalent circular aperture, see Jørgensen et al. (1995)

^cMedian of the resulting resolutions, each derived as sigma in a Gaussian fit to the sky lines in stacked spectra. The resolution is equivalent to $\sigma = 116 \text{ km s}^{-1}$ at 4300 \AA in the rest frame of RXJ0152.7–1357.

^dThe exact wavelength range varies from slit-let to slit-let.

Surveys (ACS) is used to derive 2-dimensional surface photometry of the galaxies. We use available archive data, as well as data obtained specifically for this project.

We use a two-tiered approach in the analysis of the observational data. We establish scaling relations between observable parameters (effective radii, surface brightnesses, magnitudes, velocity dispersions and absorption line strengths), and we use the spectra to derive mean ages, metal content and abundance ratios using stellar population models.

The scaling relation zero points track the bulk differences in the stellar populations. Because most of the scaling relations have either the galaxy mass or the velocity dispersion as the independent parameter, changes in the slope of a scaling relation reflect differences in the stellar populations as a function of galaxy mass or velocity dispersion. Finally, the internal scatter of the scaling relations reflect the variations in star formation history within a given sample of galaxies. The most obvious groupings of galaxies are of course groupings with respect to redshift. Other groupings make use of information about the cluster environment, cluster sub-structure, or galaxy morphology.

Using stellar population models like those recently published by Thomas et al. (2003, 2004) we can derive luminosity weighted mean ages, metal content and abundance ratios, specifically the α -element abundance ratio. Most other models do not vary the α -element abundance ratio, but assume that it is solar. This is a significant limitation of the models since data for nearby E and S0 galaxies show an α -element enhancement of $[\alpha/\text{Fe}] \approx 0.2$ (e.g., Worthey et al. 1992; Davies et al. 1993; Jørgensen 1999; Trager et al. 2000).

3. RXJ0152.7–1357: BACKGROUND INFORMATION

The massive cluster of galaxies RXJ0152.7–1357 was discovered from *ROSAT* data by three different surveys: The *ROSAT* Deep Cluster Survey (RDCS) and the Wide Angle *ROSAT* Pointed Survey (WARPS) (see Ebeling et al. 2000 for the historical account), as well as the Bright Serendipitous

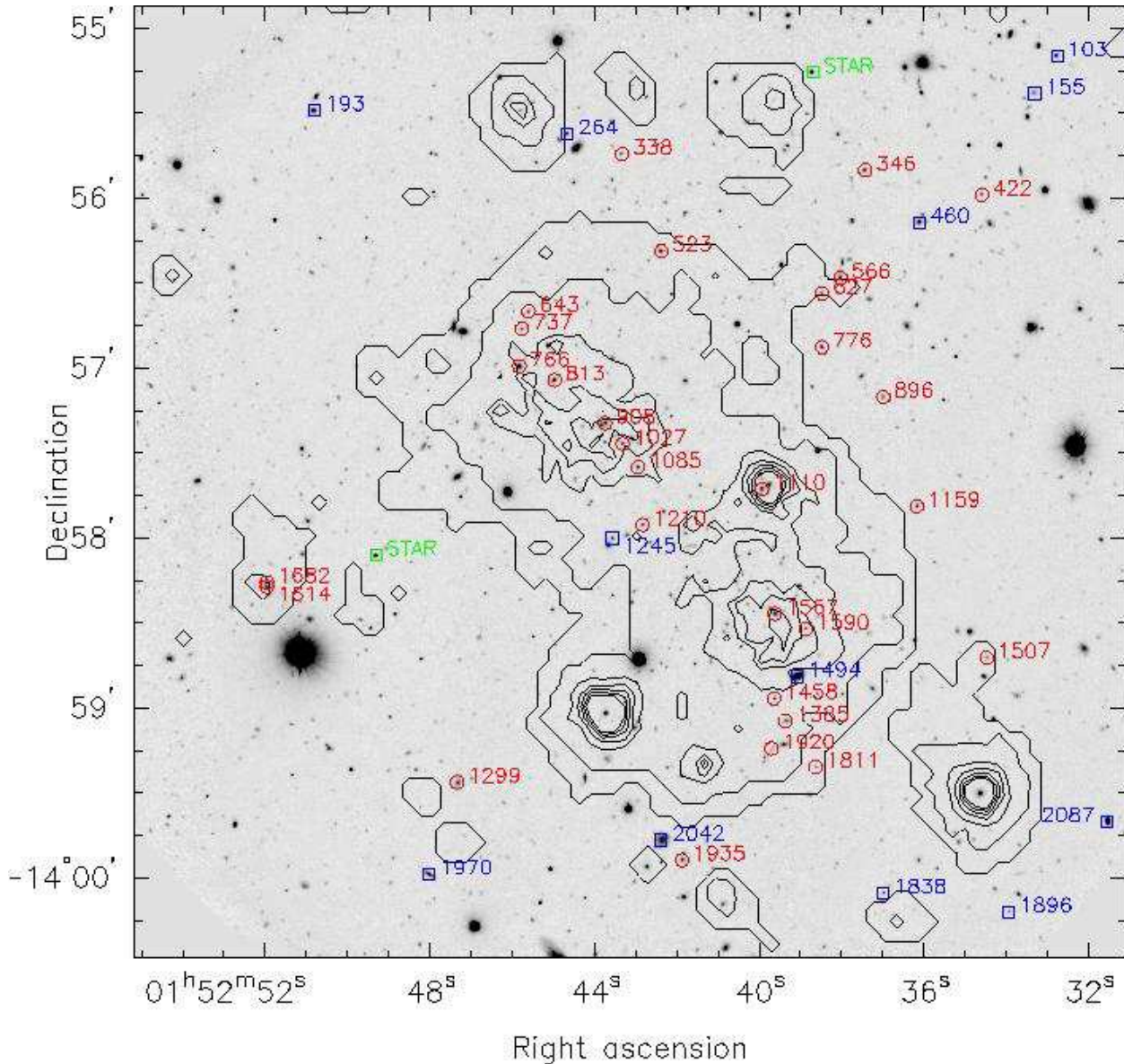


FIG. 1.— RXJ0152.7–1357 i' -band image with contours of the *XMM-Newton* data overlaid. The image covers approximately $5.5 \text{ arcmin} \times 5.5 \text{ arcmin}$. Red circles – confirmed cluster members labeled with their ID number; blue boxes – non-members with spectroscopy labeled with their ID number; green boxes – the two blue stars included in the mask. The X-ray image is the sum of the images from the two *XMM-Newton* EPIC-MOS cameras. The X-ray image has been smoothed such that the structure seen is significant at the 2.5σ level or higher. The spacing between the contours is logarithmic with a factor 1.5 between each contour.

High-Redshift Archival Cluster (SHARC) survey (Nichol et al. 1999). Further X-ray observations of the cluster have been carried out with *BeppoSAX* (Della Ceca et al. 2000), *XMM-Newton* and *Chandra* (Jones et al. 2004; Maughan et al. 2003). The data from *XMM-Newton* and *Chandra* show two sub-clumps and support the view that RXJ0152.7–1357 is in the process of merging from two clumps of roughly equal mass, see Figure 1 that shows the *XMM-Newton* data together with our i' -band image of the cluster. This figure is discussed further in Section 7. The total mass of the cluster is estimated to be similar to that of the Coma cluster (Maughan et al. 2003).

Redshifts of six galaxies in RXJ0152.7–1357 have been published by Ebeling et al. (2000), giving the cluster redshift of 0.833. Ellis & Jones (2004) have studied the K-band luminosity function of this cluster as well as two

other massive high redshift clusters, RXJ1226.9+3332 and RXJ1415.1+3612. They find the luminosity functions to be consistent with passive evolution and a formation redshift of $z_{\text{form}} \approx 1.5 - 2.0$.

4. OBSERVATIONAL DATA

Imaging and spectroscopy of RXJ0152.7–1357 were obtained with GMOS-N in semester 2002B. The observations were done in queue in the period from UT 2002 July 18 to UT 2002 September 25. The data were obtained as part of Gemini programs GN-2002B-Q-29 (a queue program) and GN-2002B-SV-90 (an engineering program). Table 1 summarizes the instrument information, while Tables 2 and 3 summarize the imaging and spectroscopic data, respectively.

The imaging covers one GMOS-N field, which is approximately $5.5 \text{ arcmin} \times 5.5 \text{ arcmin}$. Imaging was obtained in

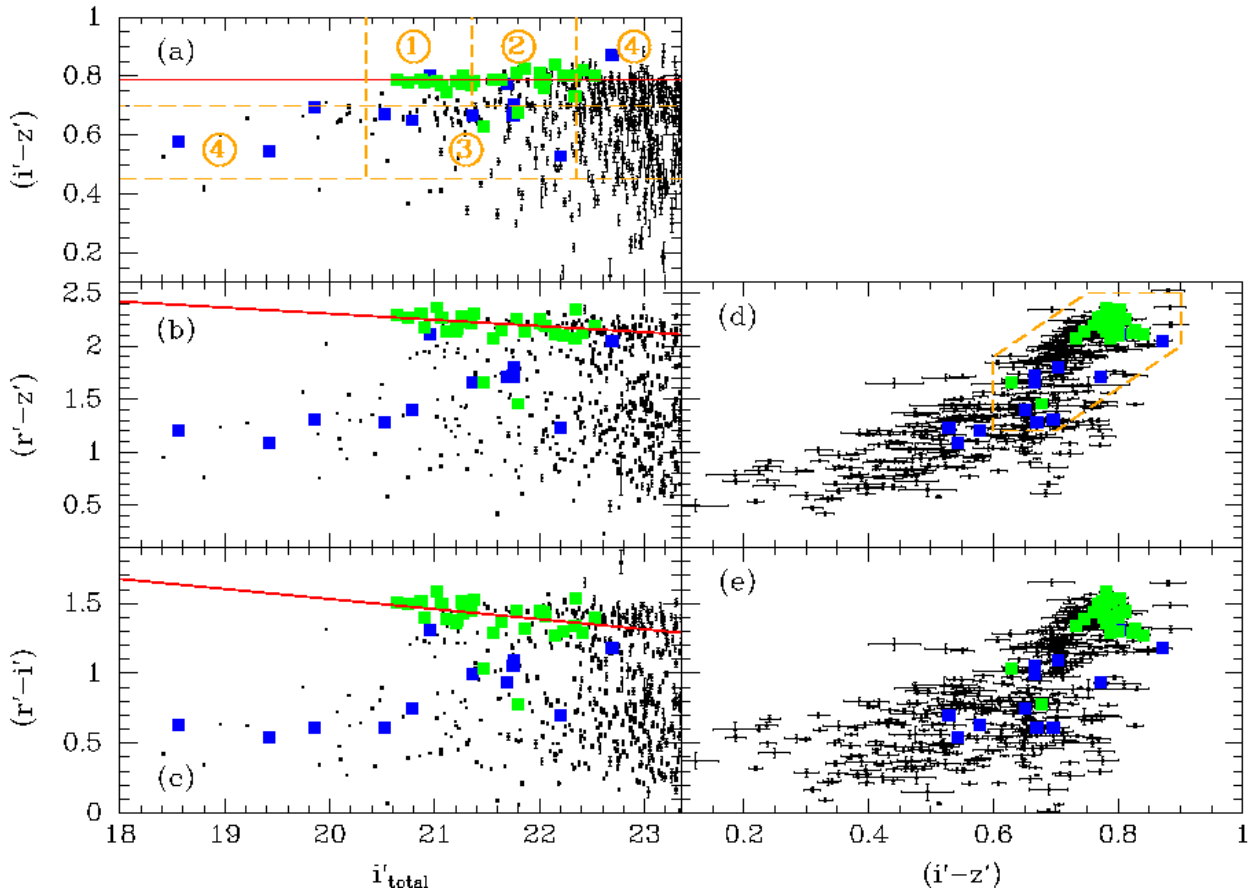


FIG. 2.— RXJ0152.7–1357: Color-magnitude and color-color diagrams. Only galaxies ($class_star < 0.80$ in the i' filter) with $i' < 23.35$ mag are shown. The magnitudes are the total magnitudes, while all colors are aperture colors. The photometry has been corrected for the galactic extinction, see Section 4.1. Green filled boxes – confirmed cluster members in our spectroscopic sample; blue filled boxes – non-members with spectroscopy; small points with error bars – galaxies without spectroscopy. Red lines – least squares fit to the data for the cluster members, excluding the two bluest galaxies. The slope for the color-magnitude relation for $(i' - z')$ is not significantly different from zero, thus the line marks the median color for the galaxies. The orange dashed lines and circled numbers in panel (a) show the object classes, see Section 4.2. The orange dashed lines on panel (d) outline the sample limits in the colors that would have been used if photometry in all three passbands had been available at the time of the sample selection, see Section 4.2 for discussion.

TABLE 2
GMOS-N IMAGING DATA

Filter	Exposure time	Image quality ^a arcsec	Sky brightness mag arcsec ⁻²
r'	$12 \times 600\text{sec}$	0.68	20.65
i'	$7 \times 450\text{sec}$ (dark sky) $+ 100 \times 120\text{sec}$ (bright sky)	0.56	19.63
z'	$13 \times 450\text{sec}$ (dark sky) $+ 14 \times 450\text{sec}$ (bright sky)	0.59	19.16

^aAverage FWHM of 7-10 stars in the field.

three filters. One GMOS mask was used for the spectroscopy. We used the R400 grating and a slit width of 1 arcsec, resulting in an instrumental resolution of 116 km s^{-1} at 4300 \AA in the rest frame of RXJ0152.7–1357, see Table 1. The spectroscopic observations were obtained as 25 individual exposures with exposure time from 2000 to 3600 sec. The total exposure time was ≈ 21.7 hours. Spectroscopy was obtained of 41 galaxies, 29 of which are cluster members. See Section 7 for the definition of cluster membership. For the cluster members, the median S/N is 31 per \AA in the rest frame

of the galaxies, derived in the rest frame wavelength interval $4100\text{-}4600 \text{ \AA}$. The S/N for the individual galaxies are listed in Table A12 in the appendix. Three cluster members have S/N less than 20 per \AA (ID 896, 1811, and 1920), two of these are emission line galaxies.

4.1. Imaging reductions and derived photometric parameters

The basic reductions of the data were done using a combination of the Gemini IRAF package and custom reduction techniques. The Gemini IRAF package is an external package built on core IRAF¹. The details of the reductions are described in the Appendix. The final imaging data products are the cleaned and averaged images in each filter, normalized to one of the exposures taken in photometric conditions, these images are in the following referred to as the “co-added images”.

The co-added images were processed with SExtractor v.2.1.6 (Bertin & Arnouts 1996). The details are described

¹ IRAF is distributed by National Optical Astronomy Observatories, which is operated by the Association of Universities for Research in Astronomy, Inc., (AURA), under cooperative agreement with the National Science Foundation, USA. The Gemini IRAF package is distributed by Gemini Observatory, which is operated by AURA.

TABLE 3
GMOS-N SPECTROSCOPIC DATA

Data set	Exposure time	Image quality ^a		
		at 7000Å (arcsec)	at 8000Å (arcsec)	at 9000Å (arcsec)
$\lambda_{\text{central}} = 8050\text{Å}$	48800 sec (15 exposures)	0.67	0.63	0.58
$\lambda_{\text{central}} = 8150\text{Å}$	29160 sec (10 exposures)	0.70	0.67	0.64
Combined	77960 sec (25 exposures)	0.68	0.65	0.60

^aAverage FWHM measured from the two blue stars included in the mask.

in the Appendix. We adopt the best magnitudes (*mag_best*) from SExtractor as the total magnitudes of the objects. Aperture magnitudes and colors were derived within apertures with a diameter of 1.16 arcsec, which is approximately twice the FWHM of the point-spread-function of the images. From model galaxies with exponential and $r^{1/4}$ -profiles, and with sizes matching our spectroscopic sample, we have found that the colors ($r' - i'$) and ($r' - z'$) are affected by no more than 0.03 due to the small differences in FWHM of the images in the different filters. The FWHM difference makes the colors systematically too red. For ($i' - z'$) the effect is less than 0.005. In all cases the effect does not affect our analysis. In the following we use the total magnitudes together with the aperture colors.

For the galaxies in the spectroscopic sample, the typical internal uncertainties on the magnitudes and colors due to photon noise only are 0.007 mag and 0.01, respectively. The observations in the i' -filter were obtained as two independent sets, one obtained in dark time and the other in bright time. We compare photometry derived from these two data sets and use this comparison to estimate the uncertainties on the photometry introduced by flat fielding, fringe correction and differences in seeing. We compare the total magnitudes as well as the aperture magnitudes derived from the two data sets. All comparisons are done for objects with $class_star < 0.80$. From the rms scatter in the comparisons, we find that for $i' < 21.5$ mag the uncertainties on the total magnitudes and the colors are 0.035 mag and 0.045, respectively. For $21.5 < i' \leq 22.5$ mag the uncertainties are 0.06 and 0.07. The standard calibration of the photometry is described in the Appendix. In general the uncertainties on the calibrations are between 0.04 mag and 0.05 mag due to the scatter in the relations used for the standard calibration. Table A10 in the Appendix lists the photometry for the spectroscopic sample.

The galactic extinction in the direction of RXJ0152.7–1357 is $A_B = 0.064$ (Schlegel et al. 1998). We use the effective wavelength of the three filters in which the photometry was obtained, and the calibration from Cardelli et al. (1989) to derive the extinction $A_r = 0.042$; $A_i = 0.033$; $A_z = 0.027$. The data in Table A10 have not been corrected for galactic extinction. Two-dimensional surface photometry and the morphologies of the galaxies in the cluster will be the topic of a future paper.

4.2. Spectroscopic sample selection

The spectroscopic sample was selected based on the photometry. Stars and galaxies were separated using the SExtractor classification parameter *class_star* derived from the image in the i' -filter. For the purpose of selecting targets for the spectroscopic observations we chose a threshold of 0.80,

i.e., objects with $class_star < 0.80$ in the i' -image are considered galaxies. This limit may result in very compact galaxies being excluded from the sample. However, it was more important for the planning of our observations to ensure that all targets for the spectroscopic observations were indeed galaxies. Based on the total magnitude in i' and the colors we then define four classes of objects. At the time of the sample selection, only photometry in i' filter and the z' filter was available. We use a color selection that includes all likely cluster members. We then define object classes as follows.

- 1: $20.35 \leq i' \leq 21.35 \wedge (i' - z') \geq 0.7$
- 2: $21.35 < i' \leq 22.35 \wedge (i' - z') \geq 0.7$
- 3: $20.35 \leq i' \leq 22.35 \wedge 0.45 \leq (i' - z') < 0.7$
- 4: $(i' < 20.35 \wedge 0.45 \leq (i' - z') < 0.7) \vee (i' > 22.35 \wedge (i' - z') \geq 0.7)$

Figure 2 summarizes the photometry for the field as color-magnitude diagrams and color-color diagrams. The spectroscopic sample is marked, cluster members as solid green boxes. The object classes are visualized on Figure 2a. The star-galaxy classification parameter *class_star* in the i' -filter is 0.02–0.04 for all the galaxies in the spectroscopic sample.

Objects in class 1 and 2 are equally important to include in the spectroscopic sample. We aimed at including roughly the same number of galaxies from each of these two classes. Class 3 objects are likely to include blue cluster members. These were observed when no class 1 or 2 object was available for a given position in the mask. Due to the distribution of the class 1, 2 and 3 objects in the field, not all of the available space in the mask could be filled with these. We therefore included objects from class 4 in order to fill the mask. The bright class 4 galaxies are expected to all be foreground galaxies. The faint class 4 galaxies are expected to include cluster members.

It turned out that most of the observed galaxies from class 3 were in fact foreground galaxies. All of the observed bright galaxies from class 4 were indeed foreground galaxies. Two of the three faint galaxies observed from class 4 were cluster members.

Because only i' and z' band photometry was available at the time of the sample selection for the spectroscopy, it is relevant to assess if this has significantly biased the sample selection. Figure 2d shows the outline of the limits in the color-color diagram that we would have used for the sample selection, had the r' band photometry been available at that time. These limits are similar to those used for observations of other clusters in our sample. It should be noted that to ensure that we did not exclude blue cluster members, the blue limit actually

used for the class 3 objects was at a smaller ($i' - z'$) than we would have used if the r' band photometry had been available. There are three galaxies in the spectroscopic sample outside the limits shown on Figure 2d. Two of these are bright galaxies in class 4. These were already expected not to be cluster members, and were only included in the sample in order to fill the mask. The third galaxy (also a foreground galaxy) would probably not have been included in the sample, and another target would have been included. The rest of the sample selection is unaffected by the lack of r' photometry. We conclude that the sample selection based on i' and z' , only, was not significantly biased relative to what we would have done using photometry in all three passbands.

The spectroscopic sample is marked on Figure 1, cluster members as circles. Two blue stars were included in the mask in order to obtain a good correction for the telluric absorption lines. These two stars are also marked on Figure 1.

4.3. Spectroscopic reductions and derived spectroscopic parameters

The details of the reductions of the spectroscopic data are described in the Appendix. The final data products are cleaned and averaged spectra that have been wavelength calibrated and also calibrated to a relative flux scale. Both extracted one-dimensional (1D) and the 2-dimensional spectra are kept after the basic reductions. However, in this paper we use only the 1D spectra.

The co-added 1D spectra were used for deriving the redshifts, velocity dispersions, absorption line indices, and emission line equivalent widths of the galaxies. The details are described in the Appendix. Here we summarize the most important points.

The redshifts and the velocity dispersions were determined by fitting a mix of three template stars to the spectra. We used software made available by Karl Gebhardt. The software uses penalized maximum likelihood fitting in pixel space to determine the velocity dispersion and the redshift, see Gebhardt et al. (2000, 2003) for a detailed description of the fitting method. The template stars were of spectral types K0III, G1V and B8V. Using multiple template stars limits any systematic effects in the derived velocity dispersions due to template mismatch. The velocity dispersions have been corrected for the aperture size using the technique from Jørgensen et al. (1995). Table A12 in the Appendix summarizes results from the template fitting. Measured velocity dispersions as well as aperture corrected velocity dispersions are listed for the cluster members. For galaxies that are not members of the cluster, we give the redshift. The detailed data for these galaxies will be discussed in a future paper.

The Lick/IDS absorption line indices CN_1 , CN_2 , G4300, Fe4383, C4668 (Worthey et al. 1994), as well as the higher order Balmer line indices $H\delta_A$ and $H\gamma_A$ (Worthey & Ottaviani 1997) were derived. We have also determined the D4000 index (Bruzual 1983; Gorgas et al. 1999), and the blue indices $CN3883$ and $CaHK$ (Davidge & Clark 1994). The indices have been corrected for the aperture size and for the effect of the velocity dispersions, see Appendix.

Seven of the cluster members have detectable emission lines. For these galaxies we determined the equivalent width of the [O II] $\lambda\lambda 3726, 3729$ doublet, in the following referred to as the “[O II] line”. With an instrumental resolution of $\sigma \approx 3 \text{ \AA}$ (FWHM $\approx 7 \text{ \AA}$), the doublet is not resolved in our spectra. With our wavelength coverage, the [O II] line is the only emission line that can be measured in the galaxies that are mem-

TABLE 4
LOW REDSHIFT COMPARISON DATA

Cluster	Redshift	N(log σ)	N(line indices)
Perseus	0.018	63	51
A0194	0.018	17	14
Coma	0.024	116	...

bers of RXJ0152.7–1357. Table A14 in the Appendix lists the derived line indices and the measurements of the [O II] equivalent widths.

5. LOW REDSHIFT COMPARISON DATA

The reference sample of galaxies at low redshift used in this paper consists of 63 galaxies in the Perseus cluster and 17 galaxies in the cluster Abell 194. Both clusters are at redshift $z = 0.018$. The Perseus sample covers the central $100 \text{ arcmin} \times 60 \text{ arcmin}$ of the cluster. For E and S0 galaxies determination of line indices the sample is 96 per cent complete to $B=16.05 \text{ mag}$ (absolute B-band magnitude of -18.4 mag). The Abell 194 sample is not complete, but covers galaxies of similar luminosities. The data for these two clusters will be published and discussed in detail in a future paper. We also use the velocity dispersions and photometry for the Coma cluster galaxies from Jørgensen (1999). This sample contains 116 galaxies with measurements of the velocity dispersions. The sample covers the central $64 \text{ arcmin} \times 70 \text{ arcmin}$ of the cluster. For E and S0 galaxies the sample is 93 per cent complete to $B=16.2 \text{ mag}$ (absolute B-band magnitude of -18.9 mag). All of the galaxies in the low redshift sample are on the red sequence of the color-magnitude relation and are classified as early-type (E or S0). Table 4 summarizes the low redshift comparison data.

The measurement techniques used for the low redshift comparison data are identical to those used for our RXJ0152.7–1357, except for the measurements of the velocity dispersions of the Coma cluster galaxies. The velocity dispersions for the Coma cluster galaxies were derived using a Fourier Fitting Technique, rather than fitting in pixel space. The line-of-sight velocity distribution for the fits were assumed to be Gaussian. Further, a small fraction of the Coma cluster velocity dispersions comes from earlier published data. Jørgensen (1999) calibrated all the Coma cluster velocity dispersions to a consistent system. We use the data as given in that paper. We have tested the consistency of the velocity dispersions of the Coma cluster galaxies with those of the Perseus cluster by comparing the relation between M_{gb} and the velocity dispersions for the two clusters. Under the assumption that this relation is the same for the two clusters, we find that the velocity dispersions are consistent within $\Delta \log \sigma = 0.026$. We use this value as a measure of the systematic errors that may affect our results due to possible inconsistent calibration of the velocity dispersion measurements. Because of the similar measurement techniques used for all other parameters, we will assume that the systematic errors in the velocity dispersion will dominate over possible systematic errors in other parameters.

6. STELLAR POPULATION MODELS AND EVOLUTIONARY SCENARIOS

In this section we first describe the SSP models that we have chosen to use. We then discuss the difficulty of us-

TABLE 5
PREDICTIONS FROM SINGLE STELLAR POPULATION MODELS

Relation (1)		rms (2)	Reference (3)
$\log M/L_B$	$= 0.935 \log \text{age} + 0.337[M/H] - 0.053$	0.022	Maraston 2004
$\log M/L_B$	$= 0.833 \log \text{age} + 0.409[M/H] + 0.162$	0.013	Vazdekis-2000
D4000	$= 0.730 \log \text{age} + 0.711[M/H] + 1.827$	0.052	Vazdekis-2000
CN3883	$= 0.173 \log \text{age} + 0.142[M/H] + 0.086$	0.012	Bruzual & Charlot 2003
$\log \text{CaHK}$	$= 0.073 \log \text{age} + 0.061[M/H] + 1.291$	0.010	Bruzual & Charlot 2003
$(H\delta_A + H\gamma_A)'$	$= -0.115 \log \text{age} - 0.095[M/H] + 0.095[\alpha/\text{Fe}] + 0.009^a$	0.008	Thomas et al.
$\log H\beta_G$	$= -0.221 \log \text{age} - 0.114[M/H] + 0.055[\alpha/\text{Fe}] + 0.500$	0.010	Thomas et al.
CN ₂	$= 0.121 \log \text{age} + 0.196[M/H] + 0.066[\alpha/\text{Fe}] - 0.043$	0.025	Thomas et al.
$\log G4300$	$= 0.162 \log \text{age} + 0.163[M/H] + 0.114[\alpha/\text{Fe}] + 0.552$	0.029	Thomas et al.
$\log \text{Fe4383}$	$= 0.220 \log \text{age} + 0.342[M/H] - 0.363[\alpha/\text{Fe}] + 0.512$	0.022	Thomas et al.
$\log C4668$	$= 0.145 \log \text{age} + 0.581[M/H] + 0.023[\alpha/\text{Fe}] + 0.529$	0.037	Thomas et al.
$\log \text{Mgb}$	$= 0.173 \log \text{age} + 0.309[M/H] + 0.210[\alpha/\text{Fe}] + 0.354$	0.019	Thomas et al.
$\log(\text{Fe})$	$= 0.113 \log \text{age} + 0.253[M/H] - 0.278[\alpha/\text{Fe}] + 0.343$	0.007	Thomas et al.

NOTE. — (1) Relation established from the published model values. $[M/H] \equiv \log Z/Z_\odot$ is the total metallicity relative to solar. $[\alpha/\text{Fe}]$ is the abundance of the α -elements relative to iron, and relative to the solar abundance ratio. The age is in Gyr. The M/L ratios are stellar M/L ratios in solar units. (2) Scatter of the model values relative to the relation. (3) Reference for the model values.

^a $(H\delta_A + H\gamma_A)' \equiv -2.5 \log(1 - (H\delta_A + H\gamma_A)/(43.75 + 38.75))$, cf. Kuntschner (2000). The rms for the relation translates to an rms of $H\delta_A + H\gamma_A$ of ≈ 0.65 for the typical values of $H\delta_A + H\gamma_A$.

ing these models to derive luminosity weighted ages, metal content $[M/H]$, and the abundance ratios of the α -elements $[\alpha/\text{Fe}]$. Finally, we outline the simple evolutionary scenarios that we will reference in the analysis of the data.

6.1. Single stellar population models

In order to interpret the spectroscopic data we use SSP models. Most SSP models in the literature assume abundance ratios in agreement with the stars in the solar neighborhood. We refer to these as models using “solar abundance ratios”, though strictly speaking the abundance ratios may not be solar for the low metallicity models tied to the abundance ratios of the stars in the solar neighborhood. Since nearby E and S0 galaxies are known to have non-solar abundance ratios, specifically the α -elements are over-abundant relative to iron compared to solar abundances, we have chosen to use the models from Thomas et al. (2003, 2004).

Thomas et al. model the Lick/IDS indices for ages between 1 Gyr and 15 Gyr and total metallicities $[M/H]$ between -2.25 and 0.67 , and they include non-solar abundance ratios for the α -elements. Models are available for $[\alpha/\text{Fe}] = 0.0, 0.2, 0.3$ and 0.5 . The M/L ratios for the $[\alpha/\text{Fe}] = 0.0$ models are published by Maraston (2004). The models from Thomas et al. (2003, 2004) treat the elements N, O, Mg, Ca, Na, Ne, S, Si, and Ti as α -like elements, though N is not an α -element. $[\alpha/\text{Fe}]$ from these models should be interpreted as the abundance of these elements relative to the iron-peak elements Cr, Mn, Fe, Co, Ni, Cu, and Zn. The abundance of carbon is kept fixed in the models. It is also important to keep in mind that while magnesium and oxygen are primarily produced by massive stars and redistributed into the ISM by SNe type II, elements like carbon and nitrogen primarily originate from intermediate mass stars and are redistributed into the ISM by these stars during their AGB phase. Therefore the time scale for the production of carbon and nitrogen is somewhat longer than that of magnesium and oxygen, though it is shorter than the timescale for production of the iron-peak elements, which primarily are produced by SNe type Ia. The reader is referred to, e.g., Chiappini et al. (2003), Sánchez-Blázquez et al. (2003) and Carretero et al. (2004) for discussions on the

evolution of the various element abundances and the implications for the galaxy assembly timescales. As a further caution, Thomas et al. model the effects of the non-solar $[\alpha/\text{Fe}]$ on the stellar atmospheres, using the results from Tripicco & Bell (1995). The models do not use evolutionary tracks for non-solar $[\alpha/\text{Fe}]$. Thus, strictly speaking the atmospheres of the models are inconsistent with the stellar interiors of the models. However, at the present we find that these models are the most useful for the interpretation of our data in terms of non-solar abundance ratios.

The indices CN3883, CaHK, and D4000 are not included in the models from Thomas et al. For D4000 we use models from Vazdekis et al. (1996). We use the updated 2000-models available on Vazdekis’ web-site. These models use new isochrones from Girardi et al. (2000). In the following we refer to the models as the Vazdekis-2000 models. The models assume solar abundance ratios, $[\alpha/\text{Fe}] = 0$. We use the Vazdekis-2000 models with a Salpeter (1955) IMF, in order to match the IMF used by Thomas et al. and Maraston. For CN3883 and CaHK, we use model spectra from Bruzual & Charlot (2003) for ages between 1 Gyr and 15 Gyr, and $[M/H]$ of $-0.4, 0.0$, and 0.4 , a Salpeter IMF and the Padova-1994 isochrones. These models also assume solar abundance ratios. We convolve the model spectra to the Lick/IDS resolution and derive the line indices using the same method as used for the observational data.

When we use the models together, we implicitly assume that the M/L ratios and the indices CN3883, CaHK, and D4000 do not depend on $[\alpha/\text{Fe}]$. For the M/L ratios, this may not be a valid assumption. Work by Thomas & Maraston (2003) indicates that the blue luminosity increases with increasing $[\alpha/\text{Fe}]$. However, these authors also conclude that the evolutionary tracks for non-solar $[\alpha/\text{Fe}]$ do not yet yield realistic ages for elliptical galaxies. They find that for tracks with non-solar $[\alpha/\text{Fe}]$ nearby elliptical galaxies become unrealistically old.

In order to interpret the offsets in the scaling relations in terms of differences in mean ages, metal content, and/or $[\alpha/\text{Fe}]$, we have used the published stellar population model values to establish linear relations between the observables

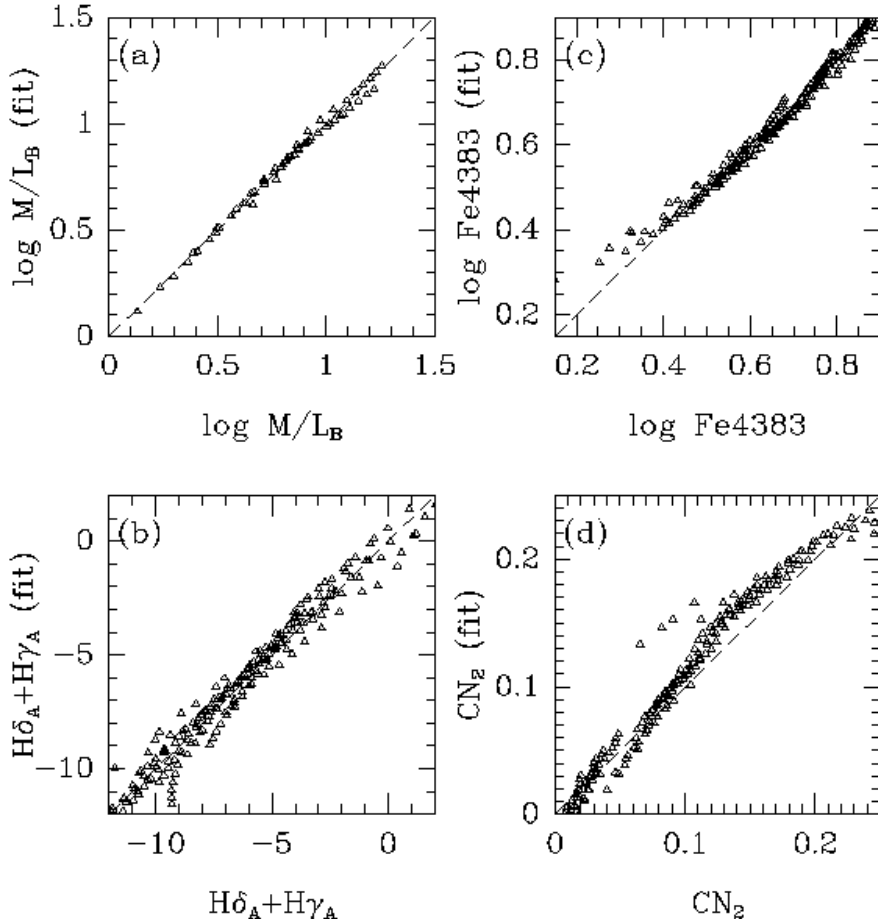


FIG. 3.— The model relations listed in Table 5 are shown as the values from the fit versus the actual model values. The lines are the one-to-one relations. If the fits were perfect representations of the models all the points would be on the one-to-one relations. Only for CN_2 does the fit deviate systematically from the actual model values, see text for discussion.

and those three parameters. The relations were derived as least squares fits with the residuals minimized in the measurable quantities, e.g. $\log M/L$, $D4000$ etc. The relations are listed in Table 5. For the models from Thomas et al. and Maraston, the models were fit for ages from 2 Gyr to 15 Gyr, and $[M/H]$ from -0.33 to 0.67 . All available $[\alpha/Fe]$ values for the models from Thomas et al. were included. The Vazdekis-2000 models were fit for $[M/H]$ from -0.68 to 0.2 and ages of 2-16 Gyr. For reference we give the linear relations for the M/L ratios based on both the Vazdekis-2000 and the Maraston models. The line indices derived from the Bruzual & Charlot models were fit for ages of 2-15 Gyr and $[M/H] = -0.4, 0.0, \text{ and } 0.4$. The relations listed for the “visible indices” Mgb , $\langle Fe \rangle$, and $H\beta_G$ are discussed in Section 6.2. The model values for $H\beta$ were converted to $H\beta_G$ using the calibration from Jørgensen (1997). Figure 3 shows the relations from Table 5 that are most important for our conclusions regarding differences in ages and $[\alpha/Fe]$. The fits for the M/L ratio, the higher order Balmer lines, and for Fe4383 show no systematic effects over the range in observable parameters relevant to our analysis. The fit for CN_2 shows a small systematic effect. The four points deviating most from the fit are the models for the most metal rich ($[M/H]=0.67$) and youngest (2 Gyr) populations. Further, CN_2 has a weak non-linear dependency on age for the highest metallicity mod-

els ($[M/H]=0.67$). The relation will lead to an underestimation of the age dependency for stellar populations with very high metallicities.

For the interpretation of the emission line equivalent widths, we use the models from Magris et al. (2003). These authors combine Bruzual & Charlot model spectra with emission line spectra from the photoionized gas around massive stars on the main sequence. We further combine these models with spectra of old stellar populations using the Bruzual & Charlot models. The details of this analysis are presented in Section 8.3.

6.2. Modeling visible and blue line indices

Ideally, we want to use the SSP models to derive luminosity weighted mean ages, metal content $[M/H]$, and the α -element abundance ratios $[\alpha/Fe]$ of the stellar populations in the galaxies. In the majority of studies of nearby galaxies, line indices in the visible region have been used for this purpose. Typically the indices Mg_2 (or Mgb), $\langle Fe \rangle$, and $H\beta$ have been used together with SSP models (e.g., Jørgensen 1999, Trager et al. 2000). We call these indices the “visible indices”. Figures 4a-c show the visible indices for our low redshift sample (Perseus and Abell 194) together with the SSP models from Thomas et al. (2003, 2004). All three indices depend on both age, $[M/H]$ and $[\alpha/Fe]$, but in different ways such that it is

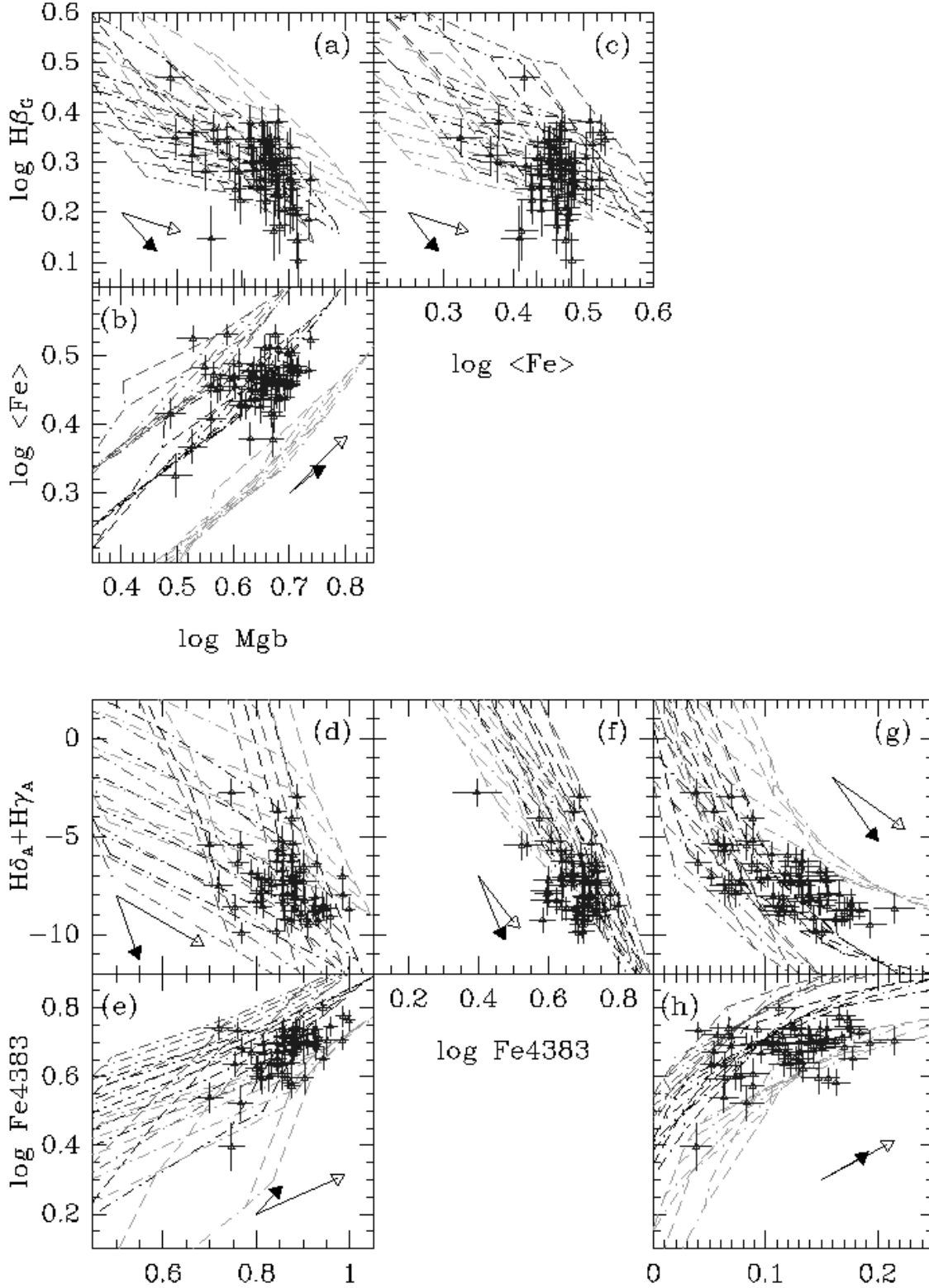


FIG. 4.— Line indices plotted versus each other, only the data for the Perseus and Abell194 sample are shown. Panels (a), (b), and (c) show the indices $H\beta$, Mgb , and $\langle \text{Fe} \rangle$, which are usually used in the visible wavelength region for investigation of ages, metal content and $[\alpha/\text{Fe}]$. Panels (d), (e), and (f) show the indices $H\delta_A + H\gamma_A$, C4668, and Fe4383, which are considered as an alternative to the indices in the visible region. Panels (g) and (h) show the index CN_2 which may be used in place of C4668. The SSP models from Thomas et al. (2003, 2004) are shown as model grids. We show the models for $[\alpha/\text{Fe}] = 0.0, 0.2$ and 0.5 , as red (dark grey), black and green (light grey) grids, respectively. Dashed lines – lines of constant $[\text{M}/\text{H}]$, for values of $-0.33, 0.0, 0.35$ and 0.67 . Dot-dashed lines – lines of constant ages, for values of $1, 2, 3, 5, 8, 11,$ and 15 Gyr. The arrows show the approximate changes in the indices for a change of $\Delta \log \text{age} = 0.3$ (solid arrow) and $\Delta [\text{M}/\text{H}] = 0.3$ (open arrow).

possible to derive these three parameters from the measured line indices with the aid of the SSP models. The derived values should always be interpreted as the luminosity weighted mean values.

For galaxies at redshift of about 0.6 or larger measuring the visible indices gets increasingly difficult as the wavelength regions for these indices are redshifted into the far red and often affected by the sky subtraction residuals due to the strong sky lines in this wavelength region. For galaxies in RXJ0152.7–1357, none of the visible indices can be measured reliably. We are therefore forced to use indices in the rest frame blue. We call these the “blue indices”. Thomas et al. (2003) discuss various such alternatives to the visible indices. Since ages, metallicities and abundance ratios derived for real galaxies using SSP models are luminosity weighted quantities, using indices in the rest frame blue instead of at longer wavelengths will give stronger weight to younger stellar populations that dominate the flux at short wavelengths. Thus, it becomes important when tracking the differences in ages, metallicities and abundance ratios to use a consistent set of line indices. However, for correct models of the various indices we would still expect tight correlations between the quantities derived using visible indices versus using blue indices.

In Figures 4d-h we show the blue indices for our low redshift sample together with the same SSP models from Thomas et al. (2003, 2004) as shown for the visible indices. The figure shows that the blue indices C4668 (or CN₂), Fe4383 and H δ_A + H γ_A , are not simply equivalent to the visible indices Mgb, $\langle\text{Fe}\rangle$, and H β . The blue indices depend in different ways on the age, [M/H] and $[\alpha/\text{Fe}]$. The dependencies for both the visible indices and the blue indices are summarized in Table 5. The Balmer lines primarily depend on the age, but the higher order Balmer lines have a stronger dependency on $[\alpha/\text{Fe}]$ than is the case for H β , as described by Thomas et al. The blue iron index Fe4383 has a strong age dependency. That combined with the $[\alpha/\text{Fe}]$ dependency of the higher order Balmer lines make the models in H δ_A + H γ_A versus Fe4383 almost degenerate. It is also clear that many of the galaxies have weaker Fe4383 for their Balmer line strength than predicted by any of the models. The index C4668 depends very little on $[\alpha/\text{Fe}]$, compared to its visible “equivalent” the Mgb index. Therefore, C4668 versus Fe4383 is less successful in separating the models according to abundance ratio, than found for Mgb versus $\langle\text{Fe}\rangle$. The CN₂ appears slightly more useful, but this index is weaker and more difficult to measure than C4668.

If we derive age, [M/H] and $[\alpha/\text{Fe}]$ from {Mgb, $\langle\text{Fe}\rangle$, H β } and from {C4668, Fe4383, H δ_A + H γ_A } using the SSP models, it turns out that the resulting values differ from each other in systematic ways. The general trends can be seen directly from Figure 4. The abundance ratio $[\alpha/\text{Fe}]$ based on the blue indices is systematically higher than when using the visible indices. This becomes most obvious when comparing the location of the data points relative to the model grids in Figures 4b and e (or h). The difference is about 0.15 dex. The metal content [M/H] resulting from the blue indices is slightly lower than when derived from the visible indices. On Figure 4, this can be seen by comparing panels (a) and (d), keeping the difference in $[\alpha/\text{Fe}]$ in mind. The resulting ages span the same range when using the two sets of indices, though there is no one-to-one correlation between the ages derived for the individual galaxies.

It is beyond the scope of the present paper to resolve these issues, which we believe are intrinsic to the SSP models. To our knowledge, there are no other published studies in which

the Thomas et al. SSP models have been used to derive age, [M/H] and $[\alpha/\text{Fe}]$ using the blue indices only. We have chosen not to present luminosity weighted mean ages, [M/H], and $[\alpha/\text{Fe}]$ derived from the blue indices. Instead we discuss the measured parameters for RXJ0152.7–1357 compared to the low redshift sample and to the SSP models. We primarily discuss the differences between the low redshift sample and the RXJ0152.7–1357 sample, rather than the absolute values of ages, [M/H], and $[\alpha/\text{Fe}]$.

6.3. Evolutionary scenarios

In order to simplify the analysis and discussion of our data, we will refer to some simple evolutionary scenarios the galaxies may experience between redshift 0.83 and the present. These scenarios do not represent an exhaustive list of possibilities, but serve as a framework for our discussion. The scenarios are as follows.

- (1) Pure passive evolution: In this scenario there is no additional star formation between $z = 0.83$ and the present. The stellar populations present at $z = 0.83$ simply age passively, while no other changes take place. The difference between the luminosity weighted mean ages of the stellar populations in the galaxies at $z = 0.83$ and the present is equal to the lookback time to $z = 0.83$ (7 Gyr with our adopted cosmology).
- (2) New star formation without galaxy mergers: Like scenario (1), the stellar populations already present at $z = 0.83$ age passively. In addition new stars are formed. Thus, the difference between the luminosity weighted mean ages of the stellar populations in the galaxies at $z = 0.83$ and the present is smaller than the lookback time to $z = 0.83$. There may also be differences in [M/H] and $[\alpha/\text{Fe}]$, depending on the details of the star formation.
- (3) Merging of galaxies and new star formation (perhaps limited to the galaxies affected by merging): The stellar populations already present at $z = 0.83$ age passively. As for scenario (2), due to the star formation the difference between the luminosity weighted mean ages of the stellar populations in the galaxies at $z = 0.83$ and the present is smaller than the lookback time to $z = 0.83$. There may be differences in [M/H] and $[\alpha/\text{Fe}]$, depending on the details of the star formation and the galaxies entering the mergers.
- (4) Merging of galaxies without new star formation: In this case, the details of the galaxies undergoing merging determine the differences in the luminosity weighted mean ages, [M/H] and $[\alpha/\text{Fe}]$ between the stellar populations at $z = 0.83$ and the present. However, since no new stars are formed we expect that the age difference is larger in this scenario than in scenario (3).

For all the scenarios, a potential complication is the sample selection and whether we succeed in observing the high redshift progenitors to the galaxies in the low redshift comparison sample. In the following we refer to scenario (1) as “passive evolution”. Only in this case is it always expected that the difference between luminosity weighted mean ages at $z = 0.83$ and the present is equal to the lookback time at $z = 0.83$. When we state that the data are not in agreement with the passive evolution model, it means that the differences between the

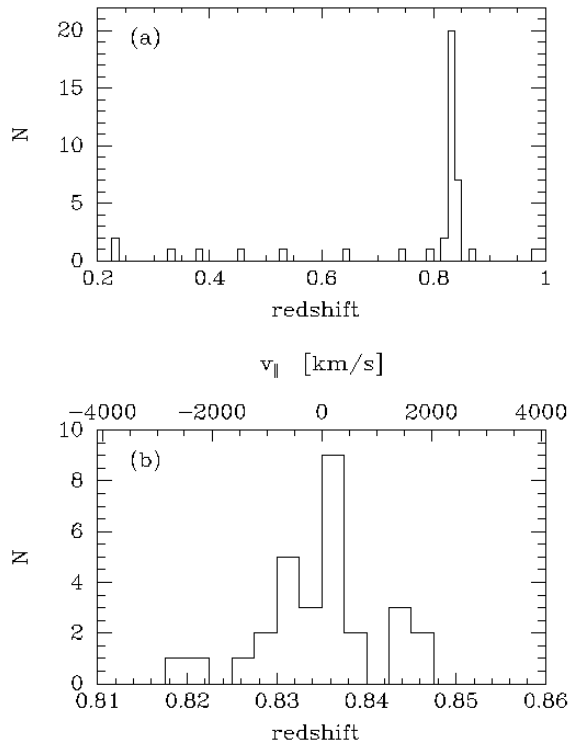


FIG. 5.— Redshift distribution of the spectroscopic sample. (a) The full sample. (b) The cluster members. The top axis on panel (b) gives the radial velocity relative to the cluster redshift and in the rest frame of the cluster, $v_{||} = c(z - z_{\text{cluster}})/(1 + z_{\text{cluster}})$.

stellar populations of the galaxies in RXJ0152.7–1357 and those in our low redshift sample cannot solely be explained by an age difference equal to the lookback time.

The main question we attempt to address is if we can find a model for the evolution that makes the stellar populations of the galaxies in RXJ0152.7–1357 evolve into stellar populations similar to those in our low redshift comparison sample, within the available time which is about 7 Gyr.

7. CLUSTER VELOCITY DISPERSION AND POSSIBLE SUB-STRUCTURE

In this section we establish the criteria for a given galaxy being a cluster member. We also briefly review the evidence showing that RXJ0152.7–1357 is in the process of merging from two sub-clumps. In Section 9, we use this information in the discussion of the stellar populations of the galaxies.

Figure 5 shows the redshift distribution of the spectroscopic sample. In order to derive the median cluster redshift and the line-of-sight cluster velocity dispersion we first exclude galaxies more than 3000 km/s from the median redshift. We then use the biweight method described by Beers et al. (1990) to derive the cluster redshift and velocity dispersion. The uncertainties are derived using a bootstrap method. We note that none of the conclusions would change if we instead had used the methods described by Danese et al. (1980). We find a cluster redshift of $z_{\text{cluster}} = 0.8350 \pm 0.0012$, and a line-of-sight cluster velocity dispersion, $\sigma_{\text{cluster}} = (1110 \pm 163) \text{ km s}^{-1}$. We consider all galaxies within $\pm 3\sigma_{\text{cluster}}$ of the cluster redshift to be cluster members. Of the 41 observed galaxies, 29 are cluster members. Table A12 in the Appendix lists which galaxies are considered cluster members.

Figure 1 shows the *XMM-Newton* data overlaid on our i' -

band image, with the cluster members labeled. The X-ray data for RXJ0152.7–1357 indicates that the cluster is still in the process of merging from the two sub-clumps that can be seen in the main X-ray structure (Maughan et al. 2003). The weak lensing analysis presented by Jee et al. (2004) also supports that RXJ0152.7–1357 is an on-going merger.

The three strong X-ray point sources seen on Figure 1 have obvious optical counterparts, all of which are extended. Table 6 summarizes the positions and ground based photometry for these three optical sources. Two of the sources (ID 1056 and 1397) are included on the HST/ACS imaging of the cluster, which shows that the sources are galaxies with well-defined spiral arms. The galaxies were not included in our spectroscopic sample. However, Ford et al. (2004) have obtained spectroscopy of ID 1056 and 1397, and find that these are Seyfert galaxies and members of the cluster. It is not known if the third source ID 1824 is a member of the cluster. Maughan et al. comment on a fourth X-ray point source. This source is located at $(\text{RA}_{J2000}, \text{DEC}_{J2000}) = (1^{\text{h}}52^{\text{m}}41^{\text{s}}.4, -13^{\circ}59'20''.1)$. We do not find any optical counterpart for this source.

From the *XMM-Newton* data we estimate that the flux in the three point sources is about 20 per cent of the total X-ray flux within the central $3.7 \text{ arcmin} \times 3.7 \text{ arcmin}$ (corresponding to $1.7 \text{ Mpc} \times 1.7 \text{ Mpc}$). If we correct the total X-ray luminosity of RXJ0152.7–1357 for these point sources then the resulting luminosity is about 1.4 times that of the Coma cluster. The cluster velocity dispersion is only slightly larger than that of the Coma cluster. The Coma cluster has a line-of-sight velocity dispersion of $\sigma_{\text{cluster}} = 1010^{+51}_{-44} \text{ km s}^{-1}$ (Zabludoff et al. 1990). Mahdavi & Geller (2001) established the $L_X - \sigma$ relation for rich clusters as $L_X \propto \sigma^{4.4}$, with a scatter of 0.182 dex in L_X . Thus, if the Coma cluster is on the $L_X - \sigma$ relation (no zero point for the relation is given by Mahdavi & Geller), then RXJ0152.7–1357 is within 0.05 dex in L_X of the relation, and therefore consistent with the relation. We also note that Maughan et al. find excess X-ray emission between the two sub-clusters, but at a very low level. The X-ray luminosity of RXJ0152.7–1357 is high enough that it would have been well above our lower sample limit even without the contribution from the three X-ray point sources and the excess X-ray emission between the two sub-clusters.

Two of the galaxies in our sample, ID 1682 and 1614, are associated with the diffuse X-ray emission to the east of the cluster. The mean redshift for these two galaxies is 0.8448, confirming the result from Maughan et al. that galaxies in this group have a higher redshift than that of the main cluster.

Maughan et al. find that the galaxies associated with the two X-ray sub-clumps have slightly different mean redshifts. We find $z = 0.8372 \pm 0.0014$ for the northern sub-cluster (7 galaxies, ID 643, 737, 766, 813, 908, 1027 and 1085), and $z = 0.8349 \pm 0.0020$ for the southern sub-cluster (6 galaxies, ID 1385, 1458, 1567, 1590, 1811, and 1920). This is a somewhat smaller difference than found Maughan et al., and barely significant. We note that both of these sub-clusters of galaxies may have a lower line-of-sight velocity dispersion than that of the full sample, though of course the uncertainties are large for these small numbers of galaxies. We find $\sigma_{\text{northern}} = (681 \pm 232) \text{ km s}^{-1}$ and $\sigma_{\text{southern}} = (866 \pm 266) \text{ km s}^{-1}$. However, we cannot detect any difference between the velocity distribution of all the cluster members and a Gaussian distribution. A Kolmogorov-Smirnov test shows that the probability that the velocity distribution is drawn from a Gaussian distribution is larger than 60 per cent. This is not surprising since we find only a very small difference between the mean

TABLE 6
OPTICAL DATA FOR X-RAY POINT SOURCES

ID	RA (J2000)	DEC (J2000) ^a	r'_{total}	i'_{total}	z'_{total}	$(r' - i)$	$(i' - z')$	FWHM ^b	class ^c
1056	1 52 39.78	-13 57 41.4	21.55	20.53	19.77	0.906	0.746	1.60	0.03
1397	1 52 43.75	-13 59 01.8	20.83	20.58	19.99	0.077	0.519	1.21	0.41
1824	1 52 34.66	-13 59 30.3	20.82	20.12	19.48	0.489	0.654	1.38	0.03

NOTE. — Units of right ascension are hours, minutes, and seconds, and units of declination are degrees, arcminutes, and arcseconds.

^aPositions are consistent with USNO, with an rms scatter of ≈ 0.7 arcsec.

^bThe FWHM of the object in units of the FWHM of a nearby point source in the i -band image from GMOS-N.

^cSExtractor *class_star* from the i' -band image.

TABLE 7
SCALING RELATIONS

Relation	Low redshift sample			RXJ0152.7–1357			$\Delta\gamma$	σ_{sys}	min.coord.
(1)	γ (2)	N_{gal} (3)	rms (4)	γ (5)	N_{gal} (6)	rms (7)	(8)	(9)	(10)
$M_B = (-8.02 \pm 1.08) \log \sigma + \gamma$	-2.29	116	0.81	-3.16	26	0.85	-0.87 ± 0.18	0.21	perpendicular ^d
$H\delta_A + H\gamma_A = -9.1 \log \sigma + \gamma$	13.16	65	1.53	16.64 ^c	21	1.71	3.48 ± 0.42	0.24	... ^b
$H\delta_A + H\gamma_A = (-7.0 \pm 1.3) \log \sigma + \gamma$	8.39	65	1.47	11.88 ^c	21	1.57	3.49 ± 0.39	0.18	$H\delta_A + H\gamma_A$ ^d
$H\delta_A + H\gamma_A = (-5.3 \pm 2.3) \text{D4000} + \gamma$	3.58	65	1.50	7.08	22	1.44	3.50 ± 0.36	...	$H\delta_A + H\gamma_A$ ^e
$\text{D4000} = \gamma$	2.10	65	0.16	2.05 ^f	22	0.16	-0.05 ± 0.04
$\text{CN3883} = (0.29 \pm 0.04) \log \sigma + \gamma$	-0.411	65	0.051	-0.400 ^c	20	0.046	0.011 ± 0.012	0.008	perpendicular
$\log \text{CaHK} = (0.14 \pm 0.04) \log \sigma + \gamma$	0.997	65	0.048	1.019 ^c	21	0.057	0.022 ± 0.014	0.004	perpendicular
$\text{CN}_2 = (0.22 \pm 0.06) \log \sigma + \gamma$	-0.390	65	0.034	-0.416 ^c	21	0.049	-0.026 ± 0.011	0.006	perpendicular ^d
$\log \text{G4300} = (0.14 \pm 0.08) \log \sigma + \gamma$	0.403	65	0.051	0.303 ^c	21	0.11	-0.100 ± 0.025	0.004	perpendicular ^d
$\log \text{Fe4383} = (0.19 \pm 0.09) \log \sigma + \gamma$	0.263	65	0.063	0.037 ^c	20	0.33	-0.226 ± 0.074	0.005	perpendicular ^d
$\log \text{C4668} = (0.33 \pm 0.08) \log \sigma + \gamma$	0.107	65	0.058	0.063 ^c	20	0.136	-0.044 ± 0.031	0.009	perpendicular ^d

NOTE. — (1) Scaling relation. (2) Zero point for the low redshift sample. (3) Number of galaxies included from the low redshift sample. (4) rms in the Y-direction of the scaling relation for the low redshift sample. (5) Zero point for the RXJ0152.7–1357 sample. (6) Number of galaxies included from the RXJ0152.7–1357 sample. (7) rms in the Y-direction of the scaling relation for the RXJ0152.7–1357 sample. (8) Zero point differences derived as “RXJ0152.7–1357”–“low redshift”. (9) Systematic uncertainties on $\Delta\gamma$, derived as 0.026 times the coefficient for $\log \sigma$. (10) Coordinate for the minimization when fitting the scaling relation. “Perpendicular” means the residuals are minimized perpendicular to the relation.

^aGalaxies with $\log \sigma < 1.8$ excluded, emission line galaxies included.

^bSlope adopted from Kelson et al. (2001).

^cEmission line galaxies and galaxies with $\log \sigma < 1.8$ excluded.

^dSlope derived from fit to low redshift sample only

^eSlope derived from fit to RXJ0152.7–1357 sample only, emission line galaxies excluded

^fEmission line galaxies excluded.

redshifts of the two sub-clusters. If sub-clustering can be detected from redshift data only, our sample is most likely too small to do so.

8. STELLAR POPULATIONS AT $Z = 0.83$

In this section we characterize the stellar populations in the RXJ0152.7–1357 galaxies by using (1) scaling relations, (2) comparisons with model grids for line indices, and (3) emission line strengths. The models and their limitations were described in Section 6.

8.1. Scaling relations

Table 7 summarizes the scaling relations that we discuss in the following sections. The scaling relations were fit by minimizing the sum of the absolute residuals. The zero points are derived as the median of the measurements. Except for relations involving $H\delta_A + H\gamma_A$, the relations were fit by minimizing the residuals perpendicular to the relation. For $H\delta_A + H\gamma_A$ we determine the fit by minimizing the residuals

in $H\delta_A + H\gamma_A$. We use minimization of the sum of the absolute residuals and median zero points because this technique is very robust to the effect of outliers. The uncertainties of slopes were derived with a boot-strap method.

Zero point differences between the RXJ0152.7–1357 sample and the low redshift sample are also listed in Table 7. In all cases the differences are derived as “RXJ0152.7–1357”–“low redshift”. The random uncertainties on the zero point differences, $\Delta\gamma$, are derived as

$$\sigma_{\Delta\gamma} = \left(\text{rms}_{\text{low } z}^2 / N_{\text{low } z} + \text{rms}_{\text{RXJ0152}}^2 / N_{\text{RXJ0152}} \right)^{0.5} \quad (1)$$

where subscripts “low z ” and “RXJ0152” refer to the low redshift sample and the RXJ0152.7–1357 sample, respectively. The systematic uncertainties on the zero point differences are expected to be dominated by the possible inconsistency in the calibration of the velocity dispersions, 0.026 in $\log \sigma$ (cf. Section 5). For each scaling relation, we estimate the systematic uncertainty in the zero point difference as 0.026 times the coefficient for $\log \sigma$, see Table 7.

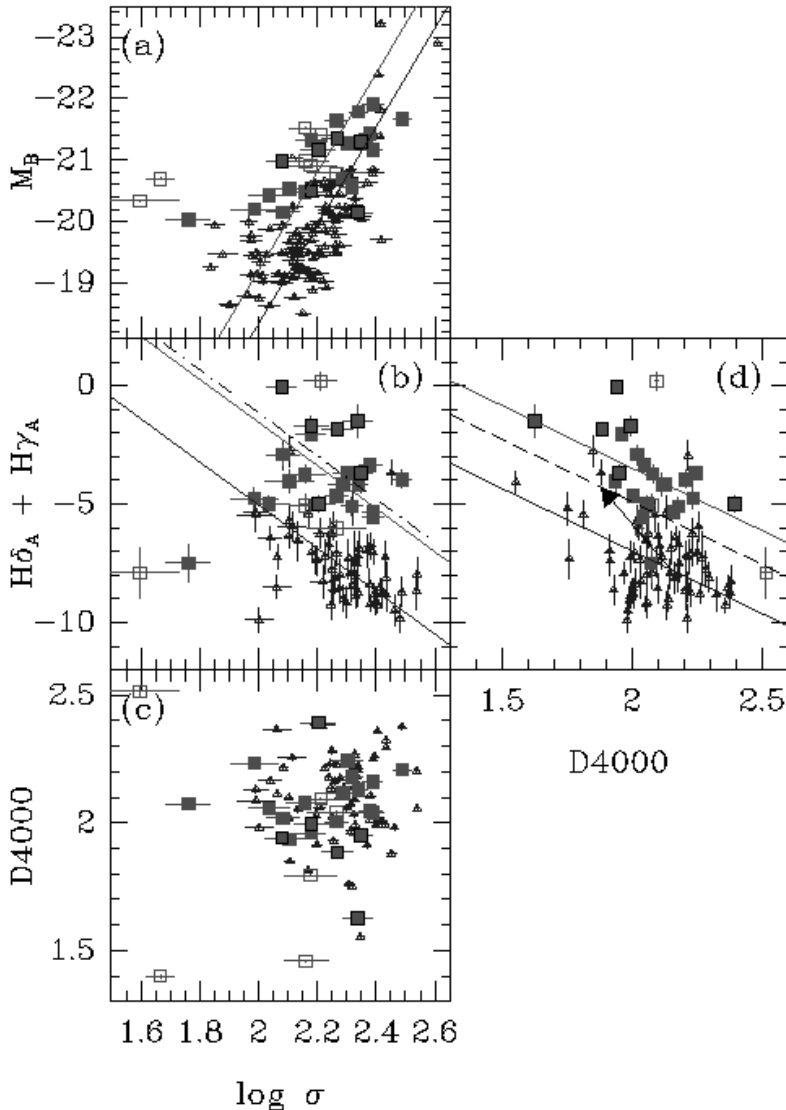


FIG. 6.— The absolute B-band magnitudes M_B , the Balmer line strengths $H\delta_A + H\gamma_A$, and the D4000 index shown as a function of the velocity dispersions. The Balmer line strengths are also shown as a function of the D4000 index. Small blue (black) triangles – low redshift sample; red (grey) filled squares – galaxies in RXJ0152.7–1357 without emission lines; red (grey) open squares – emission line galaxies in RXJ0152.7–1357. The galaxies with low C4668 and G4300 indices discussed in Section 9, are marked with black boxes around the points. Blue (black) solid lines – relations for the low redshift sample; red (grey) solid lines – relations for the RXJ0152.7–1357 sample. The dot-dashed line on panel (b) is the relation from Kelson et al. (2001) for the cluster MS1054-03 at redshift 0.83. The arrow and the dashed line on panel (d) show how the relation for the low redshift sample would be translated in both parameters under assumption of passive evolution and a formation redshift of $z_{\text{form}} = 4.1$, see text for details.

In Sections 8.1.1 and 8.1.2, we discuss the scaling relations for the age indicators and the metal indices, respectively. The relations are shown on Figures 6 and 7.

8.1.1. Scaling relations for the age indicators

The parameters most sensitive to age differences in the stellar populations are the absolute rest frame B-band magnitudes, M_B , and the strengths of the higher order Balmer lines, $H\delta_A + H\gamma_A$. Because the strength of the 4000Å break, D4000, in general is also used to estimate the ages of stellar populations we include this index in the discussion of age indicators. We use the scaling relations of these parameters to test if the data for RXJ0152.7–1357 are consistent with the hypothesis of pure passive evolution.

Figure 6 shows the scaling relations for the age indicators. The total magnitude M_B versus the velocity dispersion is the

Faber-Jackson (1976) relation, which is a projection of the FP. The zero point difference between the RXJ0152.7–1357 sample and the low redshift comparison sample is $\Delta M_B = -0.87 \pm 0.18$, see Table 7. The uncertainty includes only the random uncertainties. The systematic uncertainty is estimated to be 0.21 based on the possible systematic uncertainties affecting the measurements of the velocity dispersions. Adopting a slope of -9.1 or -6.94 instead of -8.02 does not change the zero point difference significantly. We find -0.89 ± 0.20 and -0.92 ± 0.15 in the two cases, respectively (the uncertainties are the random uncertainties). The values -9.1 and -6.94 are the best fitting slope minus and plus, respectively, the 1σ uncertainty on the slope. Thus, the accurate slope is not critical for the derived zero point. Further, we have tested whether the distribution of the velocity dispersions for the RXJ0152.7–1357 sample is significantly different from that

of the low redshift sample. A Kolmogorov-Smirnov test gives a probability of 24 per cent that the two samples are drawn from the same parent sample. Thus, the two samples are not significantly different. In summary, the zero point difference between the RXJ0152.7–1357 sample and the low redshift comparison sample is $\Delta M_B = -0.87 \pm 0.39$ including the systematic uncertainties.

For $H\delta_A + H\gamma_A$ versus $\log \sigma$, we adopt the slope of -9.1 from Kelson et al. (2001). The relation from Kelson et al. is shown on Figure 6b with the zero point that these authors find for the cluster MS1054-03 at redshift 0.83. Our data are in agreement with the data from Kelson et al. at redshift 0.83. With the slope from Kelson et al., we find $\Delta(H\delta_A + H\gamma_A) = 3.48 \pm 0.42$ (random uncertainty). The adopted slope is not critical for the determination of the zero point difference. The zero point difference does not change significantly if we instead use the slope derived from fitting our low redshift sample and the RXJ0152.7–1357 sample, cf. Table 7. The systematic uncertainty on the zero point difference is ≈ 0.2 , see Table 7.

Using models from Maraston for the luminosities and models from Thomas et al. (2004) for the Balmer lines, we can translate these zero point differences to differences in the logarithm of the age in Gyr under the assumption that $[M/H]$ and $[\alpha/Fe]$ do not change, i.e., pure passive evolution. For both parameters, we find $\Delta \log \text{age} = -0.37$. Including the systematic errors, the uncertainties are ± 0.17 and ± 0.065 on the measurement based on M_B and on $H\delta_A + H\gamma_A$, respectively. Thus, $H\delta_A + H\gamma_A$ provide the tightest constraint. For the assumed cosmology, the look-back times at redshifts 0.02 and 0.83 are 0.3 Gyr and 7.0 Gyr, respectively. From the offset in $H\delta_A + H\gamma_A$ we derive the mean ages of the galaxies in RXJ0152.7–1357 must be $5.0^{+1.5}_{-1.0}$ Gyr, and therefore that the lookback time to the epoch of formation must be $12.0^{+1.5}_{-1.0}$ Gyr. This gives a formation redshift $z_{\text{form}} = 4.1$, with a lower limit of 2.7 (one sigma uncertainty). The 95 per cent confidence limit is $z_{\text{form}} > 1.9$. This is consistent with previous results based on either luminosity offsets (e.g., Jørgensen et al. 1999; Kelson et al. 2000; Ziegler et al. 2001) or Balmer line strengths (Kelson et al. 2001). Specifically, based on $H\delta_A + H\gamma_A$ measurements of galaxies in four clusters, Kelson et al. (2001) find 95 per cent confidence limits on z_{form} that are very similar to our result.

Next we examine if the D4000 indices are consistent with pure passive evolution and $z_{\text{form}} = 4.1$. For passive evolution D4000 gets stronger with the age of the stellar population, cf. Table 5, see also Barbaro & Poggianti (1997) for a more detailed discussion of how the D4000 index depends on current and past star formation rates.

Figure 6c and d show the D4000 index versus the velocity dispersion, and $H\delta_A + H\gamma_A$ versus D4000. D4000 does not correlate with the velocity dispersion. A Kendall's τ correlation test (suitable for the small RXJ0152.7–1357 sample as well as the larger low redshift sample) gives a probability of 60 per cent or larger that there is no correlation between the two parameters. Further, the distribution of the D4000 measurements for the low redshift sample and for the RXJ0152.7–1357 are not significantly different. A Kolmogorov-Smirnov test shows that there is a probability of about 60 per cent that two samples are drawn from the same parent distribution. In Table 7 we list the median values and rms scatter for the two samples. There is no significant difference in the median values of D4000, we find $\Delta D4000 = -0.05 \pm 0.04$.

Pure passive evolution with $z_{\text{form}} = 4.1$ predicts an offset in D4000 of -0.28 , the index is expected to be weaker in the RXJ0152.7–1357 galaxies. On Figure 6d we illustrate this offset as the translation of the low redshift relation between D4000 and $H\delta_A + H\gamma_A$ that is predicted by passive evolution with $z_{\text{form}} = 4.1$.

8.1.2. Scaling relations for the metal indices

Figure 7 shows the indices for the metal lines, C4668, CN3883, Fe4383, CaHK, CN₂, and G4300 versus the velocity dispersions. Table 7 summarizes the relations shown on the figure, the zero point differences, as well as the information about how the fitting was done.

All the metal indices depend on both the metallicity and the age of the stellar population. Thus, the scaling relations for the metal indices are expected to evolve for a pure passive evolution model. Under the assumption that there is an age difference of $\Delta \log \text{age} = -0.37$ between the RXJ0152.7–1357 sample and the low redshift sample, as derived from the B magnitudes and the higher order Balmer lines, we can derive the predicted offsets in the metal indices using the relations given in Table 5. We assume that the velocity dispersions do not evolve, and then use these offset to predict the location of the relations for the RXJ0152.7–1357 sample by shifting the relations for the low redshift sample. The predicted relations are shown on Figure 7. These predicted relations can be seen as the predictions for the pure passive evolution model with $z_{\text{form}} = 4.1$. For C4668, CN₂, G4300, and Fe4383, the predictions are based on models from Thomas et al. (2003). For CN3883 and CaHK, the predictions are based on the Bruzual & Charlot (2003) models.

Formally, the zero point differences for CN₂, G4300, and Fe4383 are in marginal disagreement with the pure passive evolution model. If the stellar populations in both samples are very metal rich, the offset predicted for pure passive evolution would be larger than shown for CN₂ on Figure 7e due to the non-linear dependency on the age discussed in Section 6.1. This does not significantly affect the conclusions we draw based on the data. The differences between the model predictions and the data for CN3883 and CaHK are significant at the 5.4σ and 3.5σ level, respectively.

For C4668, G4300 and Fe4383 the scatter of the RXJ0152.7–1357 sample relative to the adopted relations is more than twice the scatter of the low redshift sample. The increased scatter is unlikely to be due to higher measurements uncertainties; in fact the measurement uncertainties for the RXJ0152.7–1357 sample are in general lower than those for the low redshift sample, see Figure 7. For CN₂ the scatter of the RXJ0152.7–1357 sample is about 1.6 times that of the low redshift sample, while for CN3883 and CaHK the scatter for the two samples is very similar. The higher scatter of the RXJ0152.7–1357 sample is not an effect of more blue (star-forming) galaxies being included in that sample compared to the low redshift sample. Except for the two blue emission-line galaxies in the RXJ0152.7–1357 sample, all the galaxies in that sample are on the red sequence of the color-magnitude diagram, as is the case for the low redshift sample. The emission line galaxies in the RXJ0152.7–1357 sample are excluded from the determination of the scatter for all the relations.

8.2. Evidence for differences in metallicities and abundance ratios

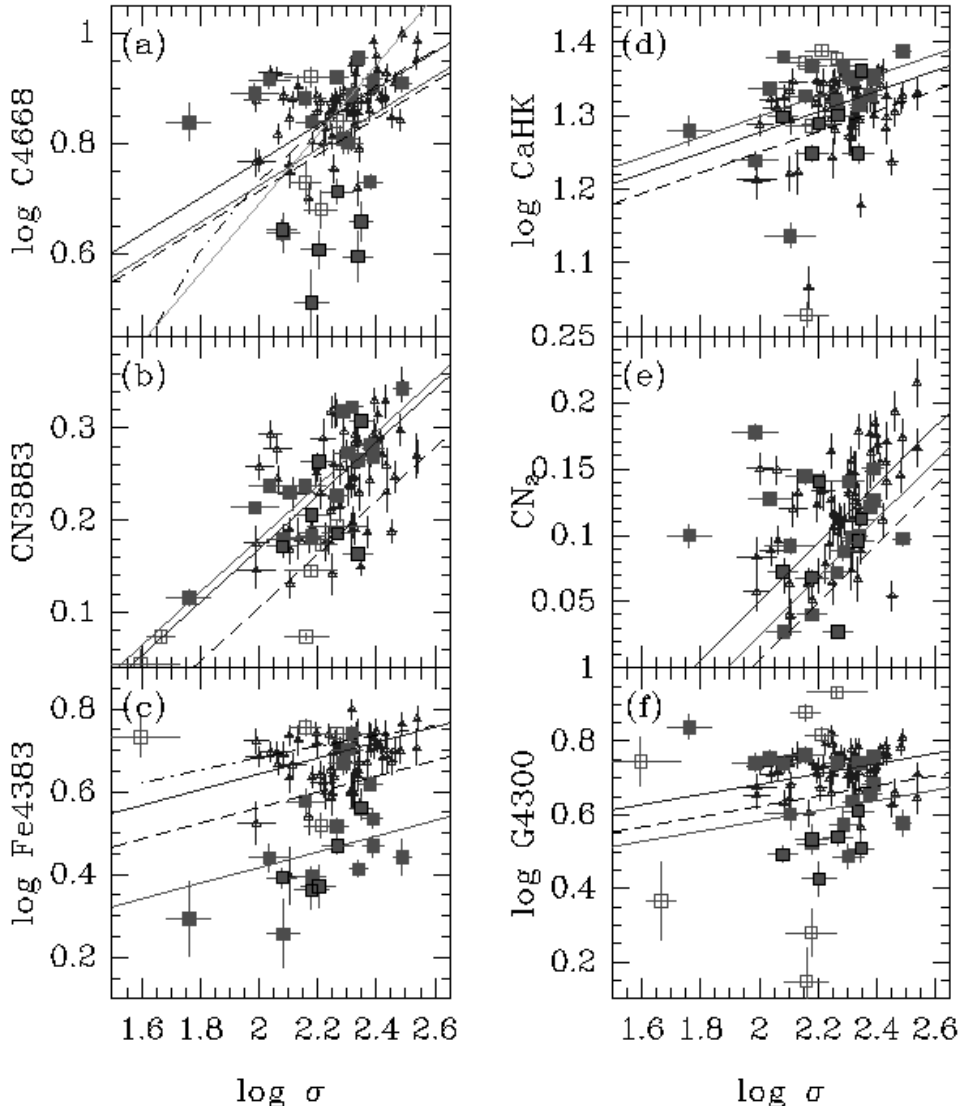


FIG. 7.— Scaling relations for the metal indices. Symbols as in Figure 6. The emission line galaxies in RXJ0152.7–1357 are not shown on panel (e) because none of the CN_2 measurements for these galaxies are reliable. Blue (black) solid lines – relations for the low redshift sample; red (grey) solid lines – relations for the RXJ0152.7–1357 galaxies. Green (grey steep) line – relation for C4668 from Jørgensen (1997) for low redshift galaxies. Dot-dashed lines – relations from Kuschner (2000) for galaxies in the Fornax cluster. Dashed lines – passive evolution predictions for $z_{\text{form}} = 4.1$, see text.

Using the line indices together, and comparing these to the SSP models offer the possibility of disentangling differences in ages from differences in metallicities and abundance ratios. As described in Section 6.2, we use the models only to quantify relative differences between the RXJ0152.7–1357 sample and the low redshift comparison sample, rather than actually derive luminosity weighted mean ages, $[M/H]$, and $[\alpha/\text{Fe}]$ for the individual galaxies.

Figure 8 shows what we call the primary indices C4668 (and CN_2), Fe4383, D4000, and $\text{H}\delta_{\text{A}} + \text{H}\gamma_{\text{A}}$ versus each other. Model grids from Thomas et al. (2003, 2004) are overlaid. D4000 is not included in these models.

The location of the RXJ0152.7–1357 data points on Figures 8c, f, and h cannot be an effect of age differences, only, between the RXJ0152.7–1357 sample and the low redshift sample. We estimate based on these figures that at least half the galaxies in the RXJ0152.7–1357 sample have $[\alpha/\text{Fe}]$ approximately 0.2 dex higher than the low redshift sample. Except for a few of the RXJ0152.7–1357 galaxies, they could in fact

all have $[\alpha/\text{Fe}]$ of 0.2 dex higher than the low redshift sample. Figure 8d indicates that the effect may be even stronger, with many of the RXJ0152.7–1357 galaxies having unusually weak Fe4383 indices. The location of the RXJ0152.7–1357 data points on Figures 8a and c, further indicates that about half of the galaxies have metal content significantly below that of the low redshift sample. This conclusion is based primarily on the C4668 measurements, but is supported by the CN_2 measurements, see Figures 8f and h.

While we have no models for D4000 that include $[\alpha/\text{Fe}]$, it is striking that D4000 is strongly correlated with CN_2 , and that the correlation is the same for the low redshift sample and for the RXJ0152.7–1357 sample. CN_2 increases with increasing $[\alpha/\text{Fe}]$ though the dependence is relatively weak, see Table 5. The correlation between D4000 and CN_2 may indicate that D4000 also increases with increasing $[\alpha/\text{Fe}]$. We return to this issue in Section 9.

Figure 9 shows C4668, Fe4383, D4000, and $\text{H}\delta_{\text{A}} + \text{H}\gamma_{\text{A}}$ versus what we call the secondary indices, G4300, CN3883, and

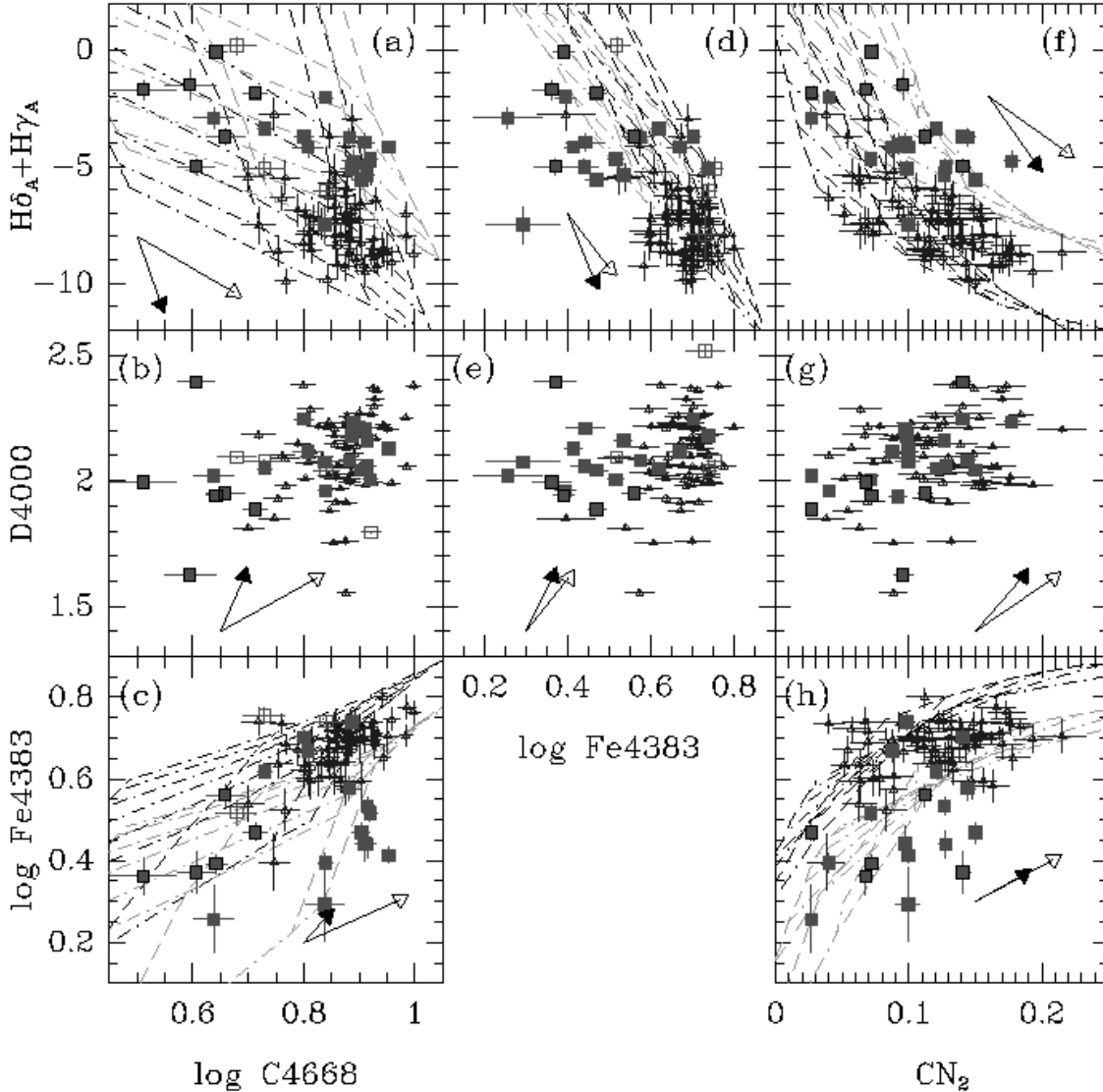


FIG. 8.— The primary blue line indices versus each other. Data symbols as in Figure 6. The grids on panels (a), (c), and (d) are SSP models from Thomas et al. (2003, 2004). The black grid and green (grey) grid have $[\alpha/\text{Fe}] = 0.2$ and 0.5 , respectively. Dashed lines – lines of constant $[\text{M}/\text{H}]$, for values of $-0.33, 0.0, 0.35$ and 0.67 . Dot-dashed lines – lines of constant ages, for values of $1, 2, 3, 5, 8, 11,$ and 15 Gyr. The arrows show the approximate changes in the indices for a change of $\Delta \log \text{age} = 0.3$ (solid arrow) and $\Delta [\text{M}/\text{H}] = 0.3$ (open arrow).

CaHK. Model grids from Thomas et al. (2003, 2004) are overlaid for G4300. D4000, CN3883 and CaHK are not included in the models. We use these plots to check whether the secondary indices give results that are consistent with the primary indices, and we discuss if there are better choices of metal indices than the primary indices.

Figure 9d (G4300 versus C4668) supports the lower metal content of part of the RXJ0152.7–1357 sample compared to the low redshift sample. The plots of G4300 versus $\text{H}\delta_{\text{A}} + \text{H}\gamma_{\text{A}}$ and Fe4383 (Figure 9a and c) indicate that about a third of the galaxies in the RXJ0152.7–1357 sample have $[\alpha/\text{Fe}]$ roughly 0.2 dex higher than the low redshift sample. However, closer inspection of these plots and comparison with Figure 8f and h reveals that the high $[\alpha/\text{Fe}]$ galaxies are not the same galaxies on the two sets of plots. This can be seen by looking at the location of the six weak-lined galaxies (discussed in Section 9), which are marked with black boxes around the points. This inconsistency may be due to the modeling of G4300. Thomas et al. (2003) comment that this index is very poorly

calibrated. Even though the models for different $[\alpha/\text{Fe}]$ are well-separated in G4300 versus Fe4383 (Figure 9c), we therefore conclude that G4300 with the present modeling is not a convincing blue alternative to Mgb .

The remainder of the indices shown on Figure 9 have not been modeled by Thomas et al. However, D4000 and CN3883 show a similar strong correlation as seen for D4000 and CN_2 , and the correlation is the same for the RXJ0152.7–1357 sample and the low redshift sample.

Fe4383 versus CN3883 (Figure 9g) as well as $\text{H}\delta_{\text{A}} + \text{H}\gamma_{\text{A}}$ versus CN3883 (Figure 9e) show a clear separation of the two samples, similar to separation seen when using CN_2 instead of CN3883. If we assume that Fe4383 primarily probes the iron abundance, while CN3883 probes the carbon and nitrogen abundance, then the distribution of data points on Figure 9g indicates that the low metallicity galaxies in RXJ0152.7–1357 have significantly higher $[\text{CN}/\text{Fe}]$ than seen in the low redshift sample.

The index CN3883 is stronger than CN_2 , in the sense that

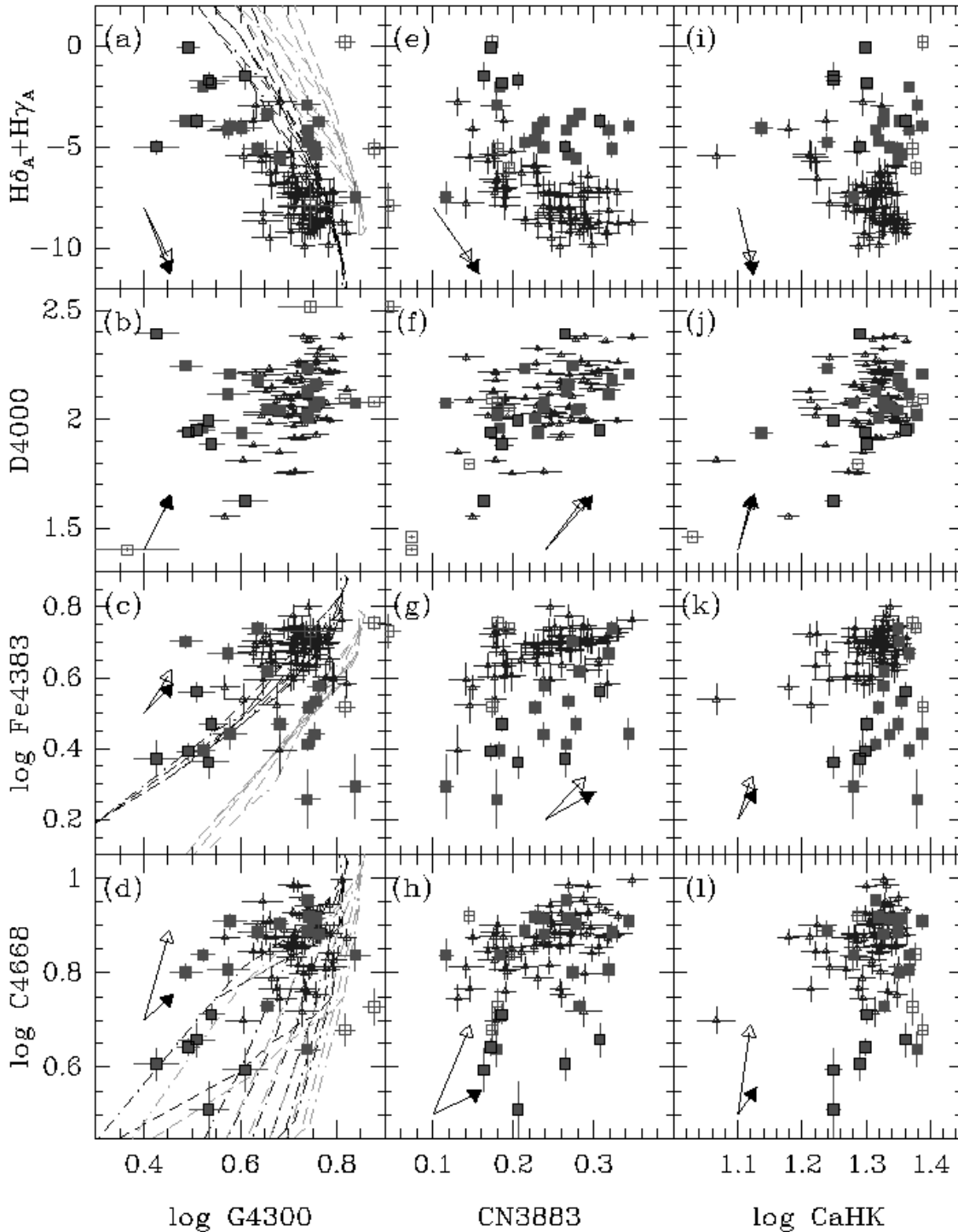


FIG. 9.— The primary blue line indices $C4668$, $Fe4383$, $D4000$, and $H\delta_A + H\gamma_A$ versus the secondary indices $G4300$, $CN3883$, and $CaHK$. Data symbols as in Figure 6. The grids on panels (a), (c), and (d) are SSP models from Thomas et al. (2003, 2004). The same models are shown in these panels as those included on Figure 8. The arrows show the approximate changes in the indices for a change of $\Delta \log \text{age} = 0.3$ (solid arrow) and $\Delta [M/H] = 0.3$ (open arrow).

for a given S/N of the spectra the relative uncertainties on $CN3883$ is smaller than that of CN_2 . Further, for galaxies in RXJ0152.7–1357 and in general for galaxies for which the blue continuum passband is redshifted to wavelengths redwards of 4000\AA the $CN3883$ index is also very easy to measure. Thus, this index is potentially very useful for studies of galaxies at redshifts above about 0.1. It would be valuable to have the dependence of $[\alpha/Fe]$ and $[CN/Fe]$ modeled for

$CN3883$.

The $CaHK$ index adds very little information. The separation of the low redshift sample and the RXJ0152.7–1357 sample on Figure 9i, k, and l is due to the indices plotted versus $CaHK$, and is not caused by $CaHK$ itself.

8.3. Recent star formation – the emission line galaxies

There are seven galaxies in the RXJ0152.7–1357 sample that have significant emission lines. Five of these follow the red sequence in color-magnitude diagram, Figure 2, though one of them (ID 1920) has a quite low S/N spectrum. The main questions of interest are the mass fraction involved in the star formation and the duration of the star formation episode.

In order to convert the equivalent width of the [O II] to star formation rates we assume that the equivalent width measured within the aperture we use is representative of the global value. We then derive the observed luminosity of the [O II] line as

$$L([\text{OII}]_{\text{obs}}) = 1.4 \cdot 10^{29} \frac{L_{\text{B}}}{L_{\text{B}\odot}} \text{EW}([\text{OII}]) (\text{ergs s}^{-1}) \quad (2)$$

with $\frac{L_{\text{B}}}{L_{\text{B}\odot}} = 10^{0.4(5.48 - M_{\text{B}})}$, see Kennicutt (1992) and Balogh et al. (1997). We convert the observed $L([\text{OII}]_{\text{obs}})$ to the star formation rate (SFR) in $M_{\odot} \text{ yr}^{-1}$ using the calibration from Kewley et al. (2004)

$$\text{SFR} = 6.58 \cdot 10^{-42} L([\text{OII}]) \quad (3)$$

with

$$L([\text{OII}]) = 3.11 \cdot 10^{-20} L([\text{OII}]_{\text{obs}})^{1.495} \quad (4)$$

Equation 4 takes into account the intrinsic reddening. Since we do not know the oxygen abundances, we have chosen to use the average calibration established by Kewley et al.

We find that the mean SFR for the four red emission line galaxies is $1.3 M_{\odot} \text{ yr}^{-1}$. If we estimate the mean mass of these four galaxies based on their absolute B magnitude, the median luminosity difference between the RXJ0152.7–1357 sample and the low redshift sample, and the FP for the low redshift sample, we get a mean mass of about $1.5 \cdot 10^{11} M_{\odot}$. Thus, a 1 Gyr burst of star formation with the mean SFR found from the [O II] line would have involved about 1 per cent of the mass.

We attempted to further constrain the mass fraction and duration of the star formation episode by creating “toy” models, which consist of a mix of two stellar populations. We assumed that some mass fraction was involved in the star formation episode, while the remainder of the mass, the underlying “old” stellar population, is not forming stars. We used models from Magris et al. (2003) for the star forming population and models from Bruzual & Charlot (2003) for the “old” stellar populations. However, none of our modeling resulted in further constraints on the duration or the mass involved in the star formation episode. The emission lines are either caused by quite small mass fraction (1 per cent) involved in a very recent star formation burst (less the 0.3 Gyr prior), or if a larger mass fraction is involved the episode must have started earlier.

9. DISCUSSION

Using the results presented in Sections 7 and 8, we now attempt to determine if there is an evolutionary scenario for the galaxies in the RXJ0152.7–1357 sample that will make these galaxies evolve into galaxies similar to those in our low redshift sample, within the available time which is about 7 Gyr.

We assume that the galaxies in the RXJ0152.7–1357 sample can be considered the progenitors for the galaxies in the low redshift sample. There is no guarantee that this assumption is correct. However, we note that all the non-emission galaxies in the RXJ0152.7–1357 sample are on the red sequence. Based on the HST/ACS archive data available for RXJ0152.7–1357 we find that none of these galaxies show any obvious spiral structure, see Figure A18 in the Appendix.

Thus, these galaxies are morphologically similar to the low redshift sample. The four red emission line galaxies are on the red sequence and they show weak spiral structure (see Figure A18). We do not know whether their morphologies will evolve such that they will resemble our low redshift sample after ≈ 7 Gyr, but we can still discuss whether there is an evolutionary scenario for their stellar populations that will lead to stellar populations similar to those of the low redshift sample. The two blue emission line galaxies in the RXJ0152.7–1357 sample are not considered in this discussion.

The simplest evolutionary scenario is pure passive evolution (scenario 1 in Section 6.3). No new stars are formed and the model prediction is that the only difference between the stellar populations in the RXJ0152.7–1357 sample and those in the low redshift sample should be an age difference equal to the difference in the lookback time. In Section 8.1.1 we found that this is in agreement with the B-band luminosities and the strength of the higher order Balmer lines, and that the model implies a formation redshift of $z_{\text{form}} \approx 4$. However, once we take the other spectral indices into account, the picture is no longer this simple. First, the SSP models predict that for a pure passive evolution model we should have found a difference in the D4000 strengths between the RXJ0152.7–1357 sample and the low redshift sample. The difference between the predicted offset in D4000 and the measured (insignificant) offset is larger than five times the uncertainty. Further, both the scatter and the zero point differences for several of the scaling relations for the metal indices are in contradiction with the pure passive evolution model, cf. Table 7.

If pure passive evolution is the correct evolutionary scenario, then either the data or the models (or both) must be incorrect for many of the indices. The SSP models from Thomas et al. (2003, 2004) are ambitious in the sense that they include non-solar $[\alpha/\text{Fe}]$. However, the age dependencies of the various parameters predicted by these models are in general agreement with other models, e.g., the Vazdekis-2000 models. Even if the details of the models are incorrect, we find it very unlikely that the significantly higher scatter in some of the scaling relations for the RXJ0152.7–1357 sample compared to those of the low redshift sample can be due to age differences only. The most troubling is perhaps that the D4000 indices for the RXJ0152.7–1357 sample are very similar to those of the low redshift sample. This index is strong and has low measurement uncertainties. We therefore consider it unlikely that the data are grossly incorrect. Thus, if pure passive evolution is the correct evolutionary scenario, then the models predicting a significant age dependency for D4000 must be incorrect.

Because of the many contradictions between the data and predictions for the pure passive evolution scenario, we consider this evolutionary scenario unlikely. Next we discuss the evidence for differences in metal content $[\text{M}/\text{H}]$ and abundance ratios $[\alpha/\text{Fe}]$ between the RXJ0152.7–1357 sample and the low redshift sample, and use these differences to discuss evolutionary scenarios that involve star formation and/or merging, in addition to passive evolution of the already existing stellar population.

First we examine in more detail the possible cause of the higher scatter for C4668, G4300 and Fe4383 scaling relations found for the RXJ0152.7–1357 sample (see Section 8.1.2 and Table 7). For C4668 and G4300 it appears that there is a group of galaxies roughly following the relations established for the low redshift sample, while another group of galaxies have significantly weaker metal indices, see Figure 7. The

majority of the RXJ0152.7–1357 galaxies has significantly weaker Fe4383 indices than found for the low redshift sample. We isolate the galaxies with C4668, G4300 and Fe4383 weaker than the relations established for the low redshift sample by more than twice the rms of that sample. There are six galaxies that meet that criterion for all three indices, none of them are emission line galaxies. In fact Fe4383 does not limit this sample more than just requiring C4668 and G4300 to be weak. The six galaxies are ID 737, 776, 1507, 1614, 1682 and 1935. Five of these lie, in projection, in areas of the cluster that have low X-ray flux (see Figure 1). Two of them (ID 1614 and 1682) are in the diffuse X-ray emission east of the main X-ray structure. If we exclude C4668 as a selection criteria and then select the group of galaxies with weak G4300 as before, this group then contains 10 non-emission line galaxies. Eight of these are in areas of low X-ray flux. If we on the other hand exclude G4300 as a selection criteria, then there are eight non-emission line galaxies with weak C4668, seven of which are in areas of low X-ray flux. For reference, 14 of the 29 cluster members are located in areas of low X-ray flux. The four red emission line galaxies in the RXJ0152.7–1357 sample, which have good S/N spectra (ID 566, 643, 1159 and 1299), also appear to be located in areas of low X-ray luminosity. Further, Ford et al. (2004) find in their study of this cluster that the star-forming spiral galaxies in the cluster are located in areas of low X-ray luminosity away from the cores of the two sub-clusters.

We speculate that the unusually weak C4668, G4300 (and Fe4383), as well as the weak emission lines in the red emission line galaxies, are the effect of short bursts of star formation in these galaxies, maybe triggered as a result of their first infall into the cluster. Only the galaxies with the weak emission lines still have small amounts of on-going star formation, while in the galaxies without emission lines the star formation has stopped. Using the scaling relation between the higher order Balmer lines $H\delta_A + H\gamma_A$ and the velocity dispersions (Figure 6b) we find that the six weak-lined galaxies are offset with $\Delta(H\delta_A + H\gamma_A) = 2.26 \pm 0.77$ from the rest of the non-emission line galaxies in the RXJ0152.7–1357 sample. A similar offset is not seen in the absolute B magnitudes where the difference is insignificant $\Delta M_B = -0.07 \pm 0.45$. It is therefore possible that these galaxies are offset in $H\delta_A + H\gamma_A$ primarily because of a higher $[\alpha/Fe]$. The offset in $H\delta_A + H\gamma_A$ is equivalent to an offset in $[\alpha/Fe]$ of 0.3 dex, assuming no differences in the mean ages and the mean $[M/H]$ between these six galaxies and the remainder of the RXJ0152.7–1357 galaxies. If these six galaxies do contain younger stellar populations than the remainder of the RXJ0152.7–1357 galaxies this offset in $[\alpha/Fe]$ should be seen as an upper limit.

Based on our comparison of $H\delta_A + H\gamma_A$, Fe4383 and CN_2 with the model grids from Thomas et al. (2003, 2004) (see Figure 8) we found that a large fraction of the galaxies in the RXJ0152.7–1357 sample may have $[\alpha/Fe]$ about 0.2 dex higher than seen in the low redshift sample. If we assume that the median difference in $[\alpha/Fe]$ between the RXJ0152.7–1357 sample and the low redshift sample is 0.2 dex, then this explains about half of the offset in $H\delta_A + H\gamma_A$ between the two samples. This in turn means that the difference required in the mean ages to explain the remainder of the offset is only $\Delta \log \text{age} \approx -0.2$. Formally this leads to a formation redshift higher than found in Section 8.1.1, but the pure passive evolution scenario is of course no longer valid because of the difference in the abundance ratios. We also found that because of the empirical correlation between D4000 and CN_2 that D4000

would have to increase with $[\alpha/Fe]$, if CN_2 increases with $[\alpha/Fe]$ as the models indicate. It is therefore possible that the D4000 indices for the RXJ0152.7–1357 sample can be explained by a combination of younger mean ages (leading to weaker D4000 indices) combined with higher $[\alpha/Fe]$ (leading to stronger D4000 indices), giving the net result that the D4000 indices for the RXJ0152.7–1357 sample are similar to those of the low redshift sample. Until models are available that predict how D4000 depends on $[\alpha/Fe]$, this remains a speculation. Models with non-solar $[\alpha/Fe]$ are also needed for the M/L ratios, since current models cannot be used to test if the differences in both ages and $[\alpha/Fe]$ would lead to inconsistencies with the measured luminosities.

It is difficult (if not impossible) to envision an evolutionary path that within the available time (about 7 Gyr) will lead from the stellar populations in the RXJ0152.7–1357 sample to those in the low redshift sample. The hardest challenge would be to identify processes that would reduce $[\alpha/Fe]$ with 0.2 dex for a large number of the galaxies, without causing the resulting mean ages of the stellar populations in the galaxies to be much too young. One possibility would be mergers between these high $[\alpha/Fe]$ galaxies and galaxies containing stellar populations with much lower $[\alpha/Fe]$, i.e. (disk) galaxies whose stellar populations formed over a much longer time scale. Thus, this may be either scenario (3) or (4) as described in Section 6.3, depending on whether there is star formation involved. In any case, in order to maintain a mix of stellar populations with fairly high mean ages such mergers can involve only a small amount of new star formation. Further, one would need a source of low $[\alpha/Fe]$ galaxies that are dominated by “old” (5 Gyr) stellar populations. Our RXJ0152.7–1357 sample is by no means complete, but it is difficult to envision the presence of a large populations of $[\alpha/Fe] = 0$ galaxies in the cluster – only three out of the 29 galaxies in our sample have line indices in agreement with $[\alpha/Fe] = 0$.

Perhaps an easier task would be to determine how the galaxies in the RXJ0152.7–1357 sample would appear if they were to evolve passively for 7 Gyr, without merging. After 7 Gyr of passive evolution, the red emission line galaxies will no longer have emission lines. Further, since the mass involved in the star formation is around 1 per cent of the total mass, the properties of the galaxies will be dominated by the underlying “old” stellar population. Thus, the signature of the short episode of star formation will no longer be detectable. We can only speculate as to whether these galaxies retain their weak spiral structure. The galaxies in RXJ0152.7–1357 that have higher $[\alpha/Fe]$ than the low redshift sample will still have higher $[\alpha/Fe]$ after 7 Gyr of passive evolution. The galaxies will also still cause the scatter in the scaling relations for C4668, G4300 and Fe4383 to be higher than found for the low redshift sample. Thus, pure passive evolution of the RXJ0152.7–1357 galaxies will result in stellar populations different from those in the low redshift sample.

10. CONCLUSIONS

We have studied the stellar populations in galaxies in the rich galaxy cluster RXJ0152.7–1357 at a redshift of 0.83. Our conclusions are based on high signal-to-noise optical spectroscopy and ground based photometry in three filters. From the spectroscopy we have measured redshifts and central velocity dispersions. Of the 41 galaxies observed, 29 are cluster members. For these, we present absorption line indices for the Lick/IDS lines in the wavelength region from 4000Å to 4700Å in the rest frame. We have also measured the indices

CN3883, CaHK and D4000 located at shorter wavelengths and not part of the Lick/IDS system. For the seven emission line galaxies in our RXJ0152.7–1357 sample, we measure the equivalent width of the [O II] line.

We have established scaling relations between the absolute total B magnitude and the central velocity dispersions of the galaxies (the Faber-Jackson relation) as well as relations between absorption line indices and the central velocity dispersions of the galaxies. Comparison of these relations with those for our low redshift comparison sample shows that the B magnitudes and the strengths of the high order Balmer lines, $H\delta_A + H\gamma_A$, are in agreement with pure passive evolution and a formation redshift $z_{\text{form}} \approx 4$. However, the measurements of D4000 do not support this conclusion. The strengths of the line indices for the metal lines, as well as the scatter in the scaling relations for C4668, Fe4383 and G4300 also indicate that pure passive evolution will not result in the stellar populations of the galaxies in the RXJ0152.7–1357 sample evolving into stellar populations similar to those in our low redshift comparison sample, within the available time.

We find that six galaxies with weak G4300 and C4668 lines for their velocity dispersion, as well as four red galaxies with emission lines appear to be located in areas of low X-ray luminosity. It is likely that these galaxies are experiencing the effect of the merger of the two sub-clusters that make up the RXJ0152.7–1357 cluster as (short) episodes of star formation triggered by the cluster merger.

Comparing the strengths of C4668, Fe4383, CN3883, G4300 and CN_2 to predictions from the stellar population models from Thomas et al. (2003, 2004) we find that at least half of the galaxies in the cluster have an α -element abundance ratio [α /Fe] of 0.2 dex higher than the galaxies in our low redshift comparison sample. This also indicates that the evolution of these galaxies may have involved more short bursts of star formation than has been the case for the low redshift sample. For about half of the non-emission line galaxies in the cluster, the metal content is (still) significantly below that of the low redshift comparison sample.

The study of RXJ0152.7–1357 presented in this paper contains the first published study of metal line indices at this redshift. Previous studies have concentrated on luminosities,

either using the Faber-Jackson relation or the Fundamental Plane, and Balmer lines. Our results are in agreement with these previous studies in the sense that if we had limited our analysis to the Faber-Jackson relation and the Balmer lines we would have concluded that the stellar populations of the galaxies in the RXJ0152.7–1357 sample by pure passive evolution can evolve into stellar populations similar to those seen in our low redshift sample, and stellar populations have a formation redshift $z_{\text{form}} > 2$. Only because we also have measured the indices for the metal lines and D4000, do we find that pure passive evolution no longer appears to be a viable scenario. An evolutionary path that makes the galaxies in the RXJ0152.7–1357 sample evolve into galaxies similar to our low redshift sample has to involve star formation and/or merging.

Acknowledgments: Claudia Maraston is thanked for making M/L ratio information available for her SSP models prior to publication. Karl Gebhardt is thanked for making his kinematics software available. We thank the anonymous referee for constructive suggestions that helped improve this paper. Based on observations obtained at the Gemini Observatory, which is operated by the Association of Universities for Research in Astronomy, Inc., under a cooperative agreement with the NSF on behalf of the Gemini partnership: the National Science Foundation (United States), the Particle Physics and Astronomy Research Council (United Kingdom), the National Research Council (Canada), CONICYT (Chile), the Australian Research Council (Australia), CNPq (Brazil) and CONICET (Argentina). The data presented in this paper originate from the following Gemini programs: GN-2002B-Q-29 (a queue program) and GN-2002B-SV-90 (an engineering program). Observations have been used that were obtained with *XMM-Newton*, an ESA science mission funded by ESA member states and NASA. In part, based on observations made with the NASA/ESA Hubble Space Telescope, obtained from the data archive at the Space Telescope Science Institute. STScI is operated by the Association of Universities for Research in Astronomy, Inc. under NASA contract NAS 5-26555.

REFERENCES

- Aaronson, et al. 1986, ApJ, 302, 536
 Balogh, M. L., Morris, S. L., Yee, H. K. C., Carlberg, R. G., & Ellingson, E. 1997, ApJ, 488, L75
 Barbaro, G., & Poggianti, B. M. 1997 A&A, 324, 490
 Beers, T. C., Flynn, K., & Gebhardt, K. 1990, AJ, 100, 32
 Bender, R., Burstein, D., & Faber, S. M. 1993, ApJ, 411, 153
 Bender, R., et al. 1998, ApJ, 493, 529
 Bertin, E., & Arnouts, S. 1996, A&AS, 117, 393
 Blanton, M. R., et al. 2003, AJ, 125, 2348
 Böhm, A., et al. 2004, A&A, 420, 97
 Bruzual, G., & Charlot, S. 2003, MNRAS, 344, 1000
 Bruzual, G. 1983, ApJ, 273, 105
 Cardelli, J. A., Clayton, G. C., & Mathis, J. S. 1989, ApJ, 345, 245
 Cardiel, N., Gorgas, J., & Aragon-Salamanca, A. 1998, MNRAS, 298, 977
 Carretero, C., Vazdekis, A., Beckman, J. E., Sánchez-Blázquez, P., & Gorgas, J. 2004, ApJ, 609, L45
 Chiappini, C., Romano, D., & Matteucci, F. 2003, MNRAS, 339, 63
 Colless, M., et al. 1999, MNRAS, 303, 813
 Concannon, K. D., Rose, J. A., & Caldwell, N. 2000, ApJ, 536, L19
 Danese, L., De Zotti, G., & di Tullio, G. 1980, A&A, 82, 322
 Davidge, T. J., & Clark, C. C. 1994, AJ, 107, 946
 Davies, R. L., Sadler, E. M., & Peletier, R. F. 1993, MNRAS, 262, 650
 Della Ceca, R., Scaramella, R., Gioia, I. M., Rosati, P., Fiore, F., & Squires, G. 2000, A&A, 353, 498
 Djorgovski, S., & Davis, M. 1987, ApJ, 313, 59
 Dressler, A., et al. 1987, ApJ, 313, 42
 Dressler, A., et al. 1997, ApJ, 490, 577
 Ebeling, H., et al. 2000, ApJ, 534, 133
 Ellis, S. C., & Jones, L. R. 2004, MNRAS, 348, 165
 Faber, S. M., & Jackson, R. E. 1976, ApJ, 204, 668
 Ferreras, I., & Silk, J. 2000a, MNRAS, 316, 786
 Ferreras, I., & Silk, J. 2000b, ApJ, 541, L37
 Ford, H., et al. 2004, to appear in Penetrating Bars through Masks of Cosmic Dust: the Hubble Tuning Fork Strikes a New Note, eds. Block, D.L., Freeman, K.C., Puerari, I. & Groess, R. (astro-ph/0408165)
 Gebhardt, K., et al. 2000, AJ, 119, 1157
 Gebhardt, K., et al. 2003, ApJ, 597, 239
 Girardi, L., Bressan, A., Bertelli, G., & Chiosi, C. 2000, A&AS, 141, 371
 Gorgas, J., Cardiel, N., Pedraz, S., & Gonzales, J. J. 1999, A&AS, 139, 29
 Hook, I. M., Jørgensen, I., Allington-Smith, J. R., Davies, R. L., Metcalfe, N., Murowinski, R. G., & Crampton, D. 2004, PASP, 116, 425
 Jee, M. J., et al. 2004, ApJ, in press (astro-ph/0409304)
 Jones, L. R., et al. 2004, in Clusters of Galaxies: Probes of Cosmological Structure and Galaxy Evolution, Eds. J.S. Mulchaey, A. Dressler, & A. Oemler (Pasadena: Carnegie Observatories), 25
 Jørgensen, I. 1997, MNRAS, 288, 161
 Jørgensen, I. 1999, MNRAS, 306, 607
 Jørgensen, I., Franx, M., & Kjaergaard, P. 1995, MNRAS, 276, 1341
 Jørgensen, I., Franx, M., & Kjaergaard, P. 1996, MNRAS, 280, 167
 Jørgensen, I., Franx, M., Hjorth, J., & van Dokkum, P. G. 1999, MNRAS, 308, 833
 Kauffmann, G., & Charlot, S. 1998, MNRAS, 294, 705
 Kannappan, S. J., & Barton, E. J. 2004, AJ, 127, 2694
 Kelson, D. D., et al. 2000, ApJ, 531, 184
 Kelson, D. D., Illingworth, G. D., Franx, M., & van Dokkum, P. G. 2001, ApJ, 552, L17

- Kennicutt, R. C., Jr. 1992, ApJ, 388, 310
 Kewley, L. J., Geller, M. J., & Jansen, R. A. 2004, AJ, 127, 2002
 Kuntschner, H. 2000, MNRAS, 315, 184
 Landolt, A. U. 1992, AJ, 104, 340
 Magris C., G., Binette, L., & Bruzual, G. 2003, ApJS, 149, 313
 Mahdavi, A., & Geller, M. J. 2001, ApJ, 554, L129
 Maraston, C. 2004, MNRAS, submitted (astro-ph/0410207)
 Maughan, B. J., Jones, L. R., Ebeling, H., Perlman, E., Rosati, P., Frye, C., & Mullis, C. R. 2003, ApJ, 587, 589
 Milvang-Jensen, B., Aragón-Salamanca, A., Hau, G. K. T., Jørgensen, I., & Hjorth, J. 2003, MNRAS, 339, L1
 Nichol, R. C., et al. 1999, ApJ, 521, L21
 Salpeter, E. E. 1955, ApJ, 121, 161
 Sánchez-Blázquez, P., Gorgas, J., Cardiel, N., Cenarro, J., & González, J. J. 2003, ApJ, 590, L91
 Schlegel, D. J., Finkbeiner, D. P., & Davis, M. 1998, ApJ, 500, 525
 Smith, J. A., et al. 2002, AJ, 123, 2121
 Thomas, D., & Maraston, C. 2003, A&A, 401, 429
 Thomas, D., Maraston, C., & Bender, R. 2003, MNRAS, 339, 897
 Thomas, D., Maraston, C., & Korn, A. 2004, MNRAS, 351, L19
 Trager, S. C., Faber, S. M., Worthey, G., & González, J. J. 2000, ApJ, 119, 1645
 Tripicco, M. J., & Bell, R. A. 1995, AJ, 110, 3035
 van Dokkum, P. G., et al. 1998, ApJ, 504, L17
 van Dokkum, P. G., & Franx, M. 2003, ApJ, 553, 90
 van Dokkum, P. G., & Stanford, S. A. 2003, ApJ, 585, 78
 Vazdekis, A., Casuso, E., Peletier, R. F., & Beckman, J. E. 1996, ApJS, 107, 306 (<http://star-www.dur.ac.uk/~vazdekis/models.html>)
 Vazdekis, A., Peletier, R. F., Beckman, J. E., & Casuso, E. 1997, ApJS, 111, 203
 Vogt, N. P., Forbes, D. A., Phillips, A. C., Gronwall, C., Faber, S. M., Illingworth, G. D., & Koo, D. C. 1996, ApJ, 465, L15
 Worthey, G., Faber, S. M., & Gonzalez, J. J. 1992, ApJ 298, 69
 Worthey, G., Faber, S. M., Gonzalez, J. J., & Burstein, D. 1994, ApJS, 94, 687
 Worthey, G., & Ottaviani, D. L. 1997, ApJS, 111, 377
 Wuyts, S., van Dokkum, P. G., Kelson, D. D., Franx, M., & Illingworth, G. D. 2004, ApJ, 605, 677
 Zabludoff, A., Huchra, J. P., & Geller, M. J. 1990, ApJS, 74, 1
 Ziegler, B. L., Bower, R. G., Smail, I., Davies, R. L., & Lee, D. 2001, MNRAS, 325, 1571
 Ziegler, B. L., et al. 2002, ApJ, 564, L69
 Ziegler, B. L., Böhm, A., Jäger, K., Heidt, J., & Möllenhoff, C. 2003, ApJ, 598, L87

APPENDIX

A. REDUCTION OF GMOS DATA

The data were reduced using the Gemini IRAF package. In order to make the description of the reductions useful to a wider audience, we give the names of the tasks in the Gemini IRAF package used for each of the reduction steps. It is also noted when the reduction techniques differ from the techniques implemented in the Gemini IRAF package.

GMOS-N has three detectors placed side by side. The raw images are multi-extension FITS (MEF) images with three image extensions, one for each of the detectors. The data format for GMOS data is described in detail on the Gemini web pages (<http://www.gemini.edu>).

A.1. Imaging data

A.1.1. Basic reduction steps handled by the Gemini IRAF package

Mean bias frames were created from all the available bias frames taken during each of the GMOS-N observing runs (task `gbias`). The overscan level was not subtracted, since it is known that the overscan region on the GMOS-N detectors contain residual signal that depends on the signal level of the images. Further, the bias level for the GMOS-N detectors is very stable, varying less than 0.2ADU from run to run. Twilight flat fields were created from all the available twilight flats taken during each of the GMOS-N observing runs (`giflat`). The overscan section of the images were trimmed off, and the images were bias subtracted and flat fielded using the matching calibration frames (`gireduce`). The three image extensions of each image were then mosaiced to form one image containing the data from all three GMOS-N detectors (`gmosaic`).

A.1.2. Fringing and scattered light

The detectors in GMOS-N have fringing at long wavelengths. The i' images have fringes which are about one per cent of the dark sky background peak-to-peak, while the fringing in the z' filter is about 5 per cent peak-to-peak. Example fringe frames are available on the Gemini web pages. The r' images have a scattered light at a low level.

Fringe frames were derived for the i' and z' images; a scattered light frame was derived for the r' images. The technique is the same for all three filters. We describe the technique actually used, but note that from the Gemini IRAF package v1.7 the construction of the fringe frames can be done with the task `gifrings`. The starting point is the mosaiced images from `gmosaic`. The goal is to produce frames that are cleaned of signal from objects and have a mean level of zero, such that they contain only the contribution from the fringes and/or the scattered light. Mask files for the objects in the images were produced using the NIRI task `nisky`. The median sky level was subtracted from each image, and the images were median combined, omitting pixels that were flagged in the masks as containing signal from objects. The task `gemcombine` in the Gemini IRAF package was used. This task is just a wrapper for `imcombine` that enables processing of MEF files. The resulting frames for the i' and r' filters were then median filtered with a box of 3.6 arcsec by 3.6 arcsec (25 by 25 pixels for the binned data). The z' fringe frame cannot be median filtered, as the fringing occurs at a spatial scale of a few pixels.

The fringe and scattered light frames were subtracted from the individual mosaiced images. The level of fringing in the z' images varies significantly. The best scaling of the z' fringe frame was determined by visual inspection of the results from scalings between 0.9 and 1.1 in steps of 0.05. After subtraction of the fringe and scatter light frames the variations in the background are less than 0.1 per cent of the background level.

A.1.3. Co-addition of the images

The images were registered and co-added using the task `imcoadd`, which is part of the `gemtools` package in the Gemini IRAF package. The resulting image from `imcoadd` is the average of all the good pixels. The input images are scaled such that images taken under non-photometric conditions and/or at different airmasses can be correctly combined. The photometric zero point of the co-added image is identical to the first image in the stack. Therefore we always use images taken under photometric conditions as the first images in the stacks. The total exposure times, sky background and image qualities of the co-added images are listed in Table 2.

TABLE A8
GMOS-N PHOTOMETRIC ZERO POINTS

Filter	m_{zero}	$N_{\text{obs}}^{\text{a}}$	k^{b}
r'	28.05 ± 0.015	7	0.11
i'	27.78 ± 0.023	7	0.10
z'	26.63 ± 0.014	8	0.05

^aNumber of individual measurements

^bMedian atmospheric extinction for Mauna Kea

TABLE A9
GMOS-N COLOR TERMS: LINEAR RELATIONS

Δm (1)	rms (2)	Color term fit (3)	rms(fit) (4)	N (5)	Color interval (6)
Δr_{zero}	0.045 ^a	$(0.042 \pm 0.004)(r' - i') - (0.011 \pm 0.002)$	0.043	1084	$-0.35 \leq (r' - i') \leq 2.2$
Δi_{zero}	0.054 ^a	$(0.113 \pm 0.008)(i' - z') - (0.010 \pm 0.002)$	0.049	1081	$-0.3 \leq (i' - z') \leq 0.85$
Δz_{zero}	0.055 ^b	$(0.125 \pm 0.012)(i' - z') - (0.014 \pm 0.003)$	0.050	492	$-0.3 \leq (i' - z') \leq 0.68$
		$(1.929 \pm 0.177)(i' - z') - (1.188 \pm 0.127)$	0.043	12	$0.6 \leq (i' - z') \leq 0.85$

NOTE. — (1) Residual zero point, (2) rms of Δm , equivalent to the expected uncertainty on the standard calibration if the color terms are ignored, (3) linear fits to the color terms, (4) rms of the linear fits, (5) number of individual measurements included in the fits, (6) color interval within which the linear fit applies.

^a $-0.7 \leq (r' - i') \leq 2.5$

^b $-0.7 \leq (r' - z') \leq 2.25$

A.1.4. Standard calibration of the photometry

The imaging have been calibrated using the exposures taken under photometric conditions on UT 2002 September 14 and using standard star observations obtained the same night. Four exposures in each filter were obtained of the Landolt (1992) standard star field PG0231+051. We use the transformation from Smith et al. (2002) to convert the standard magnitudes from the system used by Landolt to the Sloan-Digital-Sky-Survey (SDSS) photometric system. Then we establish the median zero points for each filter, see Table A8. Further, we have used all available standard star observations obtained with GMOS-N in the period between UT 2001 August 20 and UT 2003 December 26 to establish the color terms for the transformations. Full information about this calibration will be included in our paper that describes all the GMOS photometry for this project (Jørgensen et al., in preparation). Here we give only the relations used for the observations of RXJ0152.7–1357, see Table A9. The standard magnitudes are then derived as

$$m_{\text{std}} = m_{\text{zero}} + \Delta m_{\text{zero}} - 2.5 \log(N/t) - k(\text{airmass} - 1) \quad (\text{A1})$$

where t is the exposure time, N is the number of electrons above the sky level, airmass is the mean airmass for the exposure, k is the median atmospheric extinction at Mauna Kea, and Δm_{zero} is derived using one of the relations listed in Table A9. In order to make the information in the table more generally useful, we have also given the scatter relative to the nightly zero points in the case where the color terms are ignored (column (2) in Table A9). This is the average uncertainty to be expected on standard calibrated magnitudes if the color term is ignored, for objects with colors in the intervals listed in the notes to the table. The color terms are fairly small for r' and i' , while for z' the color term for RXJ0152.7–1357 cluster members with $(i' - z') \approx 0.8$ is about 0.35 mag.

A.1.5. Derived photometric parameters

We used SExtractor (v2.1.6, Bertin & Arnouts 1996) in 2-image mode, with the images pre-registered to each other. The image in the i' -filter was used for detections, while the images in the other two filters were used only for photometry. The background mesh size was adjusted to avoid systematic effects from the galaxies with the largest angular size. We use a background mesh size of 256 pixels, with a filter size of 5 pixels. Since the field is quite crowded, we used 64 sub-thresholds for the deblending of objects and a minimum contrast for the deblending of only 0.0005 (the default is 0.005). The results were visually inspected to ensure that all potential targets for spectroscopic observations were correctly deblended. Other adjustments to the SExtractor parameters were trivial adjustments for the magnitude zero points, the effective gains in the co-added images, and the image quality.

We adopt the best magnitudes (mag_{best}) from SExtractor as the total magnitudes of the objects. Aperture magnitudes and colors were derived within apertures with a diameter of 1.16 arcsec, which is approximately twice the FWHM of the point-spread-function of the images. The typical uncertainties on the magnitudes and colors are discussed in Section 4.1. Table A10 summarizes the total magnitudes and aperture colors for the galaxies included in the spectroscopic sample. The data in the table have not been corrected for the galactic extinction.

TABLE A10
PHOTOMETRIC DATA FOR THE SPECTROSCOPIC SAMPLE

ID	RA (J2000)	DEC (J2000) ^a	r'_{total}	i'_{total}	z'_{total}	$(r' - i)$	$(i' - z')$
103	1 52 32.77	-13 55 09.8	23.02	21.78	21.10	1.107	0.710
155	1 52 33.31	-13 55 23.0	22.76	21.72	21.03	0.942	0.779
193	1 52 50.80	-13 55 28.9	21.46	20.82	20.17	0.753	0.656
264	1 52 44.66	-13 55 37.3	22.30	21.40	20.68	1.001	0.672
338	1 52 43.33	-13 55 44.4	23.67	22.37	21.61	1.349	0.738
346	1 52 37.42	-13 55 50.1	22.68	21.24	20.56	1.390	0.791
422	1 52 34.59	-13 55 58.8	23.59	22.18	21.43	1.284	0.847
460	1 52 36.11	-13 56 08.5	22.26	20.99	20.24	1.320	0.810
523	1 52 42.38	-13 56 18.7	22.37	21.10	20.36	1.508	0.773
566	1 52 38.03	-13 56 28.1	22.33	21.14	20.40	1.399	0.752
627	1 52 38.48	-13 56 33.6	23.23	21.89	21.11	1.326	0.833
643	1 52 45.60	-13 56 40.0	23.15	21.82	21.03	1.457	0.817
737	1 52 45.77	-13 56 46.1	23.25	22.09	21.29	1.414	0.796
766	1 52 45.83	-13 56 59.2	22.10	20.67	19.88	1.515	0.795
776	1 52 38.48	-13 56 52.5	22.86	21.59	20.84	1.298	0.793
813	1 52 44.97	-13 57 04.2	22.17	20.78	19.99	1.503	0.783
896	1 52 36.99	-13 57 10.1	22.69	21.83	21.23	0.788	0.683
908	1 52 43.74	-13 57 19.4	22.13	20.93	20.14	1.410	0.784
1027	1 52 43.32	-13 57 26.7	23.24	22.03	21.23	1.448	0.817
1085	1 52 42.94	-13 57 35.0	22.91	21.40	20.61	1.534	0.791
1110	1 52 39.93	-13 57 42.6	22.59	21.29	20.50	1.521	0.781
1159	1 52 36.18	-13 57 48.8	23.02	21.66	20.93	1.374	0.794
1210	1 52 42.83	-13 57 55.3	23.40	22.04	21.31	1.453	0.785
1245	1 52 43.57	-13 58 00.0	22.72	21.78	21.07	1.059	0.672
1299	1 52 47.34	-13 59 26.1	22.59	21.05	20.30	1.593	0.787
1385	1 52 39.36	-13 59 04.5	22.58	21.50	20.87	1.040	0.635
1458	1 52 39.64	-13 58 56.6	23.59	22.08	21.35	1.444	0.767
1494	1 52 39.08	-13 58 48.8	19.22	18.59	18.00	0.635	0.584
1507	1 52 34.48	-13 58 42.2	23.86	22.44	21.74	1.305	0.829
1567	1 52 39.62	-13 58 26.7	22.10	20.90	20.09	1.526	0.796
1590	1 52 38.87	-13 58 32.0	24.00	22.37	21.58	1.547	0.808
1614	1 52 51.96	-13 58 17.1	22.52	21.30	20.55	1.434	0.806
1682	1 52 51.96	-13 58 15.6	22.39	21.23	20.45	1.369	0.788
1811	1 52 38.63	-13 59 20.8	23.90	22.56	21.89	1.406	0.807
1838	1 52 37.00	-14 00 05.3	22.93	22.23	21.57	0.710	0.535
1896	1 52 33.95	-14 00 11.9	23.99	22.72	21.94	1.187	0.878
1920	1 52 39.70	-13 59 14.3	23.24	22.25	21.53	1.312	0.807
1935	1 52 41.88	-13 59 53.6	22.88	21.38	20.61	1.459	0.777
1970	1 52 48.03	-13 59 58.6	21.15	20.56	19.94	0.621	0.676
2042	1 52 42.38	-13 59 46.6	19.91	19.45	18.91	0.551	0.550
2087	1 52 31.55	-13 59 40.1	20.53	19.88	19.28	0.618	0.702

NOTE. — Units of right ascension are hours, minutes, and seconds, and units of declination are degrees, arcminutes, and arcseconds.

^aPositions are consistent with USNO, with an rms scatter of ≈ 0.7 arcsec.

A.1.6. Calibration of the photometry to the rest frame

We have derived total magnitudes in the rest frame B-band from the observed i' magnitudes and colors ($i' - z'$). The calibration was established from Bruzual & Charlot (2003) stellar population models spanning the observed color range. These models are used to give the rest frame B magnitudes, as well as the observed i' and ($i' - z'$) at a given redshift. For each redshift, in steps of 0.025, we then fit the rest frame B magnitudes with the observed i' magnitude plus a second order polynomial in ($i' - z'$). When the calibration is used, the fitting coefficients are then interpolated to the exact redshift of the galaxy. More details will appear in our paper that describes all the GMOS photometry for the project (Jørgensen et al., in preparation). For reference, we here give the resulting equation for the cluster median redshift of 0.835,

$$B_{\text{rest}} = i' + 0.8026 - 0.4268(i' - z') - 0.0941(i' - z')^2 \quad (\text{A2})$$

The magnitude i' and the color ($i' - z'$) are corrected for galactic extinction before using Equation A2 to determine B_{rest} . The absolute B-band magnitude, M_B , is then derived as

$$M_B = B_{\text{rest}} - DM(z) + 2.5 \log(1 + z) \quad (\text{A3})$$

where $z = 0.835$ is the median cluster redshift and $DM(z) = 43.60$ is the distance modulus for RXJ0152.7–1357 for our adopted cosmology. See also Blanton et al. (2003) on techniques for how to calibrate to a “fixed-frame” system, like the rest frame B.

A.2. Spectroscopic data

A.2.1. Bias subtraction and flat field correction

The bias subtraction for the spectroscopic data is done in the same way as for the imaging data.

Quartz-halogen flat fields were taken during the nights, bracketing the science exposures. For each science exposure, the combination of the two flat fields taken closest in time was used to construct the normalized flat field. The flat fields were bias subtracted and trimmed the same way as for the imaging data, except the task `gsreduce` was used enabling the mask definition file (MDF) to be attached as an extension to the resulting MEF file. The MDF contains the information about the location of the slit-lets on the detector array. The flats were combined in sets corresponding to the science frames, and the flat fields were normalized extension by extension. To do so, a cubic spline was fit to the data, rejecting pixels that deviated more than $\pm 2.5\sigma$ from the fit. This technique is now part of `gsflat`.

The flat fields have emission lines at 6926 Å and 6940 Å. These emission lines originate from a surface inside the Gemini calibration unit. The pixels affected in the flat fields were set to 1.0, and these pixels cannot be flat field corrected.

The normalized flat fields were then applied to the science exposures, extension by extension (`gsreduce`). The resulting science exposures still have three extensions as the raw exposures, but have now been trimmed, bias subtracted and flat fielded.

A.2.2. Sky subtraction and fringe frames

The techniques implemented in Gemini IRAF package v1.7 for the sky subtraction of MOS data are different from the ones used for the current dataset. Because of the strong sky lines in the red, we developed a technique to subtract off the sky before any interpolation was done on the data. We also construct fringe frames and subtract these off prior to any interpolation of the data. For the spectroscopic data, the fringing is larger than ± 2 per cent for wavelengths longer than 700 nm.

The three extensions in the science exposures were temporarily pasted together to one image, using `gmosaic` with the paste flag set. This has the effect that no interpolation is done at this point, which is essential for the sky subtraction technique. The fact that no correction is done for the accurate positions of the three chips relative to each other is not important at this stage. The images were then cut into pieces corresponding to the spectra from the slit-lets. The first iteration of this was done with `gscut`, but the sections had to be manually adjusted to avoid the very edges of the slit-lets. The resulting images are MEF files with one image extension per slit-let.

The sky subtraction was done by fitting each slit-let in the spatial direction with a 2nd order polynomial rejecting pixels that deviate with more than $\pm 3\sigma$. An aperture of 1.45 arcsec at the object position was omitted from the fit. For the brightest cluster galaxy an aperture of 2.2 arcsec was used. Further, the fitting was iterated five times and the rejected pixels grown with two pixels to effectively eliminate signal from the objects and from cosmic ray hits.

For each of the two wavelength settings a fringe frame was constructed from the sky subtracted images by median combining these. Apertures around the objects were masked and not included in the combined images. The aperture sizes were between 1.67 and 3.13 arcsec, depending on the angular size of the objects. Because the observations are dithered in the spatial direction the resulting fringe frames have full spatial coverage. The result is two fringe frames, one for the central wavelength setting of 805 nm and one for 815 nm.

The fringe frames were subtracted from each of the individual images. The level of fringing varies and the best scaling of the fringe frames was determined by inspecting the results from scaling between 0.60 and 2.00, in steps of 0.05.

A.2.3. Combination of the individual exposures

The images taken at each wavelength setting were then combined. The images were shifted in the spatial direction to compensate for the dithering along the slit. The combined images were put back into the original three extensions and then mosaiced using `gmosaic` with the full transformations enabled. Thus, in this step the task is used to correct for the relative position of the three chips. The slit-lets were then cut out and put in individual extensions, using the task `gscut`.

A.2.4. Wavelength calibration and extraction

The wavelength calibrations were established from CuAr spectra (`gswavelength`). The dispersion function was fit with a 6th order polynomial. The rms of the fits were typically 0.25 Å (0.4 pixels). The wavelength calibrations were applied to the combined spectra for each wavelength setting (`gsttransform`). The gaps between the CCDs in GMOS result in gaps in the wavelength coverage for each of the wavelength settings.

The wavelength calibrated spectra from the two wavelength settings were combined using `scombine`. The gaps were masked by setting the pixel values to -1000 ADU and the pixels were excluded from the combined images by applying a threshold in `scombine`. With the release of IRAF 2.12.2a, this step can be accomplished with the task `lscombine`.

The spectra were then traced and extracted using `gsextract`, which is a wrapper for `apall` enabling easy processing of MEF files. The spectra were extracted in apertures that are 1.15 arcsec wide. For some of the slits, the wavelength range goes redwards of 10300 Ångstrom, where 2nd order contamination is significant. This part of the spectrum was deleted from the trace as it is offset from the 1st order trace because of the atmospheric differential refraction.

A.2.5. Correction for telluric lines

Slits for two blue stars were included in the mask design in order to enable correction for the telluric lines. Together the two blue stars provide complete wavelength coverage for all the spectra of the science targets. The spectra of the two blue stars were combined using `scombine`. The resulting spectrum was normalized by fitting it with a 27-piece cubic spline and dividing it with the fit. The wavelength ranges unaffected by telluric lines were set to one. The science spectra were then divided by the telluric line spectrum. Figure A10 shows the spectra of the blue stars before and after removal of the telluric lines as well as the resulting normalized telluric absorption spectrum that was applied to all the galaxy spectra. The stellar spectra shown on this figure have not been flux calibrated.

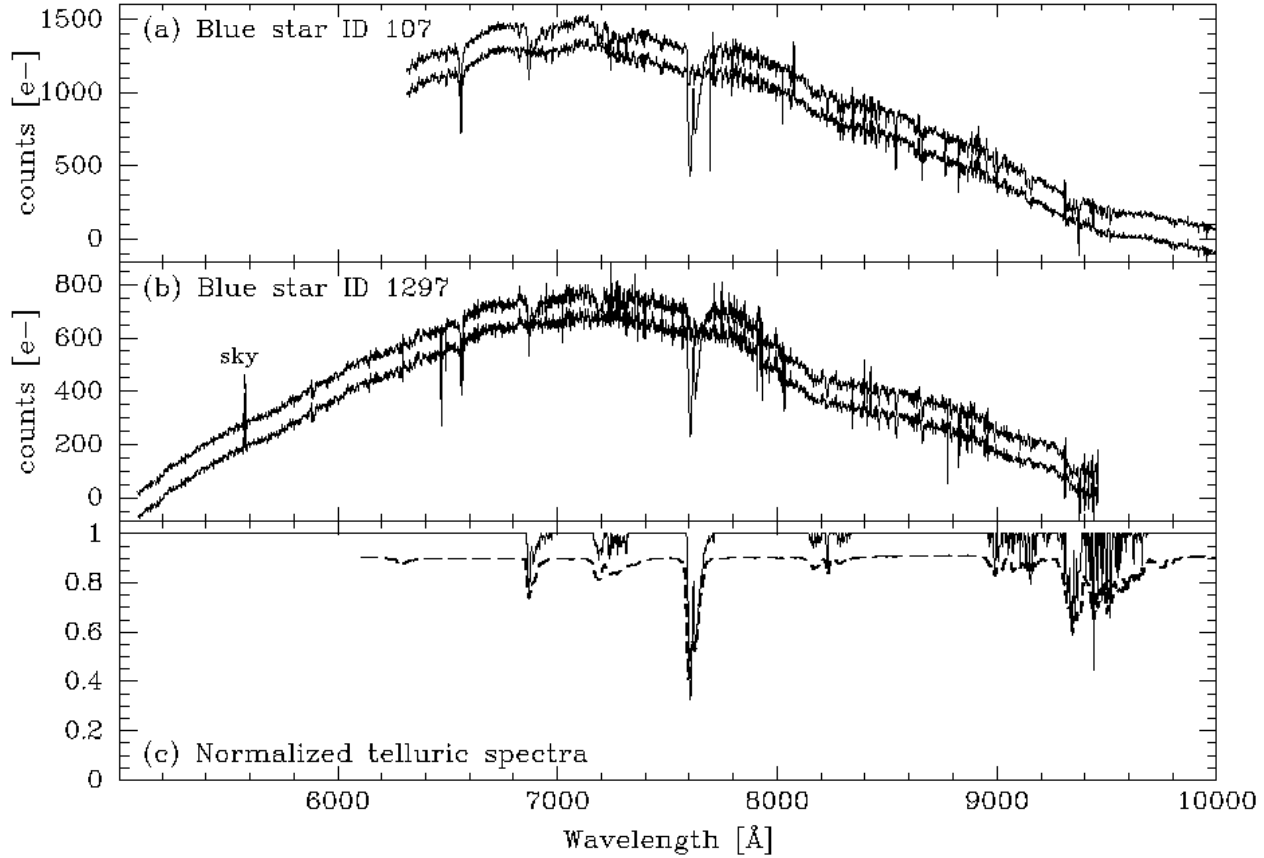


FIG. A10.— (a) & (b) Spectra of the two blue stars used to construct the telluric absorption line spectrum. Top line – the spectra before applying the telluric absorption correction; bottom line – the spectra after applying the telluric absorption correction, for clarity offset with 10 per cent of the peak signal. (c) Thin solid line – normalized telluric absorption spectrum; thick dashed line – for reference a lower resolution normalized telluric absorption spectrum from the Gemini Integration Time Calculator, for clarity offset with 10 per cent.

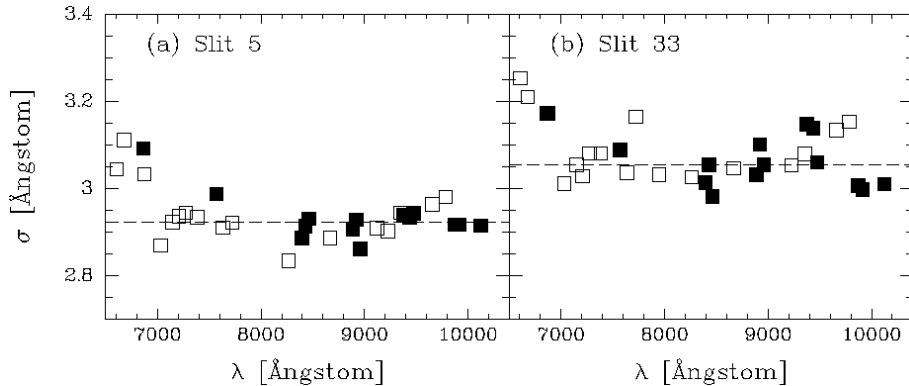


FIG. A11.— Instrumental resolution as a function of wavelength for two of the slit-lets. Open symbols – instrumental resolution derived from CuAr arc spectra; filled symbols – instrumental resolution derived from single sky frame.

A.2.6. Relative flux calibration

Because MOS spectra cover different wavelength ranges depending on where in the field of view the slit-lets are located, the spectra cannot be flux calibrated using a single observation of a standard star. Instead several observations were used spanning a range in central wavelength, such that when these were combined the resulting sensitivity function covers all wavelength ranges covered by the MOS spectra. The extracted spectra were flux calibrated with this sensitivity function. The calibration is relative since the slit width used for the standard star observations is 1 arcsec and some of the observations of RXJ0152.7–1357 were taken through thin cirrus.

A.2.7. Instrumental resolution and resampling of the spectra

Determination of the instrumental resolution is needed in order to derive the internal velocity dispersions of the galaxies. We derived the instrumental resolution both from gaussian fits to the isolated lines in the CuAr arc spectra and from gaussian fits to

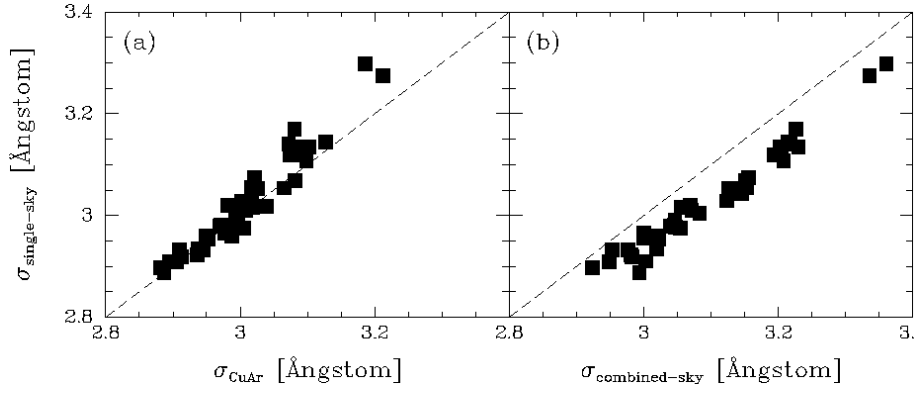


FIG. A12.— Median instrumental resolution derived from a single sky frame versus (a) the instrumental resolution derived from CuAr arc spectra, and (b) the instrumental resolution derived from the sky spectra combined the same way as the science spectra. The dashed lines on both panels are the one-to-one relations. Combining the science spectra degrades the instrumental resolution with 0.065\AA .

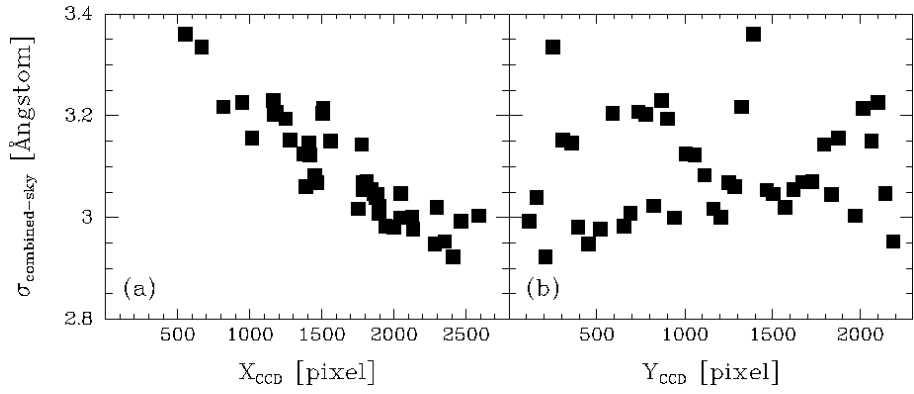


FIG. A13.— Median instrumental resolution derived from the combined sky frame versus position on the detector. The instrumental resolution depends on the X-position of the slit.

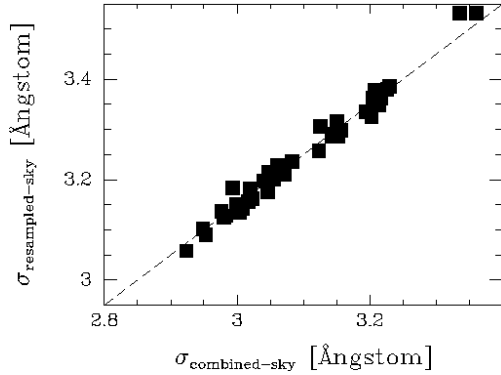


FIG. A14.— Median instrumental resolution derived from the combined sky frame median filtered and resampled to the critical resolution versus the median instrumental resolution before median filtering and resampling. The median filtering and resampling degrades the instrumental resolution with 0.15\AA . The dashed line is offset with 0.15\AA from the one-to-one relation.

skylines. Since the final science spectra were extracted from the combination of many individual frames, the analysis of the sky lines was done on both a single frame and on a combined frame processed in the same way as the science spectra. By comparing the results from the single sky frame and the combined frame we can assess to what extent the process of combining the individual frames degrades the instrumental resolution.

The skylines are significantly more crowded than the CuAr lines, due to the wavelength interval covered by the spectra. Therefore, the continuum of the sky was first subtracted off by fitting a low order polynomial to the sky spectra. The signal from the sky emission lines were omitted by using iterative rejection of positive residuals from the fit. Then the sky lines were fit with gaussian profiles, assuming that the background was zero.

Figure A11 shows the instrumental resolution as a function of wavelength for two of the slit-lets. Both the CuAr spectra and the sky spectra show that the instrumental resolution does not depend significantly on the wavelength. Figure A12a shows the median values of the instrumental resolution derived from the single sky frame versus the results from the CuAr arc spectra for

TABLE A11
GMOS-N TEMPLATE SPECTRA

Star	Spectral type	V_{hel} km s^{-1}	Wavelength coverage (\AA)	$\sigma_{\text{inst}}^{\text{a}}$
HD172958	B8V	-16.0	3674.8 \AA – 6539.2 \AA	1.253
HD030649	G1V	26.0	3746.7 \AA – 6630.8 \AA	0.940
HD172401	K0III	23.6	3674.3 \AA – 6539.1 \AA	1.243

^aEffective instrumental resolution, see text for details

all slit-lets. The resolutions derived from the CuAr arc spectra and the single sky frame are consistent. Figure A12b shows the results from the single sky frame versus the combined sky frame. The instrumental resolution of the combined sky frame is on average 0.065 \AA worse than the resolution of the single sky frame. This small degradation is caused by combining the 25 individual frames.

The instrumental resolution varies from slit to slit. In Figure A13 we show the instrumental resolution as a function of the slit’s position on the detector array. The instrumental resolution depends on the X-position. While the cause of this is not clear, the important conclusion for the present use of the data is that we will use the individual values for the instrumental resolution when determining the internal velocity dispersions of the galaxies.

The original sampling of the spectra oversamples the spectral resolution. We median filtered the spectra with 5 pixels in the spectral direction, and then resampled them to have 2.75 \AA per pixel, which is just above the critical sampling for the instrumental resolution. This process degrades the resulting instrumental resolution slightly, see Figure A14. This degradation is taken into account in our determination of the internal velocity dispersions of the galaxies.

A.2.8. Determination of redshifts and velocity dispersions

For the determination of the redshifts and the velocity dispersions, we used observations of three template stars obtained with GMOS-N using the B600 grating and a slit width of either 0.75 arcsec or 0.50 arcsec. Information about the template spectra is listed in Table A11. The template stars were observed with the star stationary in the slit. Thus, the effective instrumental resolution is partly determined by the image quality of the observation. Therefore, the effective instrumental resolution for each of the template spectra was derived by comparing the spectra to other template stars observed with GMOS-N using a technique that fills the slit with signal. Those other template star observations have shorter and more redwards wavelength coverage and are therefore not optimal for use for the spectra of RXJ0152.7–1357. The effective instrumental resolution for each of the template spectra is given in Table A11.

Initial redshifts were derived by cross-correlating the spectra with a spectrum of the K0III star HD172401. Several template spectra were constructed by offsetting the template spectrum to redshifts between 0.3 and 0.9. Then the galaxy spectra were cross-correlated with the template closest in redshift, using the task `XCOR`, which is part of STSDAS². For galaxies with obvious emission lines, the emission lines were used for the initial determination of the redshift of the galaxy.

Once the redshift had been determined to an accuracy of about 200 km s^{-1} , velocity dispersions as well as more accurate redshifts were derived using software made available by Karl Gebhardt. The software uses penalized maximum likelihood fitting in pixel space to determine the velocity dispersion and the redshift, see Gebhardt et al. (2000, 2003) for a detailed description of the fitting method.

We used the three template stars simultaneously in order to limit the systematic errors introduced by template mis-match. Further, wavelength ranges affected by emission lines or strong residuals from the sky subtraction were masked and not used for the fitting. The blue limit for the fitted wavelength ranges was in all cases 3750 \AA in the rest frame of the galaxy such that the [O II] emission line was excluded from all fits. The red limit was chosen to be as far red as the S/N would allow. For the cluster members we typically used a limit of 5050 \AA in the rest frame of the galaxy.

Gebhardt’s software is written primarily for processing of spatially resolved spectra of nearby galaxies. We therefore wrote an interface to the program that takes care of shifting both input galaxy spectra and template stars to the rest frame, after which all fitting is done in the rest frame. The interface limits the wavelength range fitted to the wavelength range in common after the shifts to the rest frame. The interface also convolves the template spectra to the instrumental resolution for each of the galaxy spectra. The results from the fitting are a refined redshift and the best fitting velocity dispersion. Uncertainties are determined from Monte-Carlo simulations. Further, the output contains information about the fractional composition of the best fitting template spectrum made from the three input template spectra. This can be used as a crude spectral classification of the galaxy spectra.

The derived velocity dispersions were corrected for the size of the aperture using the technique described in Jørgensen et al. (1995). We correct the velocity dispersions to a standard aperture size with a radius r_{norm} , which is equivalent to 1.7 arcsec at the distance of the Coma cluster. For members of RXJ0152.7–1357 the correction to the velocity dispersions is \approx 6 per cent.

Table A12 summarizes results from the template fitting. Measured velocity dispersions as well as aperture corrected velocity dispersions are listed for the cluster members. For galaxies that are not members of the cluster, we give the redshift. The detailed data for these galaxies will be discussed in a future paper.

² STSDAS is a product of Space Telescope Science Institute, which is operated by AURA for NASA.

TABLE A12
RESULTS FROM TEMPLATE FITTING

ID	Redshift	Member ^a	$\log \sigma$	$\log \sigma_{\text{cor}}^{\text{b}}$	$\sigma_{\log \sigma}$	Template fractions			S/N ^c
						B8V	G1V	K0III	
103	0.6406	0	34.8
155	0.9955	0	22.1
193	0.4562	0	34.2
264	0.5341	0	26.5
338	0.8193	1	2.057	2.084	0.057	0.19	0.54	0.28	29.8
346	0.8367	1	2.152	2.179	0.050	0.08	0.69	0.23	52.4
422	0.8342	1	2.009	2.036	0.070	0.00	0.65	0.35	35.0
460	0.8649	0	80.0
523	0.8206	1	2.352	2.379	0.038	0.00	0.65	0.35	62.1
566	0.8369	1	2.184	2.211	0.055	0.29	0.46	0.25	31.4
627	0.8324	1	2.259	2.286	0.048	0.00	0.55	0.45	25.4
643	0.8445	1	2.238	2.265	0.102	0.08	0.68	0.24	30.8
737	0.8384	1	2.152	2.179	0.056	0.00	0.65	0.35	27.2
766	0.8346	1	2.362	2.389	0.036	0.00	0.51	0.49	45.7
776	0.8325	1	2.052	2.079	0.049	0.19	0.48	0.32	57.5
813	0.8351	1	2.312	2.339	0.031	0.00	0.56	0.44	64.9
896	0.8458	1	1.639	1.666	0.049	0.65	0.35	0.00	16.1
908	0.8393	1	2.237	2.264	0.041	0.00	0.69	0.31	45.8
1027	0.8357	1	2.290	2.317	0.034	0.00	0.47	0.53	29.6
1085	0.8325	1	2.361	2.388	0.032	0.00	0.47	0.53	49.0
1110	0.8322	1	2.276	2.303	0.051	0.00	0.48	0.52	39.8
1159	0.8357	1	2.150	2.177	0.087	0.29	0.49	0.22	32.3
1210	0.8372	1	2.079	2.106	0.085	0.00	0.51	0.49	24.8
1245	0.7875	0	27.8
1299	0.8374	1	2.130	2.157	0.052	0.30	0.45	0.26	24.8
1385	0.8368	1	2.134	2.161	0.075	0.63	0.37	0.00	26.6
1458	0.8324	1	2.132	2.159	0.066	0.00	0.66	0.34	30.9
1494	0.2374	0	380.
1507	0.8289	1	2.311	2.338	0.051	0.19	0.61	0.20	22.9
1567	0.8291	1	2.461	2.488	0.030	0.10	0.41	0.49	32.7
1590	0.8317	1	1.959	1.986	0.078	0.21	0.19	0.60	28.0
1614	0.8433	1	2.321	2.348	0.041	0.06	0.66	0.28	29.8
1682	0.8463	1	2.240	2.268	0.050	0.11	0.57	0.33	43.2
1811	0.8351	1	1.735	1.762	0.076	0.00	0.55	0.45	18.0
1838	0.7450	0	28.2
1896	0.9810	0	29.0
1920	0.8442	1	1.569	1.596	0.134	0.06	0.34	0.60	10.0
1935	0.8252	1	2.177	2.204	0.058	0.00	0.71	0.29	34.4
1970	0.3775	0	21.7
2042	0.2362	0	42.5
2087	0.3320	0	102.

^aAdopted membership: 1 – galaxy is a member of RXJ0152.7–1357; 0 – galaxy is not a member of RXJ0152.7–1357

^bVelocity dispersions corrected to a standard size aperture equivalent to a circular aperture with diameter of 3.4 arcsec at the distance of the Coma cluster.

^cS/N per Ångstrom in the rest frame of the galaxy. The S/N was derived in the rest frame wavelength interval 4100–4600 Å, except for ID 1494, 2042, and 2087 for which the wavelength interval 5500–6000 Å was used.

A.2.9. The instrumental resolution – effects on the derived velocity dispersions

In order to determine at which velocity dispersion and S/N the determination of the velocity dispersions becomes affected by systematics we have made model galaxy spectra from our three template stars. The model galaxy spectra cover velocity dispersions from 50 km s⁻¹ to 300 km s⁻¹, and average S/N from 10 to 50 per Ångstrom in the rest frame. The noise is modeled from a noise spectrum that contains the average variation with wavelength, due to sky lines and system throughput, that applies to the RXJ0152.7–1357 cluster members. The model spectra match the instrumental resolution and the sampling of the real data. Three sets of model spectra were made with mixes of the templates {B8V, G1V, K0III} of {0.25, 0.5, 0.25}, {0., 0.5, 0.5}, and {0., 0., 1.}, respectively. For each model spectrum we derive the velocity dispersion as for the real data, using all three template stars. We made 100 realizations of each combination of velocity dispersion and S/N. We then derived the median values of $\log \sigma$ for the 100 realizations.

Figure A15a and b shows the systematic errors in $\log \sigma$ as the difference between the input $\log \sigma$ and median value from the simulation, as a function of the S/N of the model and the input $\log \sigma$. The template mix turned out to have very little effect on the systematic errors. Thus, Figure A15 shows only the result from the 50/50 mix of the G1V and K0III templates. Further, the S/N of the spectra does not significantly affect the systematic error, see Figure A15b. This is different from what has been found for the Fourier Fitting Technique where low S/N leads to larger systematic errors (e.g., Jørgensen et al. 1995). Velocity dispersions below

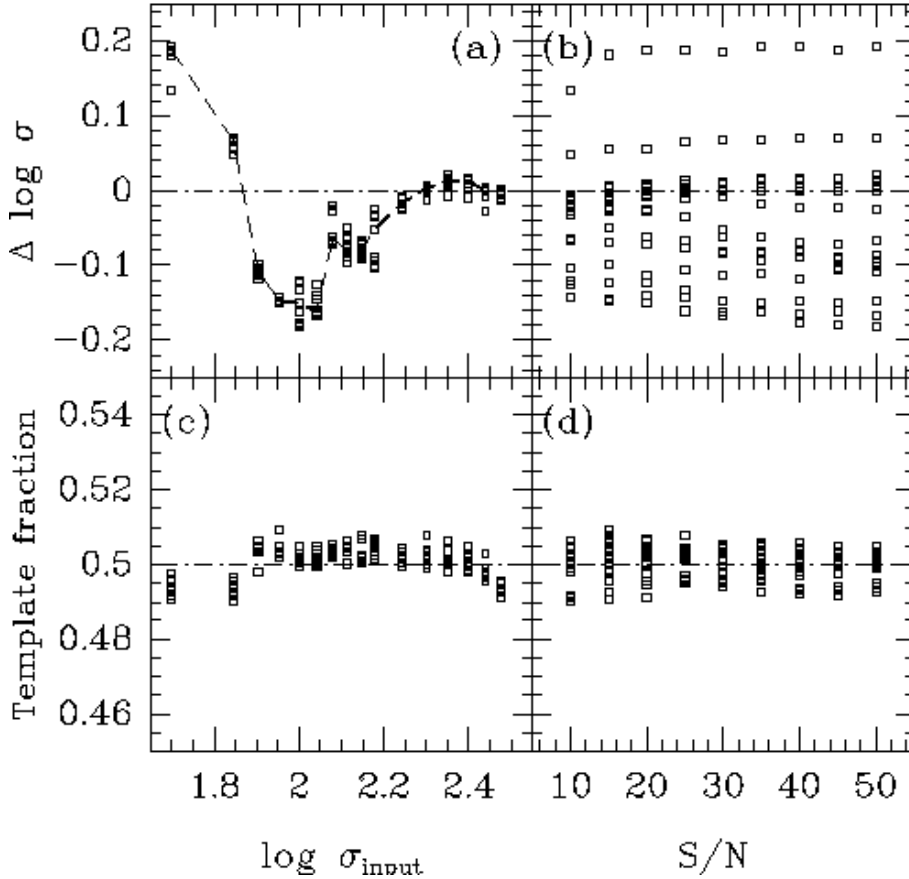


FIG. A15.— Results from simulations. The systematic error on $\log \sigma$, $\Delta \log \sigma = \log \sigma_{\text{output}} - \log \sigma_{\text{input}}$, (a) as a function of $\log \sigma_{\text{input}}$, and (b) as a function of S/N per Ångström. The dashed line on panel (a) marks the median values of $\Delta \log \sigma$. The output template fractions (c) as a function of $\log \sigma_{\text{input}}$, and (d) as a function of S/N per Ångström. See text for discussion.

the instrumental resolution ($\log \sigma = 2.06$) may be subject to systematic errors as large as ± 0.15 in $\log \sigma$; for velocity dispersions smaller than 0.5 times the instrumental resolution the systematic effects are larger. According to the models, the systematic errors lead to both underestimated and over estimated velocity dispersions depending on the value of the input velocity dispersion. For input velocity dispersions of 0.5-1.0 times the instrumental resolution the velocity dispersions get underestimated, while for smaller input velocity dispersions the systematic errors lead to overestimated velocity dispersions. The galaxies ID 896, 1811, and 1920 have velocity dispersions of less than ≈ 0.5 times the instrumental resolution and the measurements therefore are expected to be affected by systematic effects. The galaxies ID 422 and 1590 have velocity dispersions slightly below the instrumental resolution. According to the models, the measurements for these galaxies may be subject to systematic errors of the order 0.1 on $\log \sigma$. This is similar to the size of the random uncertainties for these galaxies. In the analysis of scaling relations involving $\log \sigma$ we exclude the three low dispersion galaxies from the fits. Further, we use median zero points for our analysis in order to limit the effect of the systematic errors in $\log \sigma$ on our results.

Figure A15c and d show the output template fractions as a function of the input velocity dispersion and the S/N. Independent of the velocity dispersion and the S/N, the output template fractions are within 0.01 of the input template fractions.

A.2.10. Determination of line indices

Absorption line indices were derived from the spectra. For indices in the Lick/IDS system, the definitions from Worthey et al. (1994) were used. In addition we determined the indices for $H\gamma$ and $H\delta$ defined by Worthey & Ottaviani (1997), the $H\beta_G$ index defined by Jørgensen (1997), the D4000 index defined by Bruzual (1983), see also Gorgas et al. (1999), and the blue indices CN3883 and CaHK defined by Davidge & Clark (1994). The passbands for the indices are shown on Figure A16. Indices redwards of C4668 are for galaxies in RXJ0152.7–1357 severely affected by sky subtraction residuals. Thus, these indices were not measured. Figure A16 shows the passbands for the indices measured for the RXJ0152.7–1357 galaxies.

The spectra were convolved to the instrumental resolution of the Lick/IDS spectra, in the rest frame of the galaxies. We adopted the instrumental resolution of the Lick/IDS spectra presented in Worthey & Ottaviani (1997). The indices and uncertainties, based on the noise spectra, were then derived.

The raw values of the indices were corrected for the velocity dispersion of the galaxy, following the technique described by, e.g., Davies et al. (1993). We used the spectra of three template stars used for the determination of the velocity dispersions to derive the corrections for the velocity dispersion. The indices are of three different types, equivalent widths (EW), ratios or

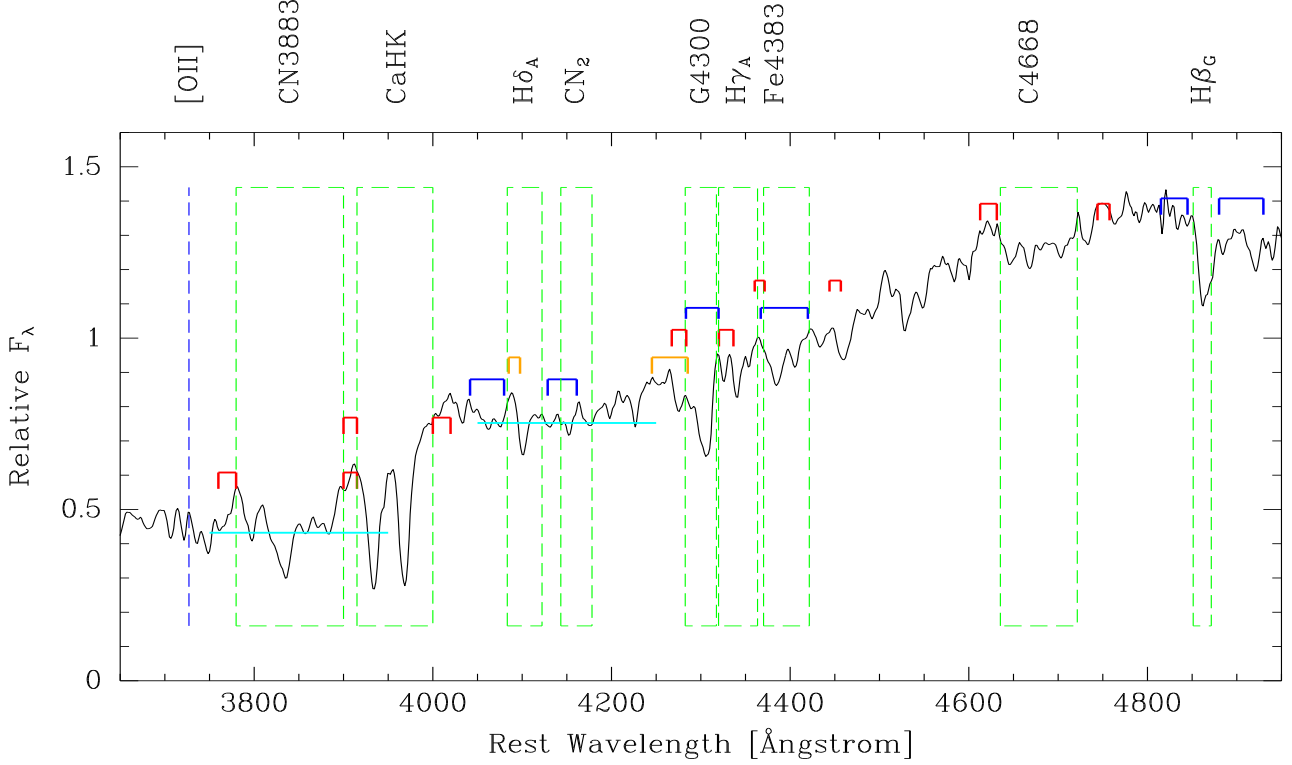


FIG. A16.— Passbands for the line indices. The spectrum is the composite of the 22 cluster members that do not have emission lines. The on-line passband for each index is marked as the dashed green box. The continuum passbands are marked in blue (for the Balmer lines), orange (for CN_2) or red (all other metal line indices). Except for CN_2 , the continuum passbands are very close to the on-line passbands. The D4000 passbands are marked as horizontal cyan lines. The location of the $[\text{O II}]$ emission line is marked, though the line is not present in the spectrum. The passbands for $\text{H}\beta_{\text{G}}$ are marked, though this index cannot be measured reliably from the spectra of individual RXJ0152.7–1357 galaxies.

magnitudes, see Table A13. For indices derived as EW or ratios the corrected indices, index_0 were derived as

$$\text{index}_0 = C(\sigma) \cdot \text{index} \quad (\text{A4})$$

where index is the value derived for the galaxy, $C(\sigma)$ is the correction factor, and index_0 is the corrected index for a zero velocity dispersion. For indices derived in magnitudes, we used

$$\text{index}_0 = C(\sigma) + \text{index} \quad (\text{A5})$$

For each galaxy, a composite template was constructed using the template fractions found from the template fitting, see Table A12. The composite template was convolved to the Lick/IDS resolution and the line indices derived. Then the composite template was convolved with the velocity dispersion found for the galaxy, and the line indices derived. The corrections $C(\sigma)$ for the galaxy were derived as the ratio or difference, as specified in Eqs. A4 and A5.

The velocity dispersion correction factor for a composite template of $0.5\text{G1V} + 0.5\text{K0III}$ and a velocity dispersion of 230 km s^{-1} is listed in Table A13. The corrected indices are in general stronger than the uncorrected indices. For the indices UVcont , NH3360 , and BL3580 we cannot determine the velocity dispersion correction since the template star spectra do not cover these short wavelengths. However, since all the passbands are quite broad for these indices we expect the corrections to be insignificant.

Galaxies have radial gradients in the line strengths. Thus, the line indices need to be aperture corrected. However, the aperture correction is not known for most of the line indices derived. For line indices also measured by Jørgensen (1997) we have adopted the aperture correction described in that paper. For the remaining line indices, we have estimated the aperture corrections in the same way as done by Jørgensen (1997), by comparing measurements of radial gradients from various previous studies. We used data from Vazdekis et al. (1997), Cardiel et al. (1998), and Davidge & Clark (1994). For indices measured as equivalent width in Angstrom or as a ratio (D4000 and UVcont), we assume that the aperture correction can be written as

$$\text{index}_{\text{norm}} = \text{index}_{\text{ap}} \cdot \left(\frac{r_{\text{ap}}}{r_{\text{norm}}} \right)^\alpha \quad (\text{A6})$$

For indices measured in magnitudes we use

$$\text{index}_{\text{norm}} = \text{index}_{\text{ap}} + \alpha \log \frac{r_{\text{ap}}}{r_{\text{norm}}} \quad (\text{A7})$$

The standard size aperture has a radius, r_{norm} , equivalent to 1.7 arcsec at the distance of the Coma cluster. The assumption about the aperture corrections and the standard size aperture are consistent with the method used in Jørgensen (1997). For the indices

TABLE A13
CORRECTIONS TO THE LINE INDICES

Index	Type	$C(\sigma)^a$	α	Reference ^b
UVcont	Ratio	...	0.035	1
NH3360	EW	...	0.05	1
BL3580	EW	...	0.05	1
CN3883	mag	0.003	0.05	1
CaHK	EW	1.009	0.025	2
D4000	Ratio	1.000	0.03	4
H δ_A	EW	1.114	0.0	
H δ_F	EW	1.158	0.0	
CN1	mag	0.002	0.04	2
CN2	mag	0.006	0.04	2
Ca4227	EW	1.297	0.05	3
G4300	EW	1.035	0.015	2
H γ_A	EW	1.009	0.0	
H γ_F	EW	1.014	0.0	
Fe4383	EW	1.110	0.05	2
Ca4455	EW	1.240	0.05	3
Fe4531	EW	1.078	0.05	3
C4668	EW	1.048	0.08	3
H β	EW	1.031	-0.005	3
H β_G	EW	1.051	-0.005	3
Mg b	EW	0.002	0.05	3
Mg $_1$	mag	0.002	0.04	3
Mg $_2$	mag	1.112	0.04	3
Fe5270	EW	1.134	0.05	3
Fe5335	EW	1.289	0.05	3
NaD	EW	1.064	0.09	3

REFERENCES. — (1) – Davidge & Clark (1994); (2) – Vazdekis et al. (1997); (3) – Jørgensen (1997); (4) – Cardiel et al. (1998).

^aCorrection to zero velocity dispersion for a galaxy with a velocity dispersion of 230 km s⁻¹ and a template mix of 0.5G1V+0.5K0III.

^bMain source for radial gradient data, or the reference for a previously used value of the aperture correction coefficient α .

Ca4227 and Ca4455 we adopted the same aperture correction as used for the Fe-indices. In Table A13 we list the adopted values for the coefficient α and the main source of radial gradient data used to estimate the coefficient. For completeness, the corrections are also listed for weaker indices in the blue, for H β_G , and for the Mg, Fe and Na indices in the visible region, though these indices cannot be measured for the RXJ0152.7–1357 galaxies. The higher order Balmer line indices (H γ_A , H γ_F , H δ_A , H δ_F) have not been aperture corrected. The correction coefficient for H β determined by Jørgensen (1997) is -0.005 , giving a correction for H β of the order 0.5 per cent for galaxies in RXJ0152.7–1357. Therefore the aperture corrections for the higher order Balmer line indices may be small enough that they can be safely ignored. We note that the continuum bands for the H γ_A index overlap the G4300 feature and the Fe4383 line. Thus, H γ_A may have an aperture correction of a similar size as the G4300 and Fe4383 indices and with the opposite sign. Using the average of the aperture correction for those two indices, we estimate that ignoring the aperture correction for H γ_A , on average may make the corrected indices 0.2 too large. This is not significant for the current analysis.

The Lick/IDS system was established from spectra that were not flux calibrated. Therefore, offsets between indices measured from flux calibrated spectra and the Lick/IDS system are expected. Several authors have derived such offsets, in particular, Worthey & Ottaviani (1997) and Jørgensen (1997). For indices measured from narrow passbands, Jørgensen (1997) finds no significant offsets. Worthey & Ottaviani find offsets of similar size, though they do not comment on whether the offsets are significant. For Mg $_1$ and Mg $_2$, both studies find significant offsets and the results are consistent. Jørgensen lists offsets for Mg $_1$ and Mg $_2$ of 0.007 and 0.011, respectively, with the Lick/IDS indices being larger. For CN $_1$ and CN $_2$, Worthey & Ottaviani find very small offsets, 0.003 and 0.004, respectively. Given the small size of the offsets, we choose in this project to only offset measurements of Mg $_1$ and Mg $_2$ to the Lick/IDS system. We adopt the offsets given by Jørgensen (1997); these offsets are added to the measured indices.

Tables A14 lists the fully corrected values of the measured line indices for galaxies in RXJ0152.7–1357.

A.3. Presentation of the spectra and imaging

The spectra of the cluster members are shown in Figure A17. Stamp-sized color images of the galaxies are shown in Figure A18. We have chosen to show the color images based on the HST imaging obtained with the ACS, rather than the GMOS-N imaging, such that these images show the morphologies of the galaxies.

TABLE A14
LINE INDICES AND EW[O II] FOR CLUSTER MEMBERS

ID	CN3883	CaHK	D4000	H δ_A	CN ₁	CN ₂	G4300	H γ_A	Fe4383	C4668	EW [O II]
338	0.180	23.94	2.019	1.39	0.027	0.027	5.48	-4.32	1.81	4.34	...
338	0.005	0.36	0.005	0.21	0.000	0.000	0.31	0.36	0.30	0.31	...
346	0.183	23.26	1.961	1.52	0.027	0.040	3.33	-3.56	2.49	6.89	...
346	0.003	0.25	0.003	0.13	0.000	0.003	0.18	0.17	0.12	0.19	...
422	0.238	21.69	2.057	-0.50	0.103	0.128	5.68	-4.50	2.76	8.21	...
422	0.005	0.36	0.005	0.19	0.005	0.005	0.25	0.26	0.19	0.26	...
523	0.282	21.25	2.048	0.40	0.087	0.121	4.52	-3.77	4.16	5.37	...
523	0.003	0.18	0.002	0.11	0.003	0.003	0.14	0.16	0.14	0.14	...
566	0.173	24.42	2.094	2.97	0.027	0.027	6.56	-2.80	3.30	4.78	8.4
566	0.005	0.42	0.005	0.21	0.000	0.000	0.29	0.30	0.20	0.33	1.6
627	0.318	23.26	2.116	0.01	0.051	0.088	3.75	-4.18	4.67	6.42	...
627	0.007	0.49	0.006	0.26	0.006	0.006	0.36	0.38	0.26	0.34	...
643	0.194	23.84	2.039	2.61	0.027	0.027	8.57	-8.64	5.51	6.92	8.2
643	0.005	0.44	0.005	0.19	0.000	0.000	0.27	0.30	0.17	0.33	1.4
737	0.206	17.73	1.995	1.83	0.043	0.068	3.42	-3.54	2.30	3.24	...
737	0.005	0.46	0.005	0.24	0.006	0.006	0.30	0.32	0.22	0.39	...
766	0.278	22.36	2.042	-0.78	0.120	0.150	4.81	-4.77	2.95	8.00	...
766	0.003	0.25	0.003	0.14	0.004	0.004	0.18	0.19	0.14	0.23	...
776	0.172	19.88	1.942	1.84	0.049	0.072	3.11	-1.93	2.47	4.39	...
776	0.003	0.21	0.002	0.11	0.003	0.003	0.15	0.16	0.12	0.17	...
813	0.266	20.63	2.129	1.31	0.071	0.100	5.50	-5.47	2.59	8.99	...
813	0.002	0.20	0.002	0.10	0.002	0.002	0.13	0.14	0.10	0.14	...
896	0.074	6.83	1.400	4.09	0.027	0.027	2.32	2.88	-3.53	-13.52	21.6
896	0.006	0.66	0.006	0.31	0.000	0.000	0.55	0.51	0.35	0.88	2.3
908	0.227	20.83	2.005	-0.02	0.043	0.072	5.51	-4.65	3.28	8.30	...
908	0.003	0.27	0.003	0.15	0.003	0.003	0.18	0.21	0.13	0.21	...
1027	0.323	22.35	2.179	-1.19	0.073	0.098	4.33	-3.90	5.49	7.71	...
1027	0.006	0.44	0.006	0.23	0.005	0.005	0.30	0.30	0.21	0.30	...
1085	0.269	22.63	2.160	-0.33	0.097	0.127	5.72	-5.01	3.42	8.22	...
1085	0.004	0.26	0.003	0.13	0.003	0.003	0.18	0.20	0.14	0.18	...
1110	0.274	22.44	2.245	0.34	0.120	0.140	3.07	-4.06	5.04	6.32	...
1110	0.005	0.33	0.004	0.17	0.004	0.004	0.22	0.24	0.17	0.23	...
1159	0.145	19.32	1.794	3.08	0.027	0.035	1.90	0.17	-0.49	8.33	4.5
1159	0.004	0.40	0.004	0.20	0.000	0.005	0.27	0.26	0.21	0.29	0.4
1210	0.230	13.69	1.937	-0.08	0.068	0.092	4.00	-3.95	0.84	-1.52	...
1210	0.006	0.50	0.006	0.26	0.006	0.006	0.37	0.37	0.26	0.40	...
1299	0.181	23.54	2.079	2.32	0.027	0.027	7.55	-7.40	5.68	5.35	6.1
1299	0.006	0.49	0.006	0.26	0.000	0.000	0.37	0.38	0.23	0.41	0.7
1385	0.073	10.70	1.459	4.96	0.027	0.027	1.40	0.02	0.01	-3.07	16.4
1385	0.004	0.40	0.004	0.21	0.000	0.000	0.32	0.33	0.26	0.46	0.5
1458	0.238	21.21	2.081	0.30	0.119	0.144	5.78	-4.04	3.77	7.62	...
1458	0.005	0.41	0.005	0.21	0.005	0.005	0.28	0.32	0.23	0.30	...
1507	0.163	17.73	1.625	0.98	0.064	0.096	4.07	-0.35	0.15	3.93	...
1507	0.006	0.51	0.005	0.31	0.007	0.007	0.41	0.43	0.33	0.35	...
1567	0.344	24.36	2.209	-0.91	0.067	0.097	3.79	-3.05	2.77	8.11	...
1567	0.006	0.38	0.005	0.22	0.005	0.005	0.28	0.30	0.22	0.26	...
1590	0.214	17.34	2.234	-0.65	0.145	0.177	5.50	-4.11	-0.55	7.76	...
1590	0.007	0.50	0.006	0.25	0.006	0.006	0.30	0.35	0.25	0.30	...
1614	0.308	22.95	1.951	-0.72	0.084	0.112	3.23	-3.00	3.64	4.55	...
1614	0.005	0.40	0.005	0.20	0.005	0.005	0.27	0.30	0.19	0.31	...
1682	0.186	19.97	1.886	1.35	0.027	0.027	3.47	-3.20	2.95	5.16	...
1682	0.003	0.28	0.003	0.12	0.000	0.000	0.19	0.19	0.13	0.21	...
1811	0.116	19.05	2.075	-1.84	0.085	0.100	6.89	-8.30	1.96	6.88	...
1811	0.009	0.83	0.009	0.37	0.009	0.009	0.50	0.52	0.37	0.47	...
1920	0.044	33.16	2.516	-3.46	0.027	0.056	5.57	-4.45	5.39	-13.58	38.
1920	0.016	1.41	0.019	0.62	0.000	0.015	0.82	0.89	0.54	1.05	10.
1935	0.264	19.47	2.393	-2.04	0.109	0.141	2.67	-2.95	2.35	4.04	...
1935	0.006	0.37	0.005	0.21	0.005	0.005	0.27	0.28	0.24	0.27	...

NOTE. — The second line for each galaxy lists the uncertainties.

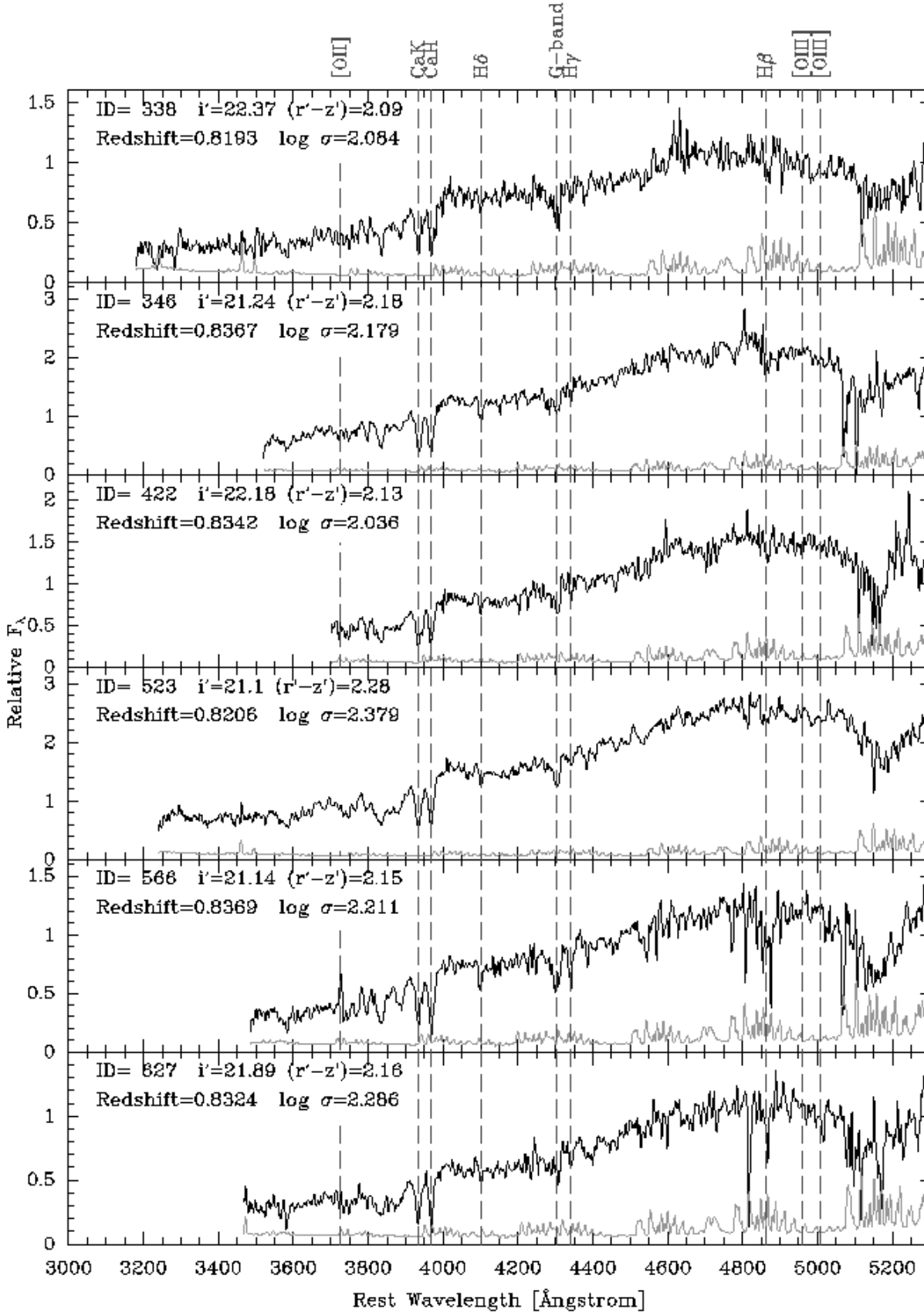


FIG. A17.— Spectra of the galaxies that are considered members of the cluster. Black lines – the galaxy spectra; green (grey) lines – the random noise multiplied with four. At the strong skylines, the random noise underestimates the real noise due to systematic errors in the sky subtraction. Some of the absorption lines are marked. The location of the emission lines [O II], [O III] λ 4959, and [O III] λ 5007 are also marked, though these lines are only present in some of the galaxies. The spectra shown in this figure have been processed as described in the text, including resampling to just better than critical sampling.

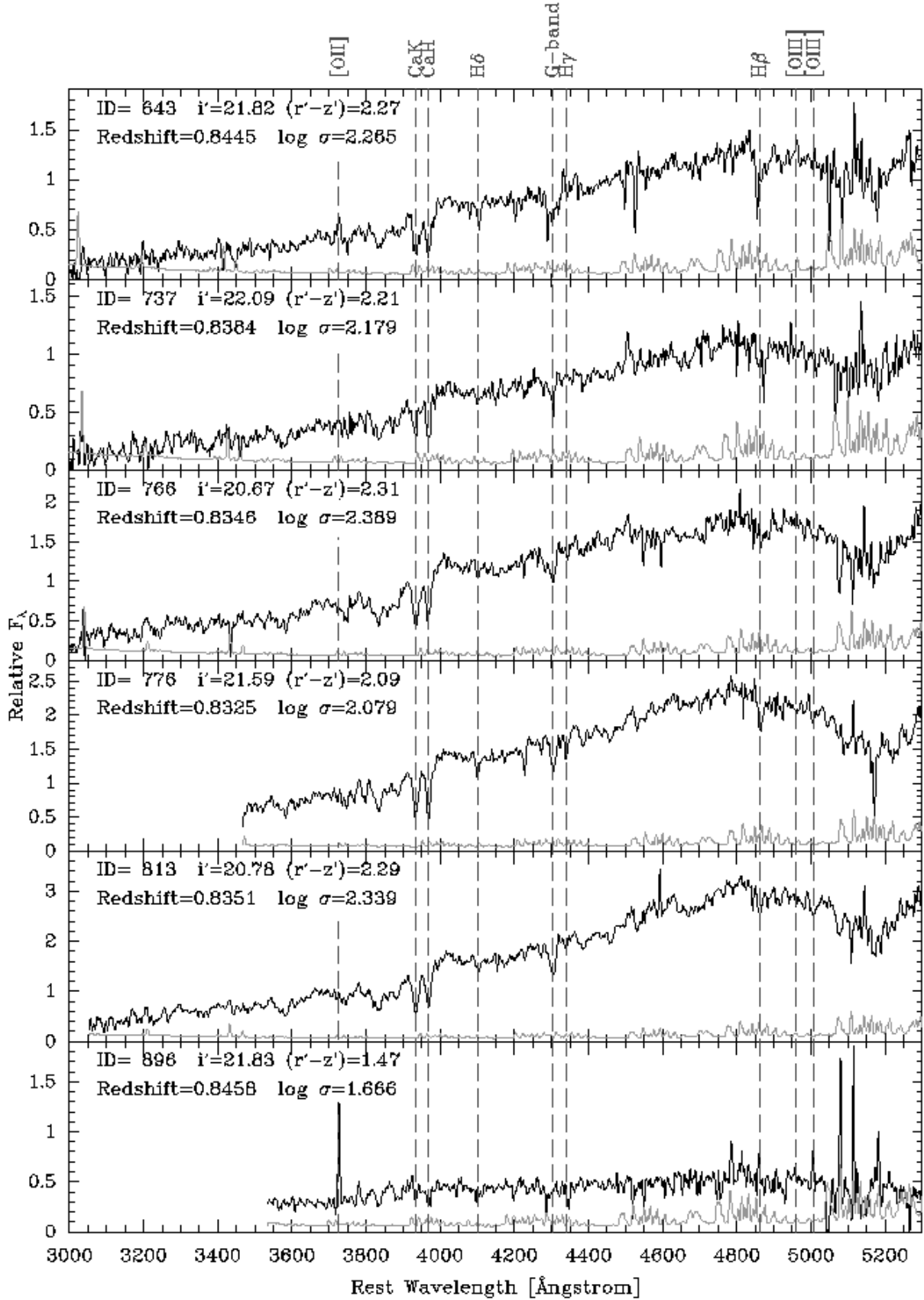


Fig. A17 - Continued.

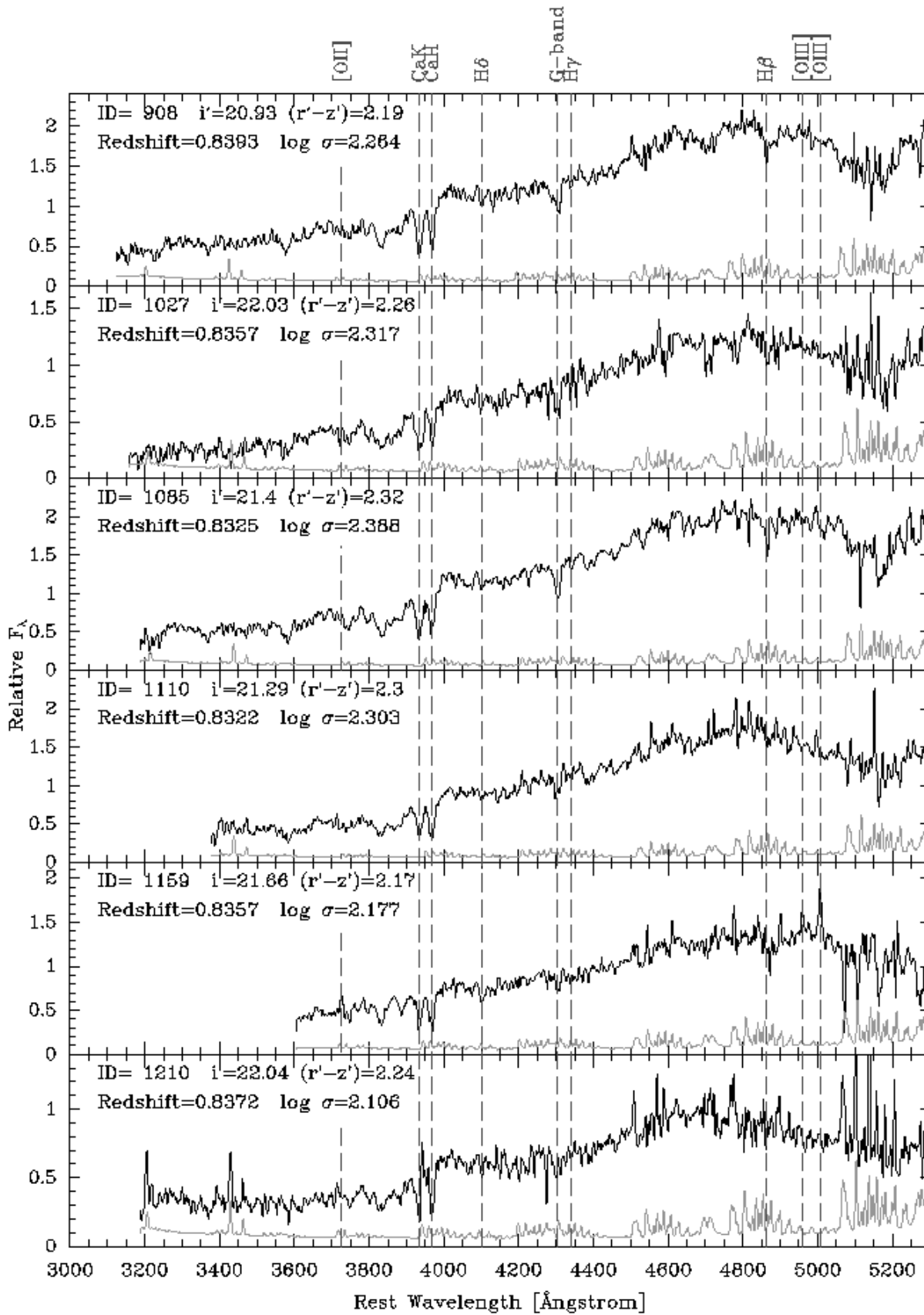


Fig. A17 - Continued.

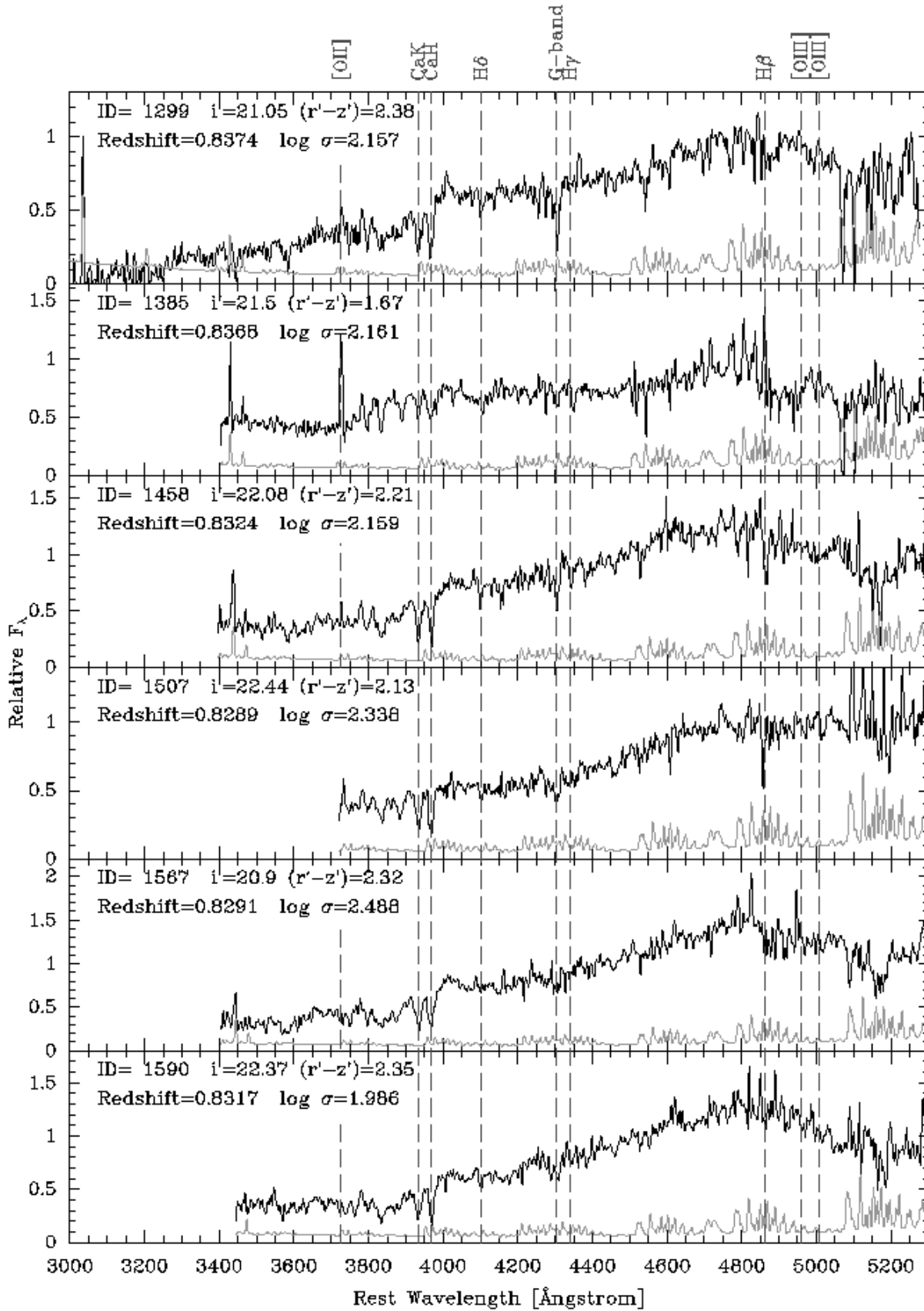


Fig. A17 - Continued.

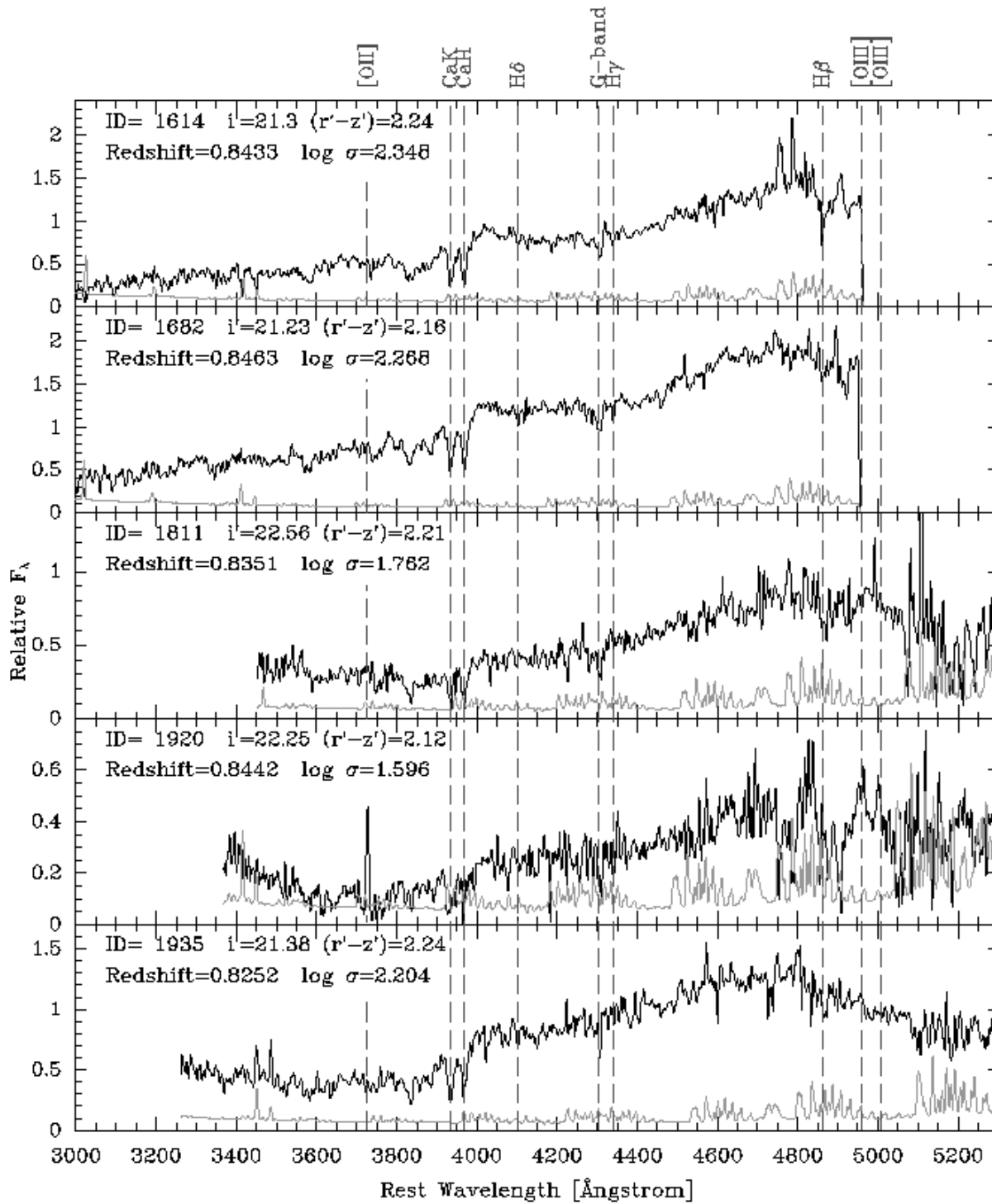


Fig. A17 - Continued.

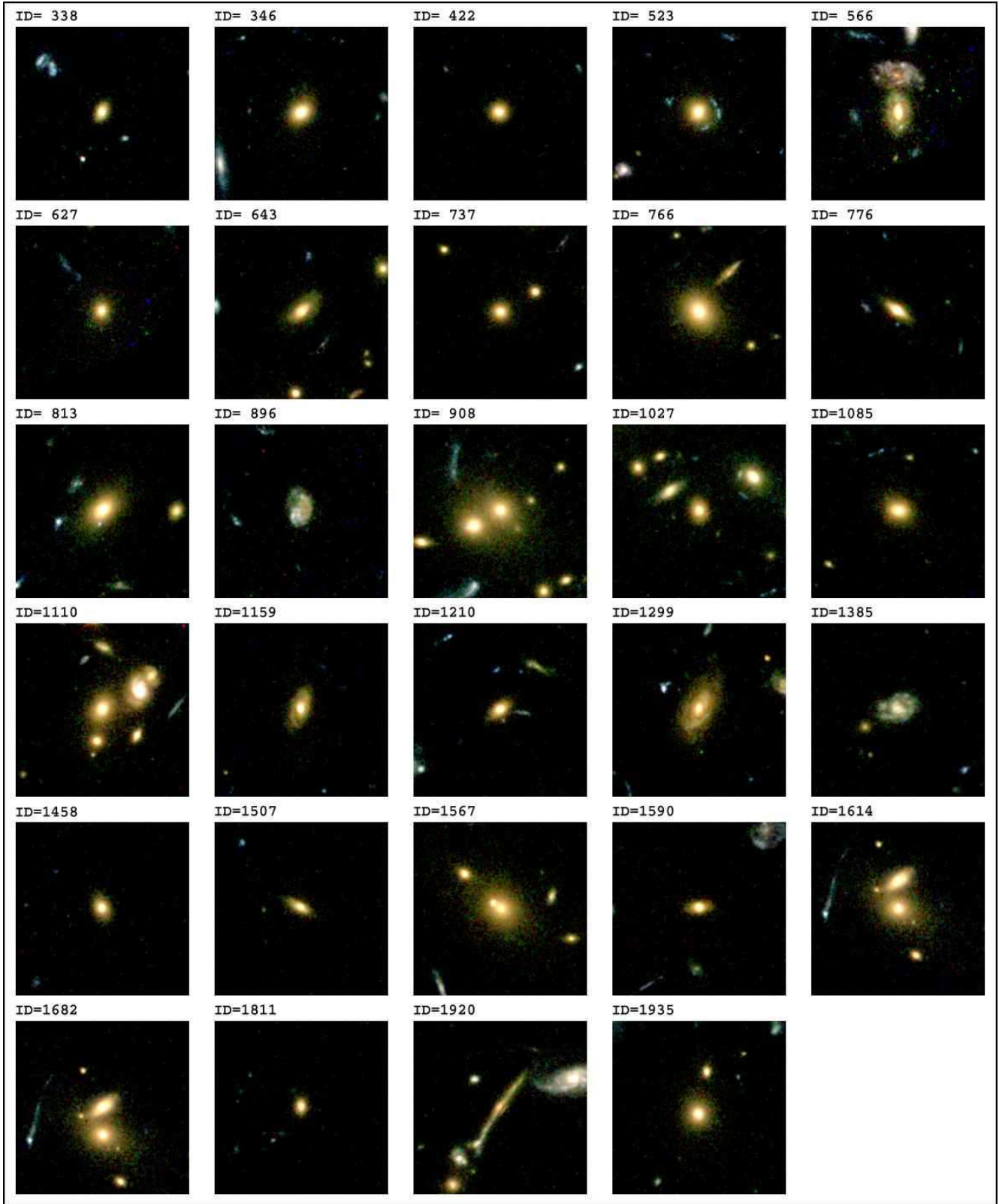


FIG. A18.— Color images of the cluster members made from archive HST imaging obtained with the ACS (program ID 9290, PI Ford). The HST/ACS images are reproduced as follows: F625W (r') is blue, F775W (i') is green, and F850LP (z') is red. Each image covers $10 \text{ arcsec} \times 10 \text{ arcsec}$. At the distance of RXJ0152.7–1357 this corresponds to $75 \text{ kpc} \times 75 \text{ kpc}$ for our adopted cosmology. North is up, East to the left. In each panel, the galaxy with the ID listed above the image is located in the center of that image.